UNIVERSITY OF CALIFORNIA SAN DIEGO

Ray Triplications and Caustics: The Imprint of Ocean Fine Structure on Underwater Sound

A dissertation submitted in partial satisfaction of the
requirements for the degree Doctor of Philosophy

in

Oceanography

by

Jacob Paul DeFilippis

Committee in charge:

Andrew J. Lucas, Chair
Bruce Cornuelle, Co-Chair
William Coles
John Colosi
Florian Meyer
William Young

2024

The Dissertation of Jacob Paul DeFilippis is approved, and it is acceptable in quality and form for publication on microfilm and electronically.

University of California San Diego

2024

DEDICATION

To Frances, may you have an inquisitive mind so that I may see the world anew.

EPIGRAPH

Once in a while, you get shown the light in the
strangest of places when you look at it right

Jerry Garcia

But the desert is a vast world, an oceanic world, as deep in its way and complex and various as the sea. Language makes a mighty loose net with which to go fishing for simple facts, when facts are infinite.

Edward Abbey

TABLE OF CONTENTS

LIST OF FIGURES

LIST OF TABLES

PREFACE

This dissertation is really split into two parts. The first part, Chapter 3, was done when I started my doctorate and before the TFO field experiments of 2020 and 2021. The models in Chapter 3 were the start of describing how the acoustic phase could vary past the internal wave cut-off frequency. While this does happen, the observations from the field experiment yielded more interesting results about the actual wave propagation, discussed in Chapters 1 & 2. I returned to working on the third Chapter 3 near the end of my doctorate which is why I would describe the path of my writing as a Mobius strip, seeing as I finished where I began and re-visited the beginning somewhere in the middle. I hope this work can be useful to those exploring the smaller scales of the ocean.

ACKNOWLEDGEMENTS

I would like to acknowledge Professor Drew Lucas for funding my doctoral research, and leading the science team on the field expedition, the results of which are paramount to this dissertation.

I would like to acknowledge Dr. Bruce Cornuelle for his support as my co-chair. He has helped with questions big and small and has always made the time to improve my understanding of oceanography, science, and acoustics.

Lastly, I would like to thank my wife Hayley. More than half the battle of completing this dissertation was fought in the emotional arena. Thank you for being my champion and encouraging me to keep going.

Chapter 1, in full, is a reprint of the material as it appears in Journal Acoustical Society America 2023. Author list: DeFilippis, Jacob; Cornuelle, Bruce; Lucas, Drew; Hodgkiss William; Lenain, Luc; Kuperman, William; Alford, Matthew. The dissertation author was the primary investigator and author of this paper.

Chapter 2, in part, has been submitted for publication of the material as it may appear in Journal Acoustical Society America Express Letters, 2024. Author list: DeFilippis, Jacob; Cornuelle, Bruce; Lucas, Drew; Hodgkiss William; Kuperman, William. The dissertation author was the primary investigator and author of this paper.

Chapter 3, in part is currently being prepared for submission for publication of the material. Author list DeFilippis, Jacob; Cornuelle, Bruce; Lucas, Drew; Colosi, John. The dissertation author was the primary investigator and author of this material.

VITA

2015	Bachelor of Science, University of California Santa Cruz
2015–2018	Stanford Linear Accelerator Center
2018–2020	Research Assistant, University of California San Diego
2020	Master of Science, University of California San Diego
2024	Doctor of Philosophy, University of California San Diego

ABSTRACT OF THE DISSERTATION

Ray Triplications and Caustics: The Imprint of Ocean Fine Structure on Underwater Sound

by

Jacob Paul DeFilippis

Doctor of Philosophy in Oceanography

University of California San Diego, 2024

Andrew J. Lucas, Chair
Bruce Cornuelle, Co-Chair

The work included in this dissertation addresses the complexities of underwater sound propagation through fine-scale, 1-10 m, sound speed structures in the upper ocean. These small spatial variations in the ocean's sound speed strongly affect sound waves at mid-frequencies (1-10 kHz) because the wavelengths of those sound waves (1.5-0.15) m approach the scale of these sound speed structures. Chapters 1 & 2 cover observations from a field experiment off the coast of San Diego that are used to analyze sound propagation through the measured sound speed profiles that contained fine structures. Chapter 3 covers oceanographic observations from the same experiment and a model of sound speed fluctuations driven by internal wave motion

to analyze how fine-scale structures alter the power spectrum of oceanographic sound speed fluctuations. A synthesis of oceanographic and acoustic observations with models suggests that fine-scale structures create additional acoustic propagation paths, caustics, and change the temporal spectrum of sound speed variability. The culmination of these effects explains why acoustic receptions at mid-frequencies propagating in the upper ocean are generally more variable than at lower frequencies in deeper parts of the ocean.

Introduction

Sound at frequencies between $1 - 100$ Hz travels exceedingly well in the open ocean. The sound channel, first discovered by Ewing and Worzel [17], focuses the sound energy around the sound channel axis, generally at a depth of about 1000 meters in mid-latitudes. The large vertical scale structure of temperature and pressure in the ocean forms the sound channel. The sound speed of seawater in the upper ocean is dominated by temperature that is warm at the surface and colder below. The resulting sound speed gradient refracts the sound away from the surface. The sound speed of seawater below the sound channel axis is dominated by pressure which increases from the channel axis to the bottom. This gradient in pressure causes the sound speed of seawater to increase from the channel axis to the bottom, which refracts sound waves away from the bottom. Thus sound waves are trapped in the middle. The large-scale structure of the sound channel persists over basin-scale ranges, so sound emitted near the sound channel axis can travel for distances that span entire ocean basins.

Even though sound waves can travel thousands of kilometers, the phase and amplitude of those sound waves are extremely variable. The scintillation index for received sound energy in the ocean can be as large as two, which means the variance of sound intensity is twice as large as its average squared. These acoustic fluctuations are well studied[43, 15, 41, 49, 10, 13] and are mainly due to mesoscale eddies and internal waves. Mesoscale eddies create perturbations to the mean structure of the sound channel and are analogous to weather in the atmosphere. Not only have these features been studied, but researchers have used inverse methods to map out mesoscale features in the ocean with sound waves[33].

The ocean contains many scales of variability, and so not only does the ocean have a large

scale that forms the sound channel and a mesoscale that changes the sound channel over 100 km ranges, but it also has fine scales, which is the focus of this dissertation. Fine-scale structure generally refers to changes in ocean temperature and salinity over scales of 1-100 m [47]. These scales can produce large temperature and salinity gradients. For example, researchers noticed that measurements of vertical temperature gradients over a meter are often ten times the magnitude of the average gradient in the upper ocean [35]. The horizontal gradient of temperature and salinity can also change at fine scales due to spice anomalies and small ocean fronts.

For low-frequency sound, the fine scales of the ocean are not as important because the wavelength of those sound waves is much greater than the scale of the fine structure. For example, a sound wave with a 10 Hz frequency has a 150 m wavelength. However, sound waves at mid-frequencies (1-10 kHz) have wavelengths smaller than or similar to the scales of the fine structure. The similarity in scale between the wavelength and the ocean structure determines the amount of interaction between the wave propagation and sound speed. The acoustic phase and amplitude variability as a function of frequency was observed at mid-frequencies by Ewart in the Cobb Seamount Experiment [15]. Although this dependence has been shown statistically in the aggregate data, this dissertation investigates the interaction between fine structure and sound waves from a deterministic viewpoint, analyzing singular acoustic transmissions in an ocean environment that is densely sampled so that the propagation can be simulated and compared to observations.

The effect fine-scale structure has on mid-frequency sound propagation is covered in Chapters 1 & 2. Chapter 1 discusses the phenomena of ray triplication and acoustic caustics generated from fine structure. This chapter looks at three different at-sea acoustic transmissions and compares them to acoustic propagation models using measured sound speed profiles. Chapter 2 discusses the change in phase of two triplicated ray arrivals under the action of a time-evolving sound speed field. The phase difference between two observed acoustic arrivals is used to amplify the perturbations from the sound speed and source depth.

Chapter 3 focuses solely on how fine structure changes the temporal statistics of ocean

sound speed fluctuations. Changes in sound speed driven by oscillating isopycnal surfaces – internal waves – are a non-linear process that depends on the vertical derivative of sound speed. The interaction between fine-scale structure and internal waves is analyzed in this chapter with both at-sea oceanographic measurements as well as a stochastic model of non-linearly advected sound speed from internal waves.

Chapter 1

Chapter 1: Observations and simulations of caustic formation due to oceanographic fine structure

1.1 Introduction

Both deep and shallow water ocean acoustic experiments have shown that acoustic travel-time variability can be related deterministically to sound-speed perturbations from oceanographic processes such as internal tides and mesoscale eddies [2, 24, 26], and that phase and amplitude fluctuations of ocean acoustic receptions can be related statistically to the spectrum of internal waves [2, 15, 41]. Although these oceanographic processes are responsible for most of the acoustic travel time, phase, and amplitude fluctuations, at time scales ranging from hours to days, small-scale (1-10 m) variations in the vertical sound-speed gradient, generally referred to as fine structure[35, 47], can alter the acoustic phase and amplitude fluctuations from those same processes[10, 14]. Acoustic propagation effects such as caustic formation and micro-multipathing have been attributed to fine structure[15, 11], but a deterministic comparison between observed and modeled acoustic propagation through oceanographic fine structure has not been done. The observations and modeling in this paper show that sections of the sound-speed profile with strong second derivatives due to the small-scale structure in the ocean can triplicate ray paths. Consequently, those triplicated rays result in multiple acoustic arrivals with a small time of

arrival separation at the receiver.

Previous mid-frequency ocean acoustic experiments[16, 41, 48], transmitting at ranges less than 40 km with broadband pulses, looked at phase and amplitude fluctuations in relation to predicted sound-speed fluctuations from internal waves. Acoustic fluctuations are severe for mid-frequency (1-10 kHz) acoustic propagation through the upper ocean because the acoustic wavelength approaches the scale of the fine structure in the ocean [15]. The simulated acoustic phase and amplitude statistics were less like the observed phase and amplitude statistics when the fine structure was removed from the sound-speed profile [14]. This disagreement worsened as frequency increased. This comparison suggested that fine-structure measurements would be crucial to making a quantitative comparison between acoustic fluctuations and internal waves, particularly for mid-frequency acoustic propagation.

In these experiments, pulse arrivals that were identified with individual eigenrays computed from a time-averaged sound-speed profile would often appear to be comprised of multiple overlapping pulse arrivals. The time-averaging of the sound-speed profile tends to remove small-scale sound-speed structures because of their time-varying depths due to internal waves. Hence, fine vertical scales of the sound-speed profile were theorized to allow for multiple pulse arrivals that came from additional ray paths that were adjacent in launch angle to the unperturbed path calculated from the time-averaged profile [15]. These nearby ray paths are frequently called micro-multipaths or microrays [3], which originate from caustic formation/ray triplication discussed further in Section 1.4.

Parts of the recorded acoustic arrivals from the Slice89 experiment [10], which transmitted 250 Hz center frequency broadband pulses at 1000 km in range, were also associated with ray triplication from oceanographic fine structure [11]. The relative curvature of the sound-speed profile, $U(z) = c(z)\partial_{zz}c(z)/(\partial_z c(z))^2$, was suggested as a dimensionless parameter for inferring caustic formation by Duda and Bowlin [11]. This parameter is useful for evaluating when curvature in the profile is likely to form caustics and consequently triplications in the timefront. $U(z)$ can be singular and highly variable, so the moments of its distribution are often more

relevant. Normally $U(z)$ is reported as the logarithm of its absolute value, $U_{10} = log_{10}(|U(z)|)$.

In order to study the influence of ocean fine structure on mid-frequency acoustic propagation at sub-hourly time scales, we conducted a joint ocean acoustics/physical oceanography experiment offshore of Southern California. The experiment, described in Section 1.2, used shipboard and semi-autonomous sampling to provide measurements of the environment near the sound transmission paths (less than 2 km). Pulses of sound at 1-10 kHz were transmitted along paths of 1 - 5 km in length. Both oceanographic and acoustic observations from the experiment are described in Section 1.3.

Modeling the effects of vertical fine structure on the acoustic propagation, described in Section 1.4, with a deterministic approach is possible because of the proximity of the oceanographic measurements to the short-range acoustic propagation paths that have single turning points. A deterministic approach was previously used by other researchers to model travel time fluctuations caused by perturbations to the sound-speed field from a large non-linear internal wave [26] and model the attribution of caustics in shallow-water acoustic communication experiments with rays reflecting from ocean surface gravity waves [7], which is a motivation for this study. Caustics and triplicated ray paths from surface waves were found to complicate signal processing to varying degrees based on the shape of the sea surface[40]. The comparison between observations and model, described in Section 1.5, identifies features in the sound-speed profile that cause interfering arrivals in the acoustic observations.

1.2 Methods

1.2.1 Experimental Setup

The at-sea experiment took place from 5-25 May 2021 on the R/V Roger Revelle in deep water 450 km from the coast of Southern California. The experiment site is outlined by the box shown in Fig. 1.1. This site was chosen to sample a region without bathymetric features that would have affected the acoustic propagation or oceanography such as acoustic bottom reflection

or local internal tide generation.

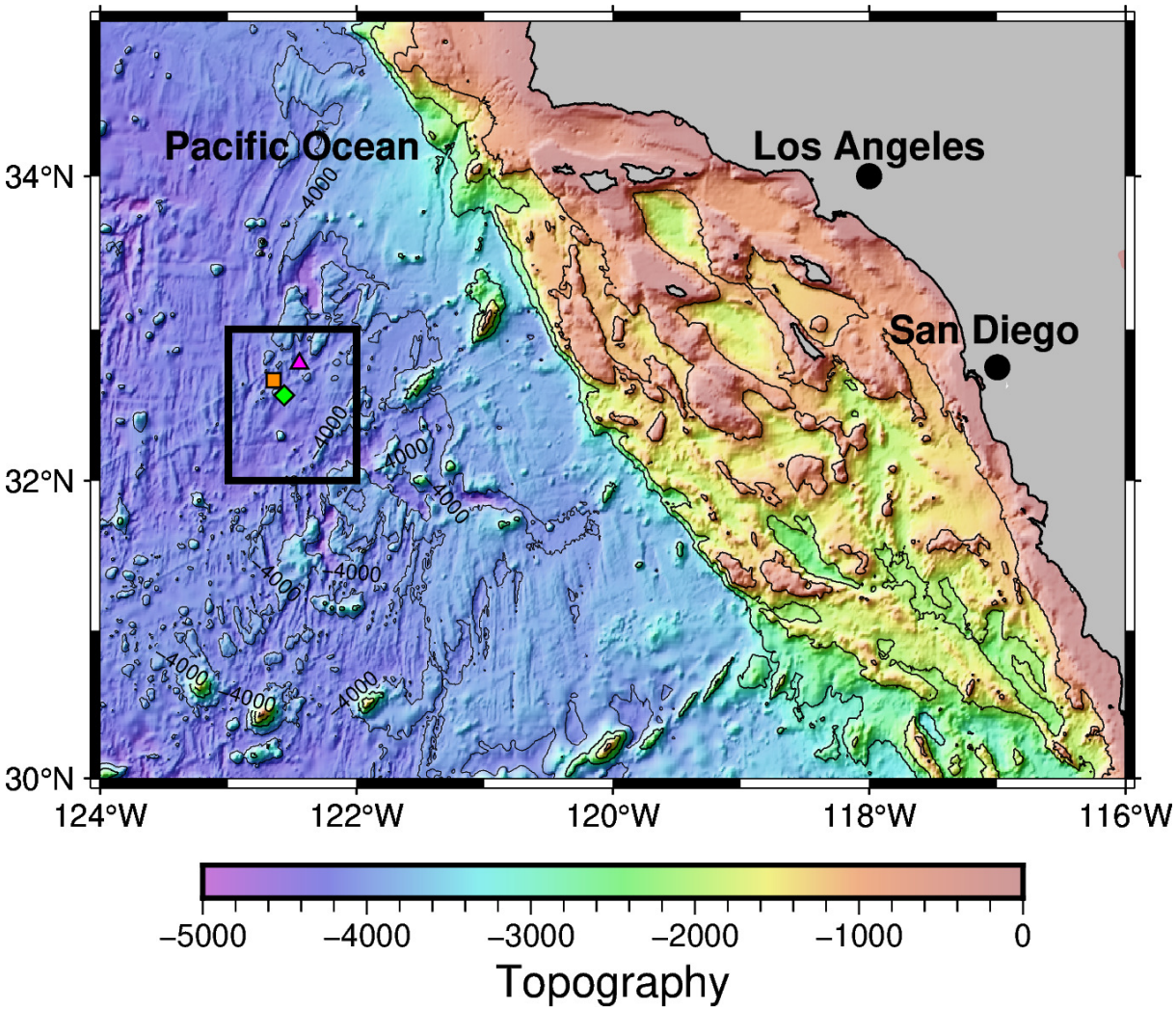

Figure 1.1. A bathymetric map showing the location of the experiment inside the box. The site is approximately 450 km from San Diego, off of the continental shelf, with a bottom depth of roughly 4000 m. The locations of the three acoustic transmissions discussed in this paper are marked with a green diamond, purple triangle, and orange square.

Acoustic transmissions were made at roughly fixed ranges from 1 to 5 km from a single shipboard acoustic source to a single drifting vertical line array with 64 elements. The array had an aperture of 7.875 m with uniform 0.125 m hydrophone spacing. The nominal depth of the acoustic source was 200 m and the nominal receiver array center depth was 132 m, with most of the received sound traveling through the upper 200 m of the ocean. Fig. 1.2 shows a schematic of the acoustic experiment setup with an example of the acoustic ray paths calculated with a ray

trace model using sound-speed data from the experiment.

Both continuous wave and maximum length sequences (MLS) forming pseudo-pulses were transmitted at a 156 dB re $1\mu Pa^2$ source level. These transmissions were in the acoustic mid-frequency band (1-10 kHz) so that the acoustic propagation would interact more with the fine-scale features of the ocean environment. Maximum length sequences were used to modulate the phase of the 4 kHz carrier frequency with a 4 kHz bandwidth. The repetition rate of the sequence is set by the MLS length of 63.5 ms with 2 cycles per digit. The hydrophones on the receiver array have high-pass poles at 100 Hz and 500 Hz, attenuating low-frequency ambient noise. The receiver array data acquisition system samples the hydrophone time series at 25 kHz. A set of maximum length sequences was matched-filtered to calculate the travel time, phase, Doppler shift, and intensity of the arrivals. After conditioning the signal and applying the matched filter, the SNR of the pulse is approximately 15 dB. The peak arrival time uncertainty of roughly 0.3 ms is calculated using the bandwidth and SNR of the pulses[34]. The time precision and vertical resolution of these measurements allow us to probe the fine scales of acoustic fluctuations. Further information on the MLS performance can be found in Gemba et al.[22].

The background characteristics of the sound speed in the operating area were supplied by four drifting Wire Walkers and the shipboard FastCTD. Wire Walkers[36, 50, 31] are drifting oceanographic sampling platforms carrying a CTD that profiled the between 0-500 m depth of temperature, salinity, and pressure roughly every 30 minutes with 0.25 m vertical resolution. Wire Walkers were deployed in an array encompassing the acoustic instruments. The distance between drifting Wire Walkers was initially set between 5-10 km. The FastCTD, a rapid shipboard profiling platform, measured temperature, salinity, and pressure when the acoustic source was not transmitting. This platform can profile 0-300 m depth at a roughly 0.1 m vertical resolution every three minutes[27]. Measurements from these instruments were used to calculate vertical correlation length scales and the statistical relationship between temperature and salinity in the region, while two thermistor chains and a Wave Glider provided direct measurements of the sound-speed profile near the transmission path.

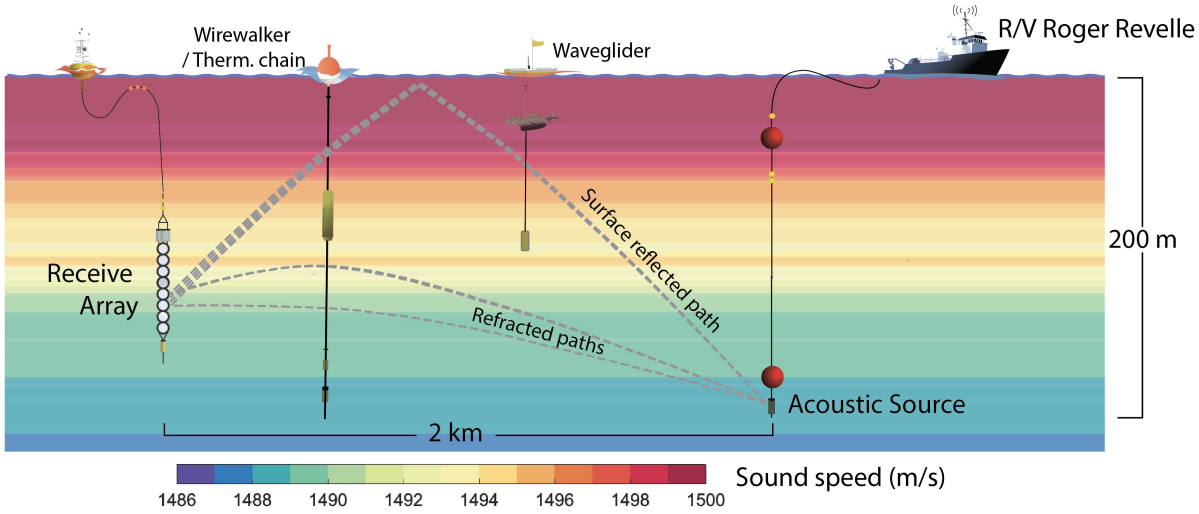

Figure 1.2. A typical instrumental setup for acoustic transmissions during the experiment. The acoustic source and array center were at depths of 200 m and 132 m, respectively, separated by approximately 2 km in range. A drifting thermistor chain and Wave Glider platform measured sound speed nearby the turning point of acoustic ray paths. The gray dashed lines mark ray paths that intersect both source and receiver. The ray paths were calculated using a sound-speed profile shown with the background layers of color. The sound speed was measured by a drifting thermistor chain on 7 May 20:20.

The two drifting thermistor chains, TC5 and TC7, were deployed 1-2 km away from the drifting receiver array. Both thermistor chains spanned 0-200 m in depth. TC5 had thermistors placed every 2 m in depth with pressure sensors every 25 m between 0-200 m. TC5 thermistors had a 0.1 ms thermal response time and a 2 Hz sampling rate. TC7 had a hybrid configuration with both thermistors and a Wire Walker deployed on the chain. TC7 had thermistors placed every 3 m in depth with pressure sensors every 25 m between 0-50 m and 100-200 m depth. TC7 thermistors had a 1 s thermal response time and a one-minute sampling rate. The TC7 Wire Walker profiled between 50-100 m depth along the chain. At these depths, the Wire-Walker CTD profiled salinity, temperature, and pressure with 0.25 m vertical resolution every 15-20 minutes.

The in-situ temperature profiles, $T(P)$, from the thermistor chain, were converted into sound-speed estimates $c(P)$ by constructing an empirical relationship between salinity and temperature $S(T)$. Once $S(T)$ was calculated, the sound-speed estimate was calculated via the equation of state $c(P) = c_{eos}(S(T(P)), T(P), P)$ [32]. The error due to the absence of in-situ

salinity measurements, discussed later in the section, is on average less than 0.1 m/s. The pressure coordinate, P was converted into depth from the mean sea surface rendering a sound-speed profile $c(z)$.

The Wave Glider, a piloted semi-autonomous vehicle [25, 29], profiled temperature, salinity, and pressure with a CTD every 10 minutes between 50-130 m depth with roughly 0.15 m vertical resolution. This depth range spans the turning depths of acoustic rays that were received by the array. The Wave Glider was positioned precisely between the acoustic source and receiver array for some of the acoustic transmissions. The drifting thermistor chains and the Wave Glider's profiling CTD were used to estimate the sound-speed field near the midpoint of the acoustic transmissions.

Three acoustic transmissions with simultaneous nearby sound-speed profiles were chosen to demonstrate the relationship between fine structure and interfering acoustic multi-paths. These acoustic transmission periods are highlighted because they were at relatively short ranges (less than 3 km) and the thermistor chains or Wave Glider were sampling close to the turning points of the ray paths. These transmissions took place on 7 May from 18:52 to 21:35, 10 May from 20:00 to 22:15, and 17 May from 18:00 to 19:45. All times are reported in UTC. Labels T1, T2, and T3 are given to minute-long blocks of continuous transmissions for 7 May 20:22, 17 May 19:10, and 10 May 20:30, respectively. These labels are ordered by transmission range. Fig. 1.3 shows the GPS tracks of both the acoustic and oceanographic instruments during the transmission period with a line and the GPS position at T1, T2, and T3 with a circle marker.

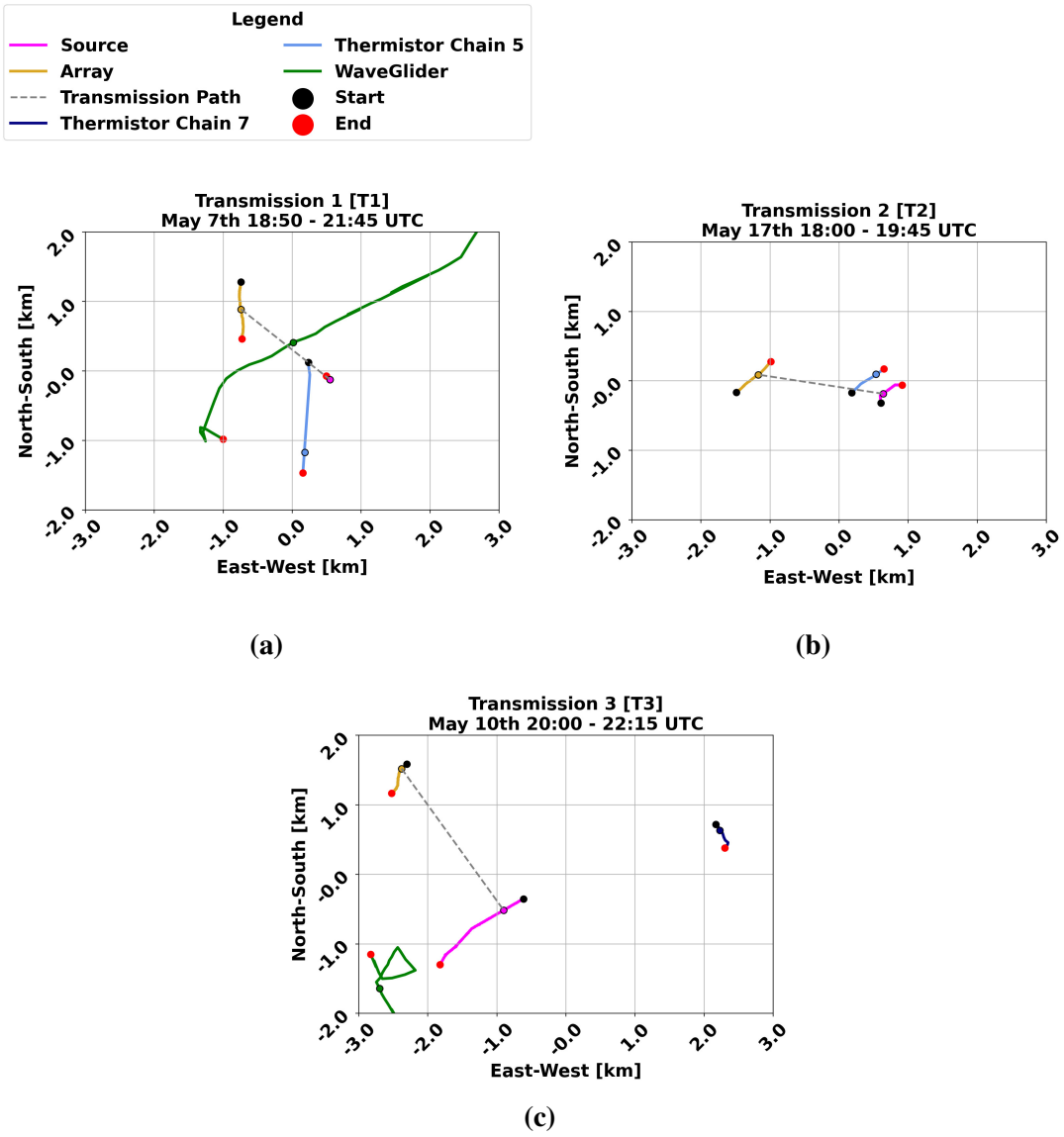

Figure 1.3. The GPS positions of the drifting receiver array (gold line), the acoustic source on the R/V Roger Revelle (magenta line), drifting thermistor chains (dark and light blue lines), and the Wave Glider (green line). Each line has a red and black dot that indicates the start and end position of each track. Panels (a),(b),(c) show the GPS tracks on 7 May from 18:52 to 21:35, 17 May from 18:00 to 19:45, and 10 May from 20:00 to 22:15, respectively. A circle marker with the same color as the track line is drawn for minutes 7 May 20:22, 17 May 19:10, and 10 May 20:30 for (a),(b),(c) to mark transmissions T1, T2, and T3 respectively. A transmission line is also drawn from source to receiver at those transmission times (grey dashed line).

1.3 Data

1.3.1 Sound-Speed Observations

Sound-speed measurements from the Wave Glider, TC5, and TC7, shown in Figs. 1.4a,b,c, correspond to the minute-long transmission intervals T1, T2, and T3 in Figs. 1.3a,b,c, respectively. Sound-speed profiles are made by interpolating through the sound-speed measurements from those instruments. In Sections 1.4 and 1.5, these sound-speed profiles are input into acoustic propagation models to connect the observed acoustic arrivals to the observed oceanographic structure.

The thermistors were affected by the surface wave action on the thermistor chain surface buoy. The thermistors were displaced vertically at depth, although, the displacement was vertically coherent, implying that the chain acted stiffly. This displacement was typically 1-2 m over 10 seconds. The combination of this displacement and the 2 Hz sampling rate for thermistors on TC5 was utilized to form a synthetic aperture by grouping minute-long intervals of thermistor data (light blue dots) to produce a temperature profile every minute. This minute-long interval of temperature samples filled in the vertical gaps between thermistors along the chain and provided a nearly continuous profile with an 0.02 m average vertical resolution. The synthetic aperture could not be used for thermistors on TC7 (dark blue dots), which had a one-minute sampling.

During transmissions T1 and T3, the Wave Glider measurements (green dots) were closer to the acoustic transmission path than measurements from TC5 and TC7, which were roughly 1-4 km away from the transmission path. Outside the Wave Glider's profiling range, 50-130 m, the thermistor chain measurements were used to fill in the sound-speed profile from 130-200 m and from the 0-50 m depth. We believe using two horizontally-separated estimates of sound speed for the propagation modeling is justified because the sound speed at the depths filled in by the thermistor chain does not vary as strongly (see Fig. 1.4), and the acoustic propagation was not as sensitive to changes in the sound speed at those depths compared to depths of 50-130 m.

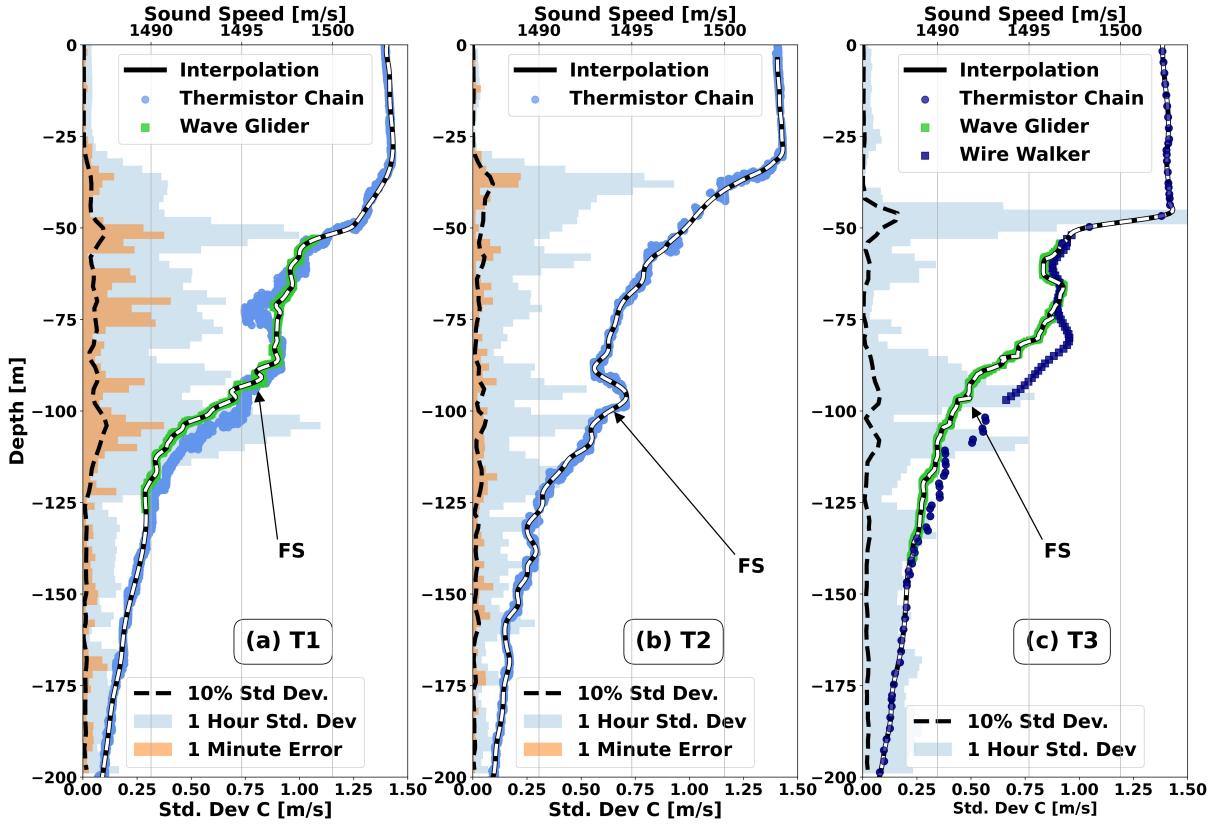

Figure 1.4. Sound-speed profiles during transmission T1, T2, and T3 are made from sound-speed estimates collected by thermistors on TC5 (light blue dots), thermistors on TC7 (dark blue dots), the profiling Wire Walker CTD on TC7 (dark blue squares), and the profiling Wave Glider CTD (green squares). A cubic spline (black and white dashed line) was fit to a minute-long collection of the sound-speed estimates. The labels 'FS' point out a few examples of fine structure in the sound-speed profile. The top and bottom horizontal axis shows the scales for sound speed and sound-speed deviation. The standard deviation of sound speed (blue bars) over an hour and the root-mean-square misfit (orange bars) of the spline over a minute are binned into one-meter depths along the left vertical axis. The black dashed line on the left side of each figure is 10 percent of the hour-long standard deviation. Fig. 1.4c does not have an interpolation error because this particular thermistor chain had a one-minute sampling rate.

Sound-speed measurements from the thermistor chain and Wave Glider were least-squares fit to a cubic spline to create a twice-differentiable sound-speed profile, shown in Fig. 1.4 as the black and white dashed line. The spline is comprised of piece-wise third-order polynomials [9]. The coefficients of each piece-wise polynomial are defined over a finite interval. The boundary of each interval is called a knot. At each knot, the value, first, and second derivative of the neighboring piece-wise polynomials must be equal, which enforces the continuity of the

spline. The cubic splines had an approximately 2 m knot spacing which enforced polynomial smoothness in the sound speed over 2 m scales. This scale was chosen so that the splines would not overfit the data but at the same time model the meter-scale vertical sound-speed structures.

We assume internal waves are the dominant process driving the temporal sound-speed variability at sub-hourly time scales represented by the hour-long standard deviation (blue bars) to the mean sound speed as measured by TC5 and TC7 in Figs. 1.4a,b,c. The sound-speed fluctuation, $\delta c(z)$, at a depth z from the mean sound speed results from vertically-varying internal wave vertical displacement $\zeta(z)$ of the potential sound-speed profile $c(z)$. This fluctuation is described in Equation (1.1),

$$\begin{aligned} \delta c(z) = c(S(z), T_p(z), P(z)) \\ - c(S(z-\zeta(z)), T_p(z-\zeta(z)), P(z)) \quad , \end{aligned} \tag{1.1}$$

where S is salinity, P is pressure and T_p is potential temperature.

The root-mean-square (RMS) residuals from the spline fit to a minute-long set of sound-speed observations measured by TC5 are shown in Figs. 1.4a,b (orange bars). The residuals are the difference between the fitted spline curve and the sound-speed point observations. The differences are mostly due to bias from fitting to a spline curve to the measurements, which may have sharper curvature. The change in sound speed over a minute from the internal waves is expected to be small because of the drop in internal wave displacement power at the maximum buoyancy frequency N[23], which was about 4 cycles per hour in the experiment region.

The sound-speed profiles in Fig. 1.4 have depths where strong and weak sound-speed derivatives alternate, appearing as steps along the sound-speed profile. The second derivative of sound speed is strongest at the edge of each fine-structure step, where the first derivative abruptly changes from strong to weak or vice versa over a small vertical distance. Parts of the sound-speed profile with high relative curvature $U_{10}(z)$ are labeled with 'FS'. At these depths, U_{10} is equal to 5.7, 5.7, and 5.8 for T1, T2, and T3, respectively, which is greater than 95 percent of the relative curvatures (not shown) between 0-200 m depth in each profile. The depth-mean U_{10}

for sound-speed profiles during T1, T2, and T3 is 3.9, 3.9 and 4.1, respectively. According to previous studies, the mean relative curvature of these profiles is large enough to expect multiple ray triplications.

Vertical fine-scale structures were frequently observed from depths of 50-150 m during the experiment from other oceanographic instruments. A vertical auto-correlation function of sound speed was calculated between depths from 50-150 m using sound-speed profiles from four nearby Wire Walkers. The average scale of the fine structure was 7 m, which is the vertical lag necessary to reduce the vertical auto-correlation function to half its value. The auto-correlation function of the first derivative of sound speed was estimated by multiplying the Fourier transform of the auto-correlation function by a factor of k^2, the vertical wavelength, and then inverse-transforming the product. The result had a vertical decorrelation of 1.2 m. This decorrelation suggests the second-derivative-length scale can be on the order of a meter or less.

The displacement of the sound-speed profile by internal waves is shown in Fig. 1.5 with a series of minute-interpolated sound-speed profiles stacked next to each other over a period of roughly 2.5 hours centered around transmission T2. The changing position of the fine structure over time (e.g. the curvature in the sound-speed profile between 95-100 m) and the motion of potential isotherms of 9.2°, 10.8°, and 11.4° C with mean depths of 83, 118, and 130 m highlight the vertical motion of the internal waves. The vertical displacement of the fine structure near 120 m depth is estimated by the change in depth of the 10.8° isotherm (green line). The isotherm depth deviated from a mean depth of 118 m by $\pm$4 m over the 2.5-hour period with a 1.8 m standard deviation. On 17 May from 19:10 to 19:20, the 10.8° isotherm was displaced upwards by one meter. The gradients of the fine structure at the 10.8° isotherm depth are vertically displaced by one meter as well over this period. The displacement of the fine structure perturbs two acoustic receptions. These receptions are discussed further in Section 1.5.

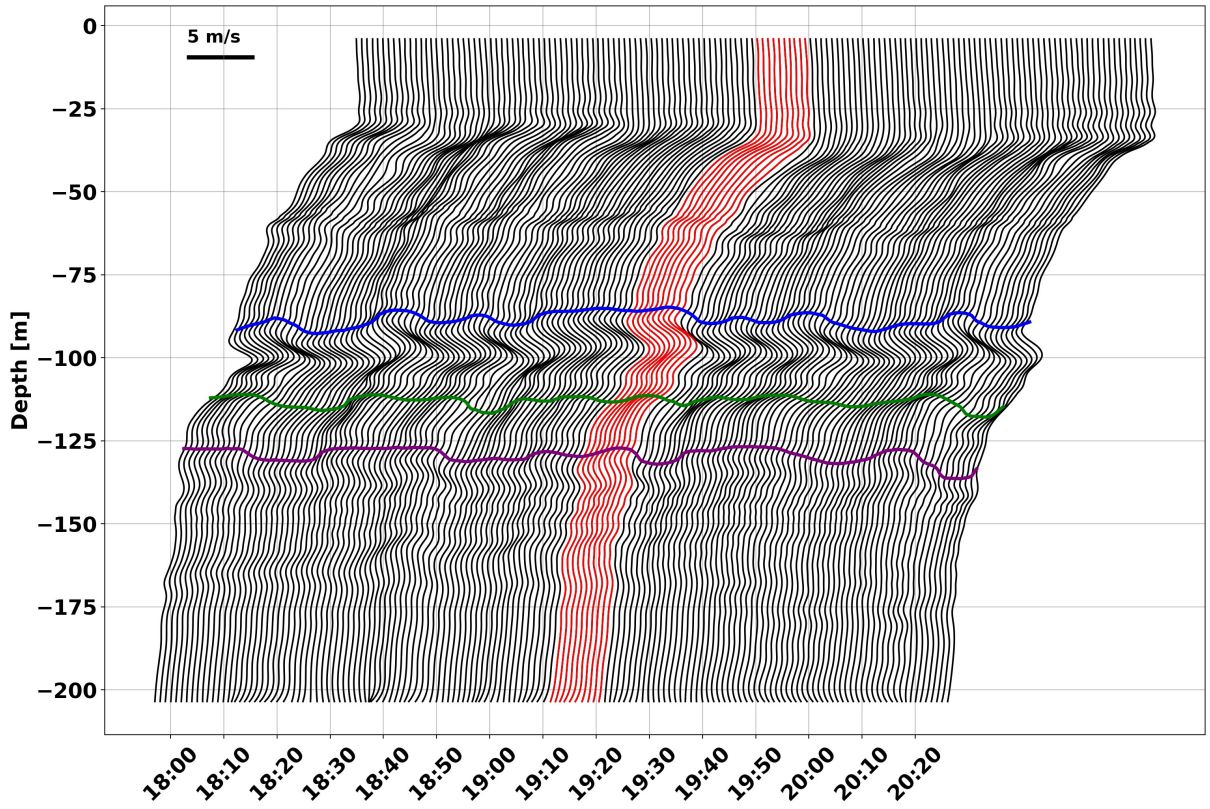

Figure 1.5. A series of interpolated sound-speed profiles using estimates from the drifting thermistor chain (TC5) plotted roughly over 2.5 hours on 17 May from 18:00 to 20:30 during the T2 transmission. The sound-speed profile at minute 19:10 is shown in Fig. 1.4b. Each profile is separated by one minute in time. Time and sound speed are plotted on the same axis, and so the 5 m/s scale bar at the top left helps show the scale of the sound-speed profiles. The time of each profile is aligned with the time axis starting at the bottom of each profile. The red profiles highlight a ten-minute range between 19:10 to 19:20. Three colored lines show constant potential temperature contours of 11.4° (blue), 10.8° (green), and 9.2° (purple) Celsius. The red sound-speed profiles highlight a 10-minute period that is related to acoustic receptions discussed further in Section 1.5.

In addition to the vertical displacement of internal waves, on-isopycnal variability of salinity and temperature creates lateral changes in the sound-speed profile. This variability, referred to as spice, corresponds with temperature variability that compensates for the salinity-related changes in density on an isopycnal. The total sound-speed anomaly can be decomposed into two components: vertical displacement of isopycnals and the spice anomaly along isopycnals [12]. The on-isopycnal variability in the California Current System, in general, is due to

larger-scale oceanographic processes related to water mass formation and mixing [46]. The interleaving of different water masses can contribute to vertical sound-speed gradients. However, the horizontal advection of these water masses is not changing the sound speed at time scales comparable to the displacement from internal waves, see Fig. 1.6a. Hence, we focus on the vertical displacement of the isopycnals from internal waves, specifically near the turning point of the transmission, as the dominant oceanographic process contributing to the acoustic fluctuations.

An 11 km transect during a four-hour period of FastCTD profiling on 18 May from 7:30-11:30 is used to quantify the relationship between temperature and salinity in the region, see Fig. 1.6b. The temperature, salinity, and pressure measurements from the FastCTD are plotted with labeled contours of density shown at 0.2 kg/m^3 intervals. The mean and standard deviation of salinity and temperature (black line with cross marks) are interpolated to form the empirical salinity-temperature relationship $S(T)$. The sound-speed anomaly along three isopycnals during the transect with mean depths of 60, 100, and 140 m shows the lateral scale of the spice anomaly, see Fig. 1.6a. The sound speed along isopycnals (green and yellow lines) near the turning depths of the ray paths in the experiment changed on the order of 1 m/s over roughly 10 km. The isopycnal near the mixed layer (red line) changed 2 m/s over roughly 1 km due to the distinct water masses on the 1024.8 isopycnal, see Fig. 1.6b.

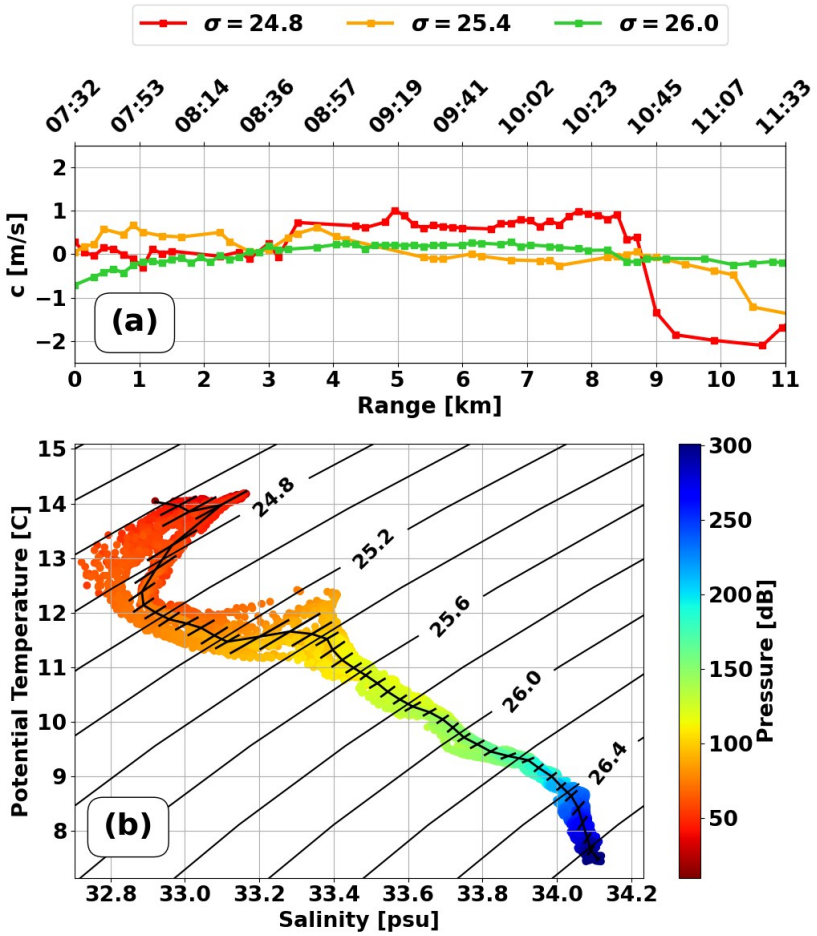

Figure 1.6. Salinity, temperature, pressure, and density measurements from 3-minute sampled FastCTD profiles down to 300 m depth during a four-hour transect on 18 May. Fig 1.6a shows the sound-speed anomaly from the mean sound speed along an isopycnal over the transect for densities of 1024.8, 1025.4, and 1026 kg/m^3 with mean depths of 60, 100, and 140 m. Fig 1.6b shows salinity and temperature measurements (colored dots) with contours of constant density (labeled black lines) plotted at $0.2 kg/m^3$ intervals. The pressure of each sample is shown in color. The mean temperature and salinity curve is calculated from 1024.6-1026.6 kg/m^3 at intervals of 0.05 kg/m^3 and is plotted in Fig 1.6b as a black line with cross bars that represent the standard deviation of temperature and salinity within each density interval.

The empirical salinity-temperature relationship shown in Fig. 1.6b is used to estimate the salinity from thermistor temperature. Relating salinity to temperature is necessary to calculate the sound speed which depends on both variables. However, the sound-speed equation of state c_{eos} is weakly dependent on the salinity, hence the contribution from the error in estimating

salinity to the error in estimating sound speed is small. For example, the error made between a sample salinity on the 1025.2 kg/m^3 isopycnal and the estimated salinity using the empirical salinity-temperature relationship evaluated at the sample temperature is at worst 0.085 PSU. This deviation in salinity contributed at most 0.1 m/s error to the sound-speed estimate, which was less than or equal to other uncertainties. The root-mean-square error of sound speed from the error in salinity is 0.03 m/s.

1.3.2 Acoustic Observations

Over various short-range acoustic transmissions during the experiment, the matched-filtered sequences had between two and four arrivals from refracted ray paths at ranges of less than 3 km at a source depth of 200 ± 4 m. Figs. 1.7a,c,e show the intensity of recorded acoustic arrivals from single matched-filtered sequences over the entire receiver array near the middle of the transmission intervals T1, T2, and T3. Figs. 1.7b,d,f show a series of arrivals from multiple matched-filtered sequences on single hydrophones during the minute-long transmission of T1, T2, and T3. The display of arrivals in the left column is generally referred to as a timefront, with each separate line of arrivals referred to as a branch. The observed timefront contained multiple branches separated within milliseconds of each other and a longer-delayed branch that likely was reflected from the surface. This paper focuses on the refracted arrival branches that do not scatter off the surface. Only a single matched-filtered sequence over the array is shown in Figs. 1.7a,c,e because the shape of the observed timefronts did not vary much over each one-minute transmission interval, however, the location of the timefront with respect to arrival time and depth does vary slightly due to the small changes in source depth and transmission range.

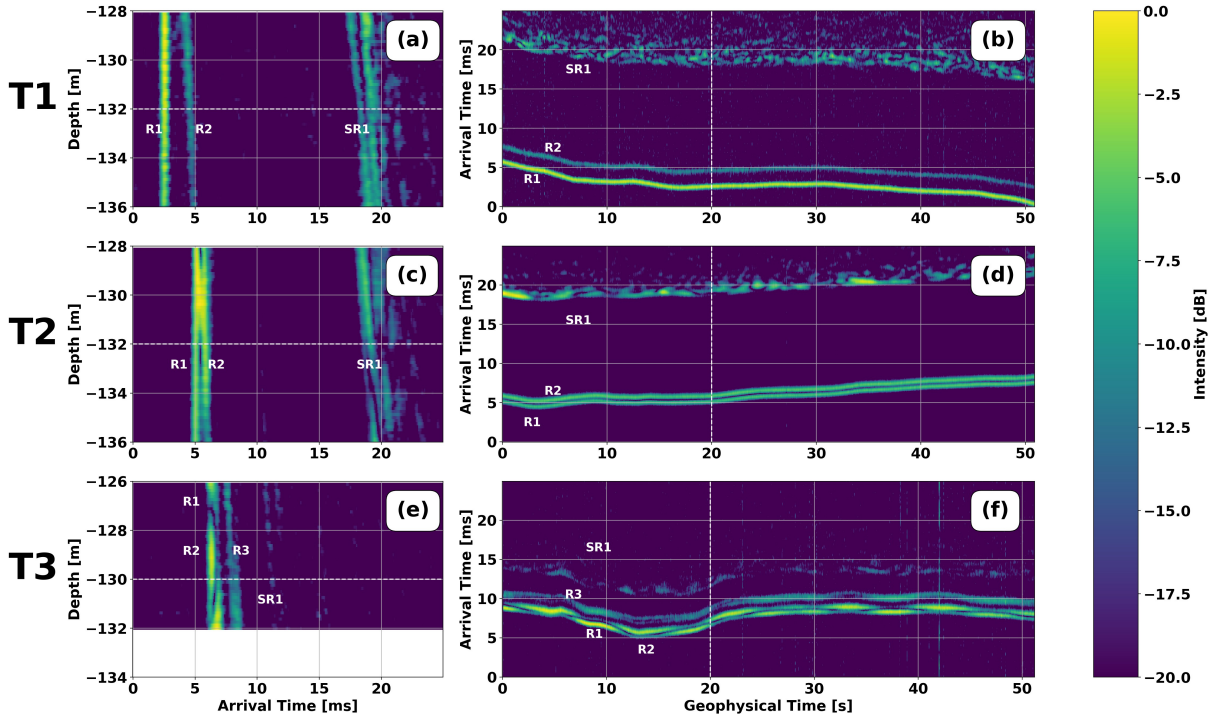

Figure 1.7. Observed matched-filtered acoustic arrivals on different days with varying ranges between 1.7 and 2.5 km. Figs. 1.7 b,d,f show the geophysical time evolution of arrivals for T1, T2, and T3 over one minute, with the arrival intensity shown in color and the relative arrival time on the vertical axis for a single hydrophone centered in the middle of the array shown as the horizontal white dashed line on the left column. The arrival intensity is relative to the maximum arrival intensity recorded on the array for each snapshot and is reported in decibels. Figs. 1.7a,c,e show the arrival intensity for T1, T2, and T3 in color with the relative arrival time on the horizontal axis and hydrophone depth on the vertical axis for a single transmission at the time marked by the vertical dashed line on the right column. Each transmission contained multiple arrivals labeled with an 'R' for a refracted and an 'SR' for a surface reflected. The bottom 16 hydrophones in the array lost power during T3, and so there is a blank space in Fig. 1.7e where no data is available at those depths.

During transmission T1, shown in Fig. 1.7a, the array received two refracted arrivals and one surface-reflected arrival from the source at a range of 1.7 km. The first two refracted arrivals R1 and R2 had a time separation of 1.5 ms. The time separation between the two arrivals is smaller at the top of the array than at the bottom suggesting a difference in their angle of arrival at the receiver. During transmission T2, shown in Fig. 1.7c, the array also received two refracted arrivals and one surface-reflected arrival at a range of 1.9 km. These arrivals were similar to the arrivals in T1, although, R1 and R2 overlapped at a depth of 130 m near the top half of the

array. The intensity of the arrival appears to increase where R1 and R2 overlapped. During transmission T3, shown in Fig. 1.7e, the array received 4 arrivals, three refracted and one surface reflected, at a range of 2.5 km. Arrivals R1 and R2 overlapped at multiple locations. Arrival R3 did not overlap with the first two. It is possible that R3 is two interfering paths because R3 temporarily appears to split, at geophysical time 32 seconds and arrival time 10 ms, into two smaller arrivals, see Fig. 1.7f. Arrivals shown in Figs. 1.7a,c,e are attributed to ray triplications which allow for the arrivals to have small time separations.

The arrival intensity structure along the array, shown in Figs. 1.7a,c,e, is projected into the temporal variability of arrival intensity recorded on a single hydrophone, shown in Figs. 1.7b,d,f. The rapid changes seen in the time evolution of the refracted arrivals during T3, Fig. 1.7f, can be explained by the overlapping arrivals seen along the timefront in Fig. 1.7e sweeping across a single hydrophone over time. The surface waves – which were particularly strong during T3 – caused the ship to heave, resulting in the source depth changing by ± 4 m with a period of ≈ 7 seconds. Ray simulations showed that an upwards source motion shifts the arrival depth of a triplication downwards, and conversely shifts the triplication upwards for a downwards source motion. The pattern of intensity along the time front (Fig 1.7e) is visible in the time record in (Fig. 1.7f) as a series of interleaving paths due to the motion of the acoustic source. This effect can be removed by sampling transmissions that had the same source depth, but the effect illustrates how structure along the timefront can impact the time series of arrivals for a single hydrophone.

1.4 Model

1.4.1 Ray Triplication/Wavefront Folding

A ray model illustrates the change in acoustic propagation due to the sound-speed fine structure. A two-dimensional (r,z) range-independent ray trace is simulated using a sound-speed profile from T1, see Fig. 1.8a, which is the same sound-speed profile shown in Fig. 1.4a. Rays

were traced at constant launch angle increments of 0.05 degrees over a range of 1.8 km, shown in Fig. 1.8b. Ray angles throughout the ray trajectory are defined from the horizontal axis with rays approaching the surface having positive ray angles and rays approaching the bottom with negative ray angles.

Caustics form when the spatial separation between two rays, separated by an infinitesimally small launch angle, decreases to zero[28]. Rays near a caustic cross over each other creating a triplication, see the upper left corner of Fig. 1.8b. Caustics occur at the folding points of timefronts, where $dz_f/d\theta_0$, the derivative of ray depth at the range of the receiver, z_f, with respect to the launch angle θ_0, changes sign[4]. The color of the rays in Figs. 1.8b,c changes when $dz_f/d\theta_0$ changes sign. The ray arrivals at a 1.8 km range in Fig. 1.8c contain two triplications near 60 and 110 m depth. These triplications stem from rays with turning points between 50-60 m and 90-120 m depth. At 55 and 100 m depth, U_{10} is 5.1 and 5.8, respectively. The relative curvature at these depths is sufficient to form triplications for rays with nearby turning points.

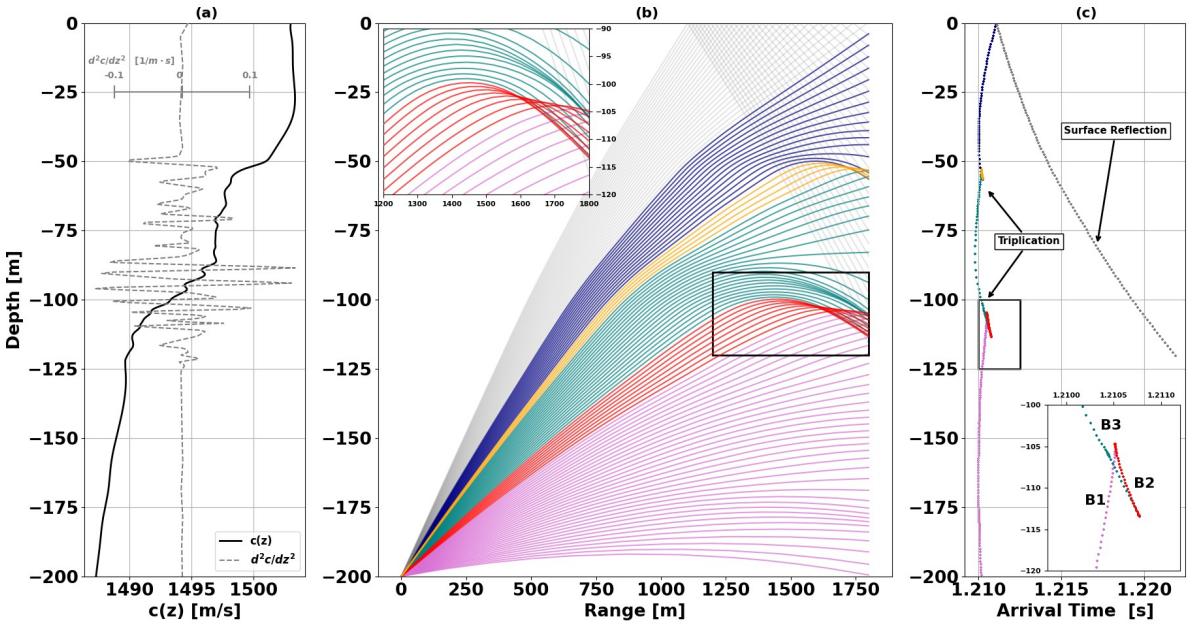

Figure 1.8. A ray trace simulation using the sound-speed profile from T1 is shown in Fig. 1.4 and redrawn in Fig. 1.8a (black line) in combination with the second derivative in sound speed (grey line). Fig. 1.8b shows a ray trace over 1.8 km with an inset plot that focuses on rays forming a triplication. Ray bundles, highlighted with different colors in Fig. 1.8b, are delineated by the change in sign of the derivative of ray arrival depth with respect to launch angle, $dz_f/d\theta_0$. The rays that are reflected from the surface are shaded in light grey. The inset plot in Fig. 1.8b focuses on rays that pass through caustics and continue to cross over each other. Fig. 1.8c shows the ray arrival time versus ray arrival depth at a 1.8 km range. The inset plot in Fig. 1.8c focuses on the triplication area near 110 m. Each branch of the triplication in the inset plot is labeled B1, B2, and B3.

The ray arrivals related to the triplication near 110 m form a swallow-tail pattern, see the inset plot of Fig. 1.8c. The three branches B1, B2, and B3 of the triplication are labeled in Fig. 1.8c. Branch B1 (magenta rays) consists of rays with positive angles with an average of 1°. The arrival angle of rays along the triplication goes through zero at the top of the triplication where Branches B1 and B2 connect. The ray angles on B2 (red rays) are negative with an average of $-3.3°$. Ray angles on Branch B3 (teal rays) increase slightly after passing through the bottom of the triplication and have an average angle of $-3.0°$. Branch B3 has the lowest intensity of the three branches as seen by the increase in spacing between ray arrivals, and the ray angles are very similar to Branch B2. Branch B3 might not be resolved in the observations for those two

reasons. Arrivals from triplicated ray paths plausibly explain observations of closely separated and overlapping arrivals with varying intensities.

The formation of the triplication related to the arrivals near 110 m depth starts near the caustic between 1200-1800 m in range and 90-120 m in depth which is shown in the upper left corner of Fig. 1.8b. Figs. 1.9a,b focus further on the area where the wavefront starts to fold due to the fine structure at those depths. Fig 1.9a shows the value (black line), first (blue line), and second (green line) derivative of the interpolated sound-speed profile between 92-105 m depth. The propagation of the simulated wavefront, curves in r, z space of constant travel time, is shown in Fig. 1.9b between 1450-1600 m in range by 92-105 m in depth. Each wavefront is sampled every 10 ms in travel time starting at a relative initial travel time of 0 ms. The range variability along each wavefront is a few centimeters, whereas the range separation between each wavefront is 15 m. The mean range separation between each wavefront in Fig. 1.9b is reduced from 15 m to 5 cm to emphasize the along-wavefront variability relevant to triplications.

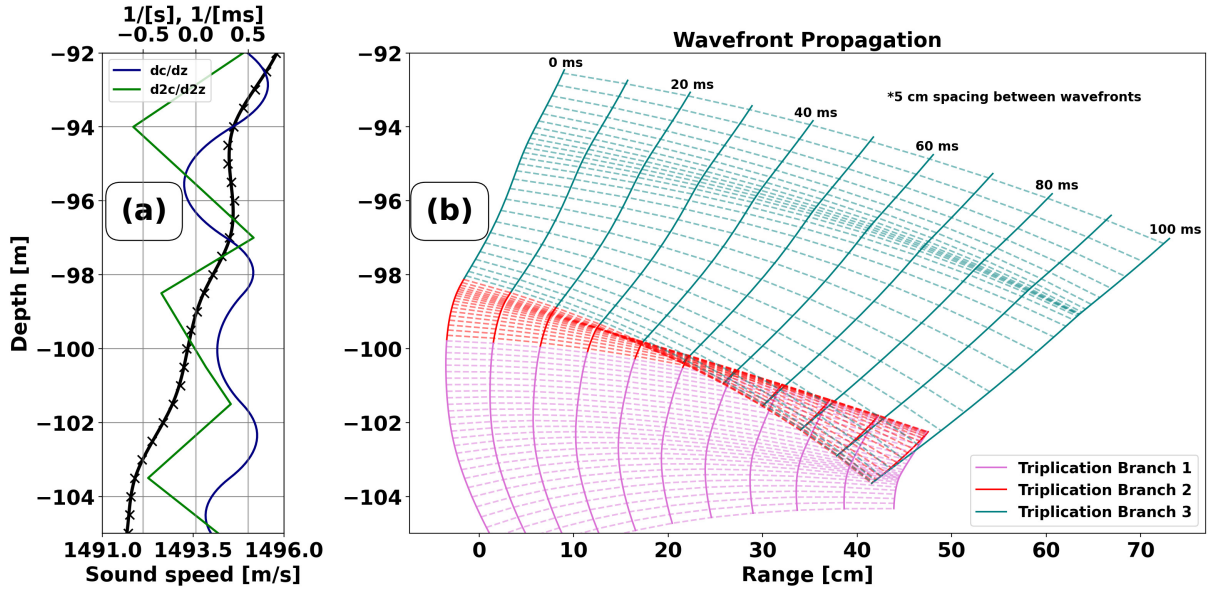

Figure 1.9. (a) An example sound-speed profile between 92-105 m, shown on the left side (black solid line), contains multiple 'step-like' structures that have non-trivial second derivatives (green solid line) in sound speed with respect to depth by alternating the first derivative in sound speed (blue solid line). (b) Wavefronts at 10 ms travel time intervals are calculated from simulated rays between ranges of 1450 and 1600 m. Solid lines represent the wavefront, a curve of constant travel time, and the dashed lines represent acoustic rays. The mean range separation between each wavefront is re-scaled from 15 m to 5 cm to emphasize the curvature along the wavefront. The wavefront folds over itself as it propagates which forms a triplication near 102 m depth. The colors magenta, red, and teal each represent a different branch of the triplication for the wavefront with a 100 ms travel time.

The wavefront begins converging near depths of 94, 98, and 104 m. At these depths, the second derivative of sound speed (Fig. 1.9a green line) has negative extrema, which cause the rays in the vicinity of these depths to progressively squeeze together. The wavefront near 100 m depth and 40 ms travel time converges to a focal point (caustic), after which the wavefront folds over itself. The wavefront tends to fold in areas where the rays are near horizontal, so the wavefront is aligned vertically, making it more sensitive to the vertical changes in the sound-speed profile [3]. The curve $r(z)$ that describes the wavefront range as a function of depth is multi-valued across the fold. The colors of the wavefront in Fig. 1.9b correspond to the three branches of the triplication shown in Fig. 1.8c. From the ray point of view, the folding of the front involves neighboring rays crossing over each other, allowing for three rays with distinct

travel times to occupy the same point in space where the wavefront has folded.

This fold shown in both the wavefront, shown in Fig. 1.9b, and in the timefront, shown in the inset plot of Fig. 1.8c, demonstrates how ocean fine structure allows for distinct ray paths that have small vertical separation while still arriving at the same depth at short ranges. For example, rays on branches B1, B2, and B3 that intersect 110 m depth at a range of 1.8 km had maximum vertical separations of 12, 19, and 9 m between their respective rays paths at a range of 1.5 km where the rays on branches B2 and B3 start to turn.

1.4.2 Model Comparison

The PE model is compared to the ray model by overlaying ray arrivals on top of the PE simulated intensity shown in Fig. 1.10 for each transmission. Both simulations used the estimated transmission ranges, source depths, and sound-speed profiles from the three transmission periods, see Fig. 1.7. The PE simulations used the spectral shape of the pulses sent during the experiment. Figs. 1.10b,d,f show simulated acoustic receptions that have the same pulse shape, source depth, and range as the simulated receptions shown in Figs. 1.10a,c,e, but use sound-speed profiles smoothed by convolving a 12-meter boxcar window with the interpolated sound-speed profiles for T1, T2, and T3. Smoothing the sound-speed profile of T1, T2, and T3 decreases the depth-mean U_{10} of each profile down to 2.9, 2.8, and 3.0, respectively. Figs. 1.10b,d,f show the change in PE and ray timefront when the fine structure is removed by smoothing. To further quantify the effect of smoothing the sound-speed profile, this smoothing technique is applied to the interpolated sound-speed profiles with various window lengths and the resulting simulated propagation is compared to the observations in Section 1.5.

The intensity along the ray timefront can be estimated from the arrival depth separation between successive rays because the rays have uniform increments in launch angle. Each transmission has at least two branches of arrivals. Branches that reflected from the surface are labeled ‘SR’, and branches that were wholly refracted are labeled with ‘R’. Along each refracted branch there are in general extra branches that are created by the ray triplication process.

Simulated arrival branches that are associated with the observed arrivals are labeled the same as in Fig. 1.7. Not all the branches can be associated with the observations because the aperture of the array, see Fig. 1.7a, is small compared to the depth range of the simulated timefront. The overall structure of the PE and ray timefront tend to agree, although, in some areas, PE simulated energy appears where the rays are shadowed e.g. Fig. 1.10a between 125-150 m.

Figs. 1.10 a,c,e show simulated output using unsmoothed sound-speed profiles for transmissions T1, T2, and T3, which are ordered by increasing range. T1 appeared to have the least amount of complexity in the timefront, based on the number of branches and the intensity variability, while T3 had the most. Timefront complexity thus increased with range, as might be expected. T1 and T2 show branches, e.g. R2, extending from ray triplications near depths of 50, 100, and 125 m. The strong sound-speed gradient at the base of the mixed layer, see Fig. 1.4c, during transmission T3 explains the discontinuity between 25-50 m depth and additional arrival branch, R3, in the timefront shown in Fig. 1.10e, that do not occur in the T1 or T2 timefront.

The change in acoustic amplitude described by the ray model is governed by the convergence and divergence of the ray tube which depends on the second derivative of sound speed along the ray path [18, 4]. Areas of high intensity appear near points where the timefront splits into two arrival branches, e.g. near 110 m between R1 and R2 in Fig. 1.10a. This split is the top part of the triplication shown in Fig. 1.8c. This area of high intensity is associated with a caustic. The simulated arrivals retain areas of high intensity at depths where the unsmoothed simulated timefront folds over because the second derivative of sound speed in those areas is strong enough to significantly focus the acoustic energy, even after smoothing.

The PE and ray simulations tend to agree on the location of caustics along the timefront, however, the PE simulations show energy extending from the caustics in the timefront which are not paired with ray arrivals. This is most clear for the caustic in Fig. 1.10a near 110 m depth. Both ray and PE simulated receptions show a second arrival branch, R2, in the timefront underneath the caustic. R2 calculated from geometric ray tracing terminates at a depth of 112 m whereas R2 calculated with a full-wave PE simulation extends to a depth of 140 m. This

extension of energy is asymmetric with more energy scattered below than above the triplication. The ray trace does not model the extension of energy but does predict areas of triplication that appear to be the source of this extension.

The PE model includes information about the acoustic wavelengths within the bandwidth of the experimental transmissions, and models wave scattering when the wavelength is comparable to or larger than the length scale of the changes in sound speed. Hence, when the sound-speed profiles are smoothed with a 12 m window length, the PE simulated transmission of T1 and T2 lose their R2 arrival branches, and the energy below 125 m for T2 and T3 appears less scattered across the timefront because the vertical length scales of the sound-speed profiles are increased by smoothing. The vertical Fresnel zone, $R_f \approx 1/2(\sqrt{\lambda R})$, can quantify the acoustic sensitivity to vertical scales in the sound-speed profile[4]. The vertical Fresnel zone for ray paths connected to arrivals R1 and R2 is approximately 10 to 20 m based on the bandwidth of the pulses. This calculation assumes a free-space medium and the curvature of the waveguide can make the Fresnel zones much smaller [4].

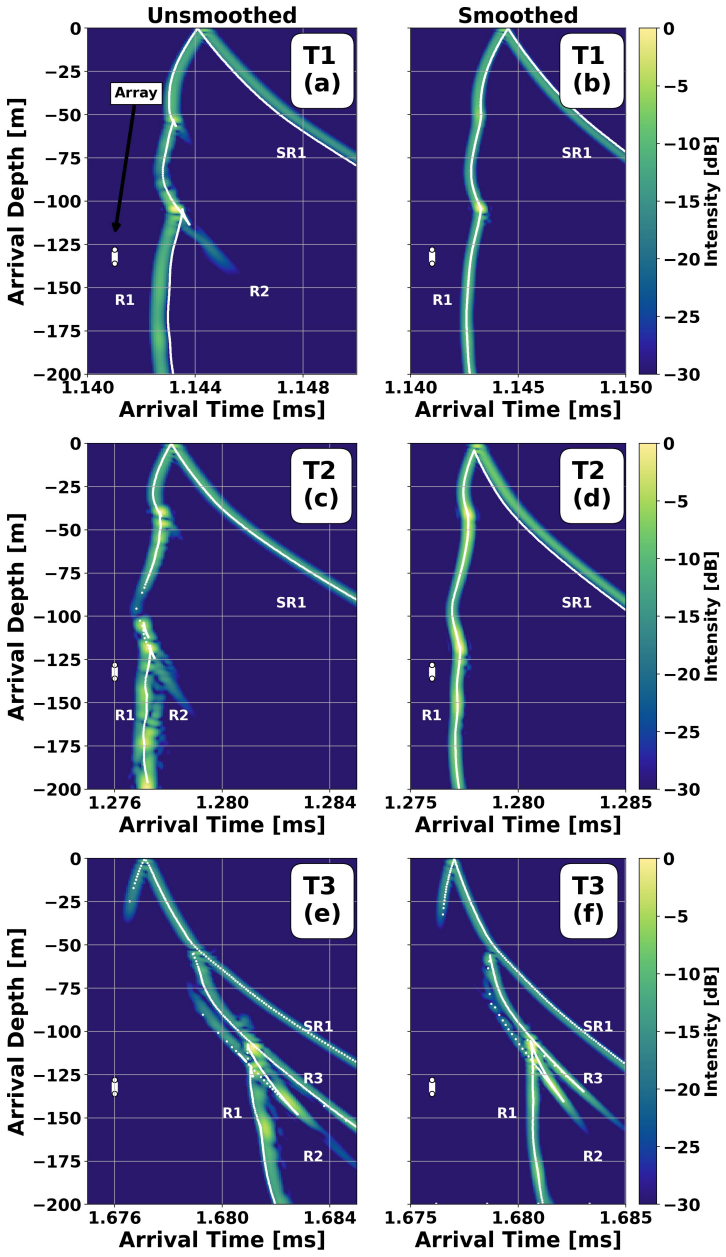

Figure 1.10. Three simulated acoustic arrivals using sound-speed estimates shown in Fig. 1.4 with and without sound-speed smoothing. Figs. 1.10a,c,e show the simulation of transmission T1, T2, and T3 at ranges of 1.7, 1.9, and 2.5 km respectively without any smoothing to the sound-speed profiles. Figs. 1.10b,d,f show the simulations in Figs. 1.10a,c,e with a 12 m smoothing window applied to the sound-speed profile. Intensity calculated by the PE simulation is shown relative to the maximum arrival intensity in decibels with color. Ray arrivals are shown as white dots. Each branch of the timefront observed by the receiver is labeled with the same arrival labels in Fig. 1.7. The scale and depth of the experimental array aperture are shown in each figure on the left-hand side between depths of approximately 128-136 m.

1.5 Results

1.5.1 Model-Observation Comparison : Intensity

A deterministic comparison was made between arrivals observed over the array and PE simulations of arrivals for each of the three transmission periods. Fig. 1.11 compares the intensity of the observed and simulated pulses. The intensities are shown in decibels in Fig. 1.11 and are relative to the maximum arrival intensity recorded on the array during the snapshot. Figs. 1.11a,c,e show a snapshot of a single pulse arrival (expanded view of Figs. 1.7a,c,e) within the same minute interval as the simulated result shown in Figs. 1.11b,d,f. The range of the transmission can be estimated with the measured travel time and sound speed but has an uncertainty of roughly 30 cm. A single travel time offset is used to align the observed and simulated timefronts along the center of the time delay axis. These comparisons show good visual agreement demonstrating that the closely spaced arrivals observed during the experiment were consistent with ray triplication created by oceanographic fine structure in the sound-speed profile.

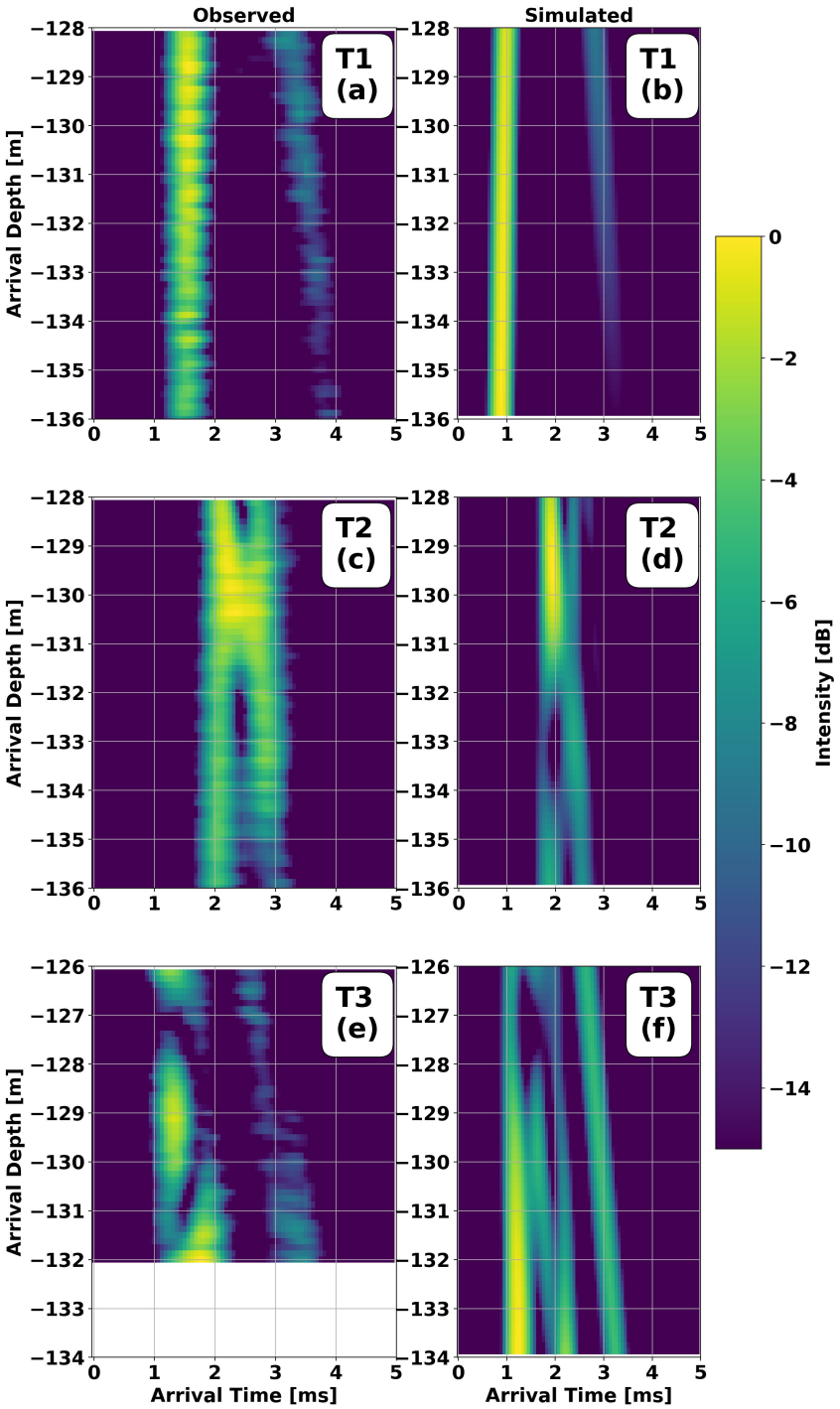

Figure 1.11. Three snapshots of observed pulses from the experiment (left column), and modeled pulse propagation (right column) using sound-speed profiles within 2 km. Figs. 1.11a,b show observed and simulated arrivals from T1, Figs. 1.11c,d T2, Fig. 1.11e,f T3. The intensity of arrivals relative to the maximum arrival intensity is shown in decibels with color over the 7.875 m array aperture for an arrival time window of 5 ms. The arrivals are centered in each plot, with the travel times adjusted to match because of the uncertainty in the transmission range.

The interpolated profiles in Figs. 1.4a,b,c and the measured source-receiver geometry were used to make a set of baseline PE simulations, see Figs 1.11b,d,f, for each transmission. Another set of simulations was made with perturbations to the range, source depth, and sound-speed profile. The simulations, perturbed and unperturbed, were compared to the observed intensity along the array with a correlation, r, a skill score, SS, and mean squared error relative to noise, MSE_r, see Table 1.1. The r value measures the correlation between the amplitudes, which is less sensitive to the difference in magnitude between two received pulses than to the difference in pulse shape, whereas the skill score and MSE_r are sensitive to the difference in the magnitude and shape between the received pulses, and has a larger range of values over the set of comparisons. These metrics quantify the importance of each parameter to the difference between observed and simulated arrival amplitudes. Appendix A describes how these metrics are computed from the data.

In general, the PE simulations using a well-resolved sound-speed profile near the turning point and the correct acoustic parameters predicted the number of observed arrivals and replicated the relative travel time separation between those arrivals. The variation in intensity along each arrival branch was not as well replicated in the simulations shown by the lower values of skill score compared to the correlation. The agreement between the observed and simulated intensity was more sensitive to changes in the sound-speed profile than to small changes in the range or source depth. The last row of Table 1.1 uses sound-speed profiles made solely from the thermistor-chain measurements, shown in Fig. 1.4a,c, without supplemental measurements from the Wave Glider. The simulations in the first row of Table 1.1 used sound-speed measurements from the Wave Glider which were made at the turning point depth and roughly 100 m and 2 km away from the turning points in range during T1 and T3, respectively. The correlation between observation and simulation decreased by 11% for T1 and 30% for T3 when solely using the thermistor-chain measurements at the turning point depths. The thermistor measurements were 1.5 km and 4 km, respectively, away from the turning point in range. The decrease in correlation emphasizes the importance of measuring the sound-speed profile near the turning point of the

Table 1.1. Values of the correlation, r, skill score, SS, and relative mean squared error, MSE_r, quantify the difference between the observed and simulated arrival amplitudes. The rows in the leftmost column dictate the type of perturbation made to the simulation's parameters. Each column corresponds to a transmission with sub-columns for each metric. The unperturbed row uses the range, source depth, and sound-speed profile that best match the acoustic transmission. The range and source depth of the simulations were perturbed and their agreement with the observations is reported in the middle rows. Simulations using sound-speed profiles measured farther away from the turning point of the acoustic path are available for two transmissions. Comparisons between observations and those simulations are listed in the last row.

Perturbation	T1		
	r [%]	SS [%]	MSE_r [dB]
Unperturbed	93	80	−24.17
Range +50 m	90	80	−23.48
Range −50 m	93	76	−23.37
Source Depth +3m	93	79	−23.77
Source Depth −3m	92	79	−24.07
Alternative Profile	83	58	−21.60
Perturbation	T2		
	r [%]	SS [%]	MSE_r [dB]
Unperturbed	90	80	−23.32
Range +50 m	88	74	−22.56
Range −50 m	88	71	−22.26
Source Depth +3m	88	74	−22.44
Source Depth −3m	89	76	−22.54
Alternative Profile	–	–	–
Perturbation	T3		
	r [%]	SS [%]	MSE_r [dB]
Unperturbed	72	64	−19.73
Range +50 m	59	48	−17.72
Range −50 m	62	56	−18.62
Source Depth +3m	49	42	−16.72
Source Depth −3m	70	64	−19.56
Alternative Profile	50	28	−16.24

acoustic transmission.

In another perturbation experiment, the sound-speed profile closest to the turning point was smoothed by convolving a box-car window with the profile for window lengths of 2, 4, 8, 12, and 20 m. The sensitivity simulation indicated that modifying the sound-speed profile by vertical smoothing reduced the number of arrivals overall, decreasing both the correlation and

skill score, see Fig. 1.12. The correlation is not as sensitive as the skill score and flattens off after a smoothing window length of 8 m. The skill score decreased monotonically as the sound-speed profile smoothing window length increased. The decrease in skill score between 0 and 2 m window length is smaller than 2 to 4 m window length, indicating structures under 4 m need to be resolved in the sound-speed profile in order to adequately match the simulated pulses to observations, although higher resolution improves the match.

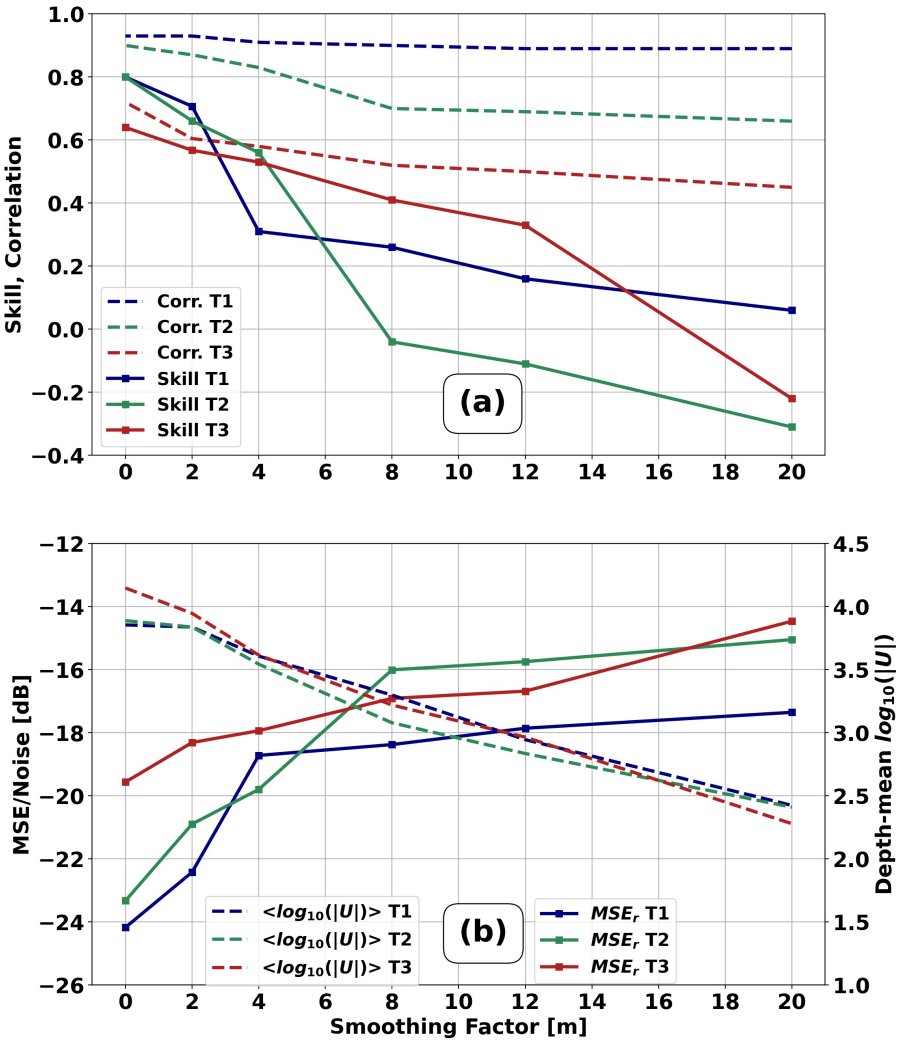

Figure 1.12. Values of skill score (solid line) and correlation (dashed line) between observation and simulation for the three transmissions T1 (blue line), T2 (green line), T3 (red line) as a function of window length (smoothing factor) used to smooth the sound-speed profile are plotted in the Fig. 1.12a (top). The mean-squared error between observation and simulation divided by the squared amplitude of the observed noise in decibels (solid lines) and the depth-mean $log_{10}(|U(z)|)$ of the sound-speed profile (dashed lines) for T1 (blue line), T2 (green line), T3 (red line) are plotted as a function of the window length used to smooth the sound-speed profile in Fig. 1.12b (bottom).

The drifting nature of the experiment made it difficult to position the oceanographic platforms so that they could measure the range variability along the acoustic propagation path. The agreement between our range-independent simulations and the acoustic observations gives us confidence that our range-independent assumption is reasonable. Additionally, two range-

dependent environments were made to test the sensitivity of the simulated propagation to horizontal sound-speed variability. Lacking horizontally-separated sound-speed measurements along the transmission path between the source and receiver, we convert hour-long and 30-minute-long time series of sound-speed profiles, see Fig. 1.5, centered on Transmission T2 into a spatial series by spacing each profile in range by a fixed distance.

The 30-minute and hour-long series separate consecutive profiles in range by 67 and 33 m respectively. These range-dependent simulations test cases where the range dependence of the sound channel is strong. The ratio between the spatial to temporal decorrelation scale of the sound speed, approximately 4 km per 24 minutes, would suggest a profile every 167 m. Even with 67 and 33 m horizontal separations, adding horizontal range dependence to the simulation did not greatly affect the arrivals at the 1.9 km range. The hour-long series was 92% correlated with the range-independent simulation. The 30-minute-long series was 95% correlated with the range-independent simulation. Neither of the range-dependent simulations increased the agreement between observation and simulation which is expected since the range-dependent simulations do not have the true range dependence for those transmissions.

1.5.2 Model-Observation Comparison : Phase

The phases of the 4 kHz carrier frequency along the array for a single MLS transmission in the middle of the minute-long series from the observations, see Figs. 1.13a,c,e, were computed from the output of the matched filter on the demodulated receptions[34]. The phases of the simulated propagation, see Figs. 1.13b,d,f, were evaluated as the angle between the complex components of the base-band pulse. Values that have lower than -15 dB intensity are not shown in the figures. It is not possible to compare the absolute phase between the simulation and observation because the range uncertainty is greater than 30 cm, which is the amount of range required to change the phase by 1 cycle. A single phase offset is added to the simulated phase so that it is easier to compare the simulated to the observed phase along each arrival depth.

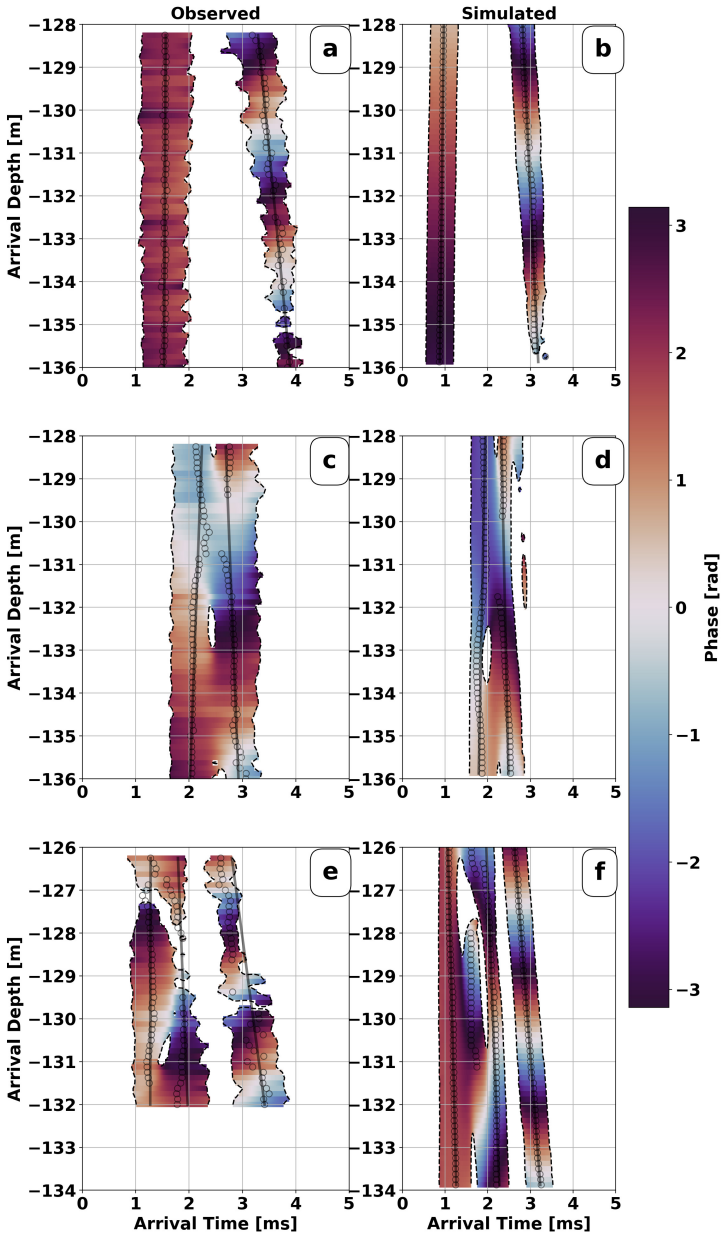

Figure 1.13. A comparison between observed and simulated arrival phase. Arrival phases that have an arrival intensity of -15 dB less than the maximal arrival peak are not shown. Fig. 1.13a,c,e show the observed carrier phases along the array for a single transmission during T1, T2, and T3, respectively. Figs. 1.13b,d,f show the simulated carrier phases of transmissions T1, T2, and T3 with a single phase offset allowed to ease the comparison between observed and simulated phases. Circle markers show the location of peak intensities of each arrival with the solid lines showing a linear fit to those peak arrival times along the vertical axis.

The angle of arrival, θ, of the wavefront with respect to the array is estimated using both the rate of change in phase and travel time over the vertical span of the array. The estimated angle

of arrival, $\hat{\theta_\tau}$ and $\hat{\theta_\phi}$, is congruent to the ray angle defined by the ray coordinate system. The travel time and phase are evaluated at the peak values of the received arrival amplitude. These peaks are shown as circles in Fig. 1.13. A line is fit to peak phase and travel time measurements and the slope is used to estimate the rate of change in both quantities along the array. Equation (1.2),

$$\hat{\theta_\tau} = tan^{-1}\left(\left[\frac{d\tau}{dz}\right]c\right) \tag{1.2}$$

is used to estimate angle $\hat{\theta_\tau}$ with travel time where $\frac{d\tau}{dz}$ is the change in arrival time with respect to depth, and c is the local sound speed. Equation (1.3),

$$\hat{\theta_\phi} = tan^{-1}\left(\left[\frac{d\phi}{dz}\right]\frac{c}{\omega}\right) \tag{1.3}$$

is used to estimate angle $\hat{\theta_\phi}$with phase where $\frac{d\phi}{dz}$ is the phase rate with respect to depth, ω is the angular frequency, and c is the local sound speed.

The angle of arrival estimates are reported in Table 1.2. The difference between observed and simulated arrival estimates is at most a few degrees, which demonstrates the capability of the simulation to accurately represent the phase distribution over the array. The average difference between observation and simulation angle estimates using travel time was 1°, and using phase was 1.6°. Differences were greatest for T3 and least for T1 as expected. The overlap of arrivals for both T2 and T3 leads to some disagreement between the phase and travel time angle estimate. For example, the phase estimate of the second arrival angle for T2 differs by 1.9° from the travel time estimate of the arrival angle. When two pulses overlap in arrival time the phase underneath the envelope of the overlapping pulses is affected by both the phase and amplitude of the two pulses. This interference can cause the phase to deviate from a constant rate of phase change along the array. The overlapping of arrivals can also change the envelope shape, therefore, adding uncertainty to the travel time estimate of the arrival angle, but to a lesser extent than for the phase estimate.

The ray trace using the sound-speed profile from T1 predicted a single arrival at the depth of the array. The PE simulation correctly models the energy that was received on the array during T1 with an estimated arrival angle within a degree of the observed arrival angle. Branch 2 of the triplication, shown in Fig. 1.8c, is connected to the extension of energy, shown in Fig. 1.10a. In the ray trace, Branch 2 has a $-3.3°$ arrival angle, whereas the estimated angle from the observation was $-6.6°$. The angle of the received wavefront from the caustic extension must steepen as it reaches the depth of the array, which would explain the discrepancy between the observed arrival angle and ray angle.

Table 1.2. Estimated arrival angles for different transmissions T1, T2, and T3 for both observations (DATA) and simulations (SIM) are reported in each row. The left half of the table shows the travel time estimates of arrival angles. The right half shows the phase estimates of arrival angles. Each column delineates the arrival numbers which are ordered by the time of arrival. A dashed line in the table means that particular arrival was not received during the transmission.

Transmission	Arrival Angle					
	Travel Time Estimate			Phase Estimate		
	1st	2nd	3rd	1st	2nd	3rd
T1 (DATA)	$0.35°$	$-6.6°$	–	$0.42°$	$-6.2°$	–
T1 (SIM)	$1.18°$	$-5.3°$	–	$1.18°$	$-4.9°$	–
T2 (DATA)	$2.7°$	$-3.3°$	–	$1.7°$	$-3.7°$	–
T2 (SIM)	$1.7°$	$-3.5°$	–	$1.4°$	$-1.8°$	–
T3 (DATA)	$0.1°$	$-2.7°$	$-9.1°$	$-4.3°$	$-3.8°$	$-9.4°$
T3 (SIM)	$0.5°$	$-3.8°$	$-6.4°$	$-0.6°$	$-5.1°$	$-6.8°$

1.5.3 Time Evolving Amplitude Comparison

A longer time series of acoustic arrivals during T2 was processed to compare the evolution of the arrivals over a few minutes to a simulated evolution. Fig. 1.14 shows a 10-minute record during T2 starting on 17 May 19:10 on a hydrophone at 129 m depth, which is above the interference of two arrivals shown in Fig. 1.7d. Fig. 1.14a shows all of the arrivals including the

surface arrival. The travel time of arrivals in Fig. 1.14a vary due to the varying range between the drifting array and the shipboard source. The range between source and receiver increased by 30 m over the 10-minute period on 17 May from 19:10 to 19:20. The relative time delay between surface and refracted arrivals was roughly constant over the 10-minute record which suggested the change in travel time could be corrected with a single time delay adjustment for each MLS reception.

The change in the arrivals due to sound-speed changes was isolated by removing the travel time effect of range and filtering for source and receiver depth changes within half a meter. A time-lag cross-correlation was calculated between the intensity of the two refracted arrivals from each reception and the intensity of the two refracted arrivals from the previous reception. The time lag with maximal cross-correlation estimates the change in travel time from one reception to the next. Those time-lags were then used to offset each reception so that the first refracted arrival is centered at time-delay 0 in Fig. 1.14b. The range was held constant in the simulation and so Fig. 1.14c is not travel time corrected with a cross-correlation. There are slight changes in the travel time of the arrivals shown in Fig. 1.14c due to the changing sound-speed profile, but these are small compared to the change in travel time caused by the increasing range in the observed data.

The two observed arrivals in Fig. 1.14b with intensities of -20 dB or greater are separated by 0.6 ms at the beginning of the record. These two arrivals combine near minute five into a merged arrival with a broader peak. The merging of the two arrivals happened in under one minute and changed the intensity of the acoustic reception. The time evolution of the arrival intensity at 129 m depth was simulated, see Fig. 1.14c, using a series of interpolated sound-speed profiles on 17 May from 19:10-19:20 sampled at one-minute intervals, which are highlighted with red in Fig. 1.5. The observed and simulated arrivals both display two separate arrivals that merge into a single arrival between minutes 4 and 5. Both the observed and simulated timefront over the full vertical span of the array preserve their 'X'-like pattern, see Figs. 1.11c,d, however, both timefronts moved upwards in arrival depth over the ten-minute interval. The movement of

the timefront caused the overlapping arrivals seen in Figs. 1.7c,d at 130 m depth to move to a depth of 129 m where the series of arrivals are recorded in Figs. 1.14b,c.

During this period of time, fine structure centered at 120 m was displaced upwards by 1 m highlighted by the green line in Fig. 1.5. Ray paths associated with the observed arrivals turn over at depths near 120 m, and so would be sensitive to a change in the position of the fine structure. Although, the range of the transmission is changing, Table 1.1 suggests that the arrival structure is more sensitive to perturbations in sound speed than range. The merging of two paths in Fig. 1.14c can be explained as an upwards shift of the timefront due to a meter scale displacement of the fine structure embedded in the sound-speed profile causing the interference point of the two arrivals in that timefront to sweep past the hydrophone at 129 m.

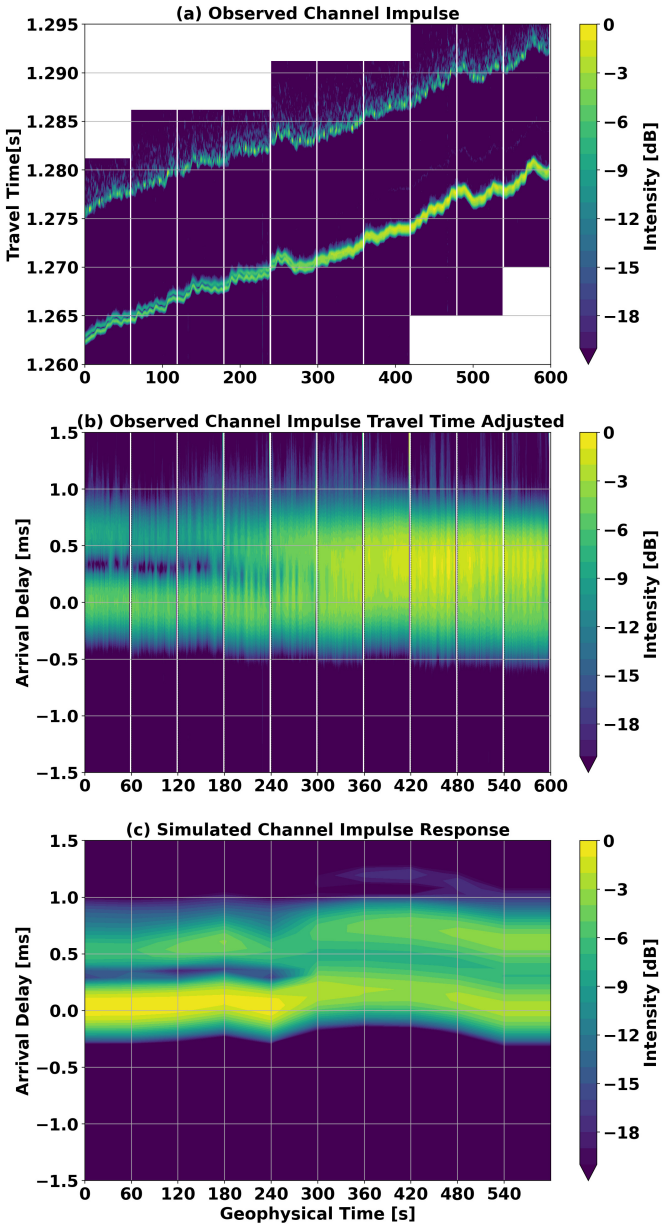

Figure 1.14. A time series of recorded (Figs. 1.14a,b) and simulated (Fig. 1.14c) acoustic arrivals on a hydrophone at 129 m depth, including T2, on 17 May from 19:10-19:20 with intensity relative to the maximum arrival intensity shown in color and travel time in seconds on the vertical axis. Fig. 1.14a,b have a white gap every minute because the phase-coded arrivals are processed on minute intervals, and the coded sequence length of 63.5 ms does not divide evenly into a minute. The travel time variability seen in Fig. 1.14a was removed in Fig. 1.14b by shifting each arrival by a time delay that maximizes the cross-correlation with the previous arrival. The arrival time axis is shrunk in Fig. 1.14b to exclude the surface arrival. Fig. 1.14c is a simulation of the refracted arrivals during the same time period using the series of sound-speed profiles measured at the same time as the transmissions shown in Fig. 1.5 (red profiles).

1.6 Discussion

The measurements in this paper identify sound-speed features that are important for modeling micro-multipathing. The rapidly repeated broad-band pulses are critical for resolving the path separation of the acoustic arrivals. The three examples of micro-multipathing in transmissions T1, T2, and T3 show receptions that have no interference, single interference, and multiple interferences, respectively. It was also typical to have multiple-interference arrivals for receptions with ranges greater than 2 km and less than 5 km, which are not shown in the paper. The short range of the transmissions is crucial for reducing the impact of range-dependent sound-speed perturbations in the channel. We would expect that at longer ranges, with multiple upper turning points, the paths would go through multiple triplications leading to saturation of the scintillation coefficient. This would increase the difficulty in sampling the sound speed and matching observed and modeled acoustic arrivals.

Full-wave simulations of mid-frequency acoustic propagation show triplication patterns similar to that of the ray simulation, which argues for the validity of arrivals that have distinct ray paths emanating from the triplication. The full-wave simulations also show energy extending into the geometric shadow zone of the ray simulation, which indicates that finite-wavelength effects are also relevant to micro-multipathing at mid-frequencies. We expect that at lower frequencies the agreement between full-wave and ray simulations would decrease as the Fresnel zone widens and diffraction smooths out the effects of small-scale features.

In general, reducing the relative curvature by smoothing the sound-speed profile reduces the number of caustics, which increases the mismatch between the smoothed-profile simulations and the observations. There is not, however, a threshold for how much relative curvature is needed to form a caustic. The lack of a threshold is partially due to the dependence of caustic formation on the geometry of the ray paths between the source and receiver. For example, the triplicated arrivals in the simulated transmissions of T1 and T2 vanish when the depth-mean U_{10} is reduced to roughly 3.0 with a smoothing window of 12 m, see Fig. 1.10. In contrast, the

simulated transmission of T3 which uses a smoothed sound-speed profile with similar depth-average U_{10} as T1 and T2, still contains triplicated arrivals. The slightly greater range of this transmission may be the reason for this difference, as triplications tend to grow with range. These observations only represent a small case study, not a comprehensive theory.

The importance of modeling additional ray paths related to strong second derivatives in sound speed lies in the interference of the arrivals. The interference of micro-multipath arrivals not only increases the scintillation but also creates ambiguity in the phase of the received acoustic pulse, see Fig 1.13c,e. As a consequence, caustics and micro-multipath interference from triplicated arrivals increase the sensitivity of the channel impulse response between source and receiver to the vertical position of those second derivatives. Weak vertical displacements of those second derivatives can cause strong fluctuations in acoustic intensity and phase, see Fig. 1.14, so internal waves with higher frequencies which tend to have lower energy can produce significant acoustic variability.

Further work is required to understand the correlation and time variability of micro-multipath arrivals specifically at short ranges where mid-frequency acoustic propagation is partially saturated – a regime of strong acoustic intensity variation due to strong focusing and interference[3]. Acoustic propagation modeling that includes realistic meter-scale vertical sound-speed variability could quantify statistics of micro-multipath interference. These statistics are important for understanding the scintillation as well as the phase decorrelation of the underwater acoustic channel.

ACKNOWLEDGEMENTS

Chapter 1, in full, is a reprint of the material as it appears in Journal Acoustical Society America 2023. Author list: DeFilippis, Jacob; Cornuelle, Bruce; Lucas, Drew; Hodgkiss William; Lenain, Luc; Kuperman, William; Alford, Matthew. The dissertation author was the primary investigator and author of this paper.

Chapter 2

Chapter 2: Measuring phase difference to sense small-scale ocean sound-speed structure

2.1 Introduction

We explore the information gained from ocean-fine-structure-related multipaths in mid-frequency sound propagation by analyzing observations from a short-range, broadband acoustic experiment. We focus on a 30-minute segment where two received pulses can be attributed to multipaths created by fine structure in the measured sound-speed profile[8]. The travel times and phases of the two receptions on a single hydrophone can be tracked for 30 minutes. The phases of the two arrivals evolve in time, driven by both changes in source/receiver location and the sound speed. The two arrivals provide an "interferometer of opportunity". The difference between the two arrival phases creates a measurement that is more sensitive to small-scale sound-speed perturbations, and less sensitive to range-related phase perturbations.

By analyzing the phase difference using a propagation model, we attempt to understand the travel time/phase changes that are predominantly driven by the vertical advection of small-scale structures in the ocean. Although broadband arrivals with small travel time separation are frequently observed in mid-frequency experiments, the temporal and spatial behavior of these paths is not well understood[48, 15]. The small-scale vertical structure of the ocean allows for

ray paths that can have small travel time and spatial separation, similar to how the large-scale structure in the sound-speed profile can create ray paths that have large travel time and spatial separation. The propagation launch angles in the experiment are only separated by a few degrees, and, at roughly 2 km range, the paths are vertically separated by at most 40 m. Even though the paths are similar, the received phases change at different rates, which points to the complexity of the short-range sound propagation.

2.2 Observations

On 7 May 2021, maximum-length phase-modulated sequences were transmitted from the R/V Revelle for 30 minutes. The drifting receiver array recorded those sequences at a range of about 1.8 km. Sequences are repeated every 63.5 ms with two cycles per digit and a 4 kHz carrier frequency. The effective bandwidth of these sequences is 4 kHz. During the transmission period, a thermistor chain measured the temperature and pressure within 0.5 km of the acoustic propagation's center point. The GPS positions of the source, receiver, and thermistor chain are shown in Fig. 2.1a. During the transmission period, the receiver drifted toward the ship, shortening the source-receiver range by approximately 50 m. The range of the transmission divided by the average sound speed is plotted in Fig. 2.1c. The average source depth was 200 m and the average receiver depth was 130 m both vary by about ± 2 m due to surface-wave heave on the ship and receiver buoy.

The recorded sequences are matched filtered to produce amplitude, travel time, phase, and Doppler. There are 28,320 matched-filter sequences in our 30-minute-long transmission. Three pulses appear in the matched-filter output, see Fig. 2.1b. The energy of the first two pulses is less scattered than the third pulse which is reflected from the ocean surface. The second arrival in this experiment could be considered a micro-multipath[3] of the first arrival because of the small spatial separation between the ray paths. Furthermore, for this 30-minute transmission, the second arrival exists for the entire interval, however, during the full experiment, the second

arrival fades in and out of the receiver suggesting it is not a stable acoustic path.

The travel time and phase of the pulses are evaluated at the peak of the pulse for each matched filter sequence in the 30-minute-long transmission. The travel times and phase difference of those two peaks are shown in Fig. 2.1c. The peak amplitude of these two arrivals is calculated using a peak-finding algorithm that evaluates the derivative of the matched-filter output above a 15 dB threshold and looks for zero points of the derivative. After the maximum point is found, a parabola is fit to the four points surrounding the maximum to interpolate to the maximum matched-filter amplitude between sampled points. The peak travel time, phase, and amplitude are calculated for the first two arrivals.

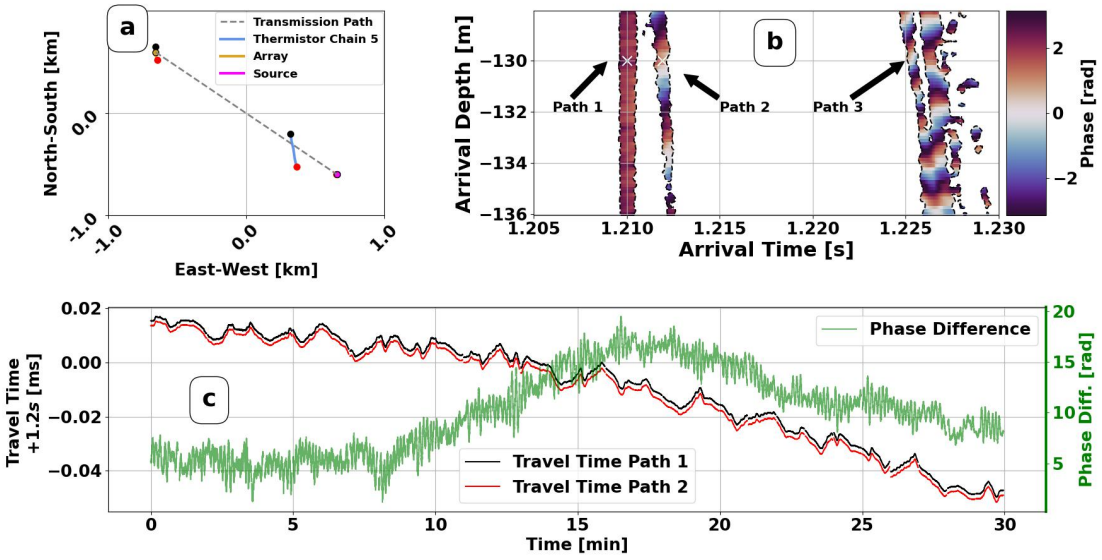

Figure 2.1. (a) The source, receiver, and thermistor chain positions between 19:30-20:00 on 7 May 2021 UTC. (b) Matched-filter output of phase above a 15 dB threshold of three arrivals on the array at 19:30. Peaks of the first two arrivals on a hydrophone at 130 m depth (see white 'X' marks) are tracked for thirty minutes. (c) The travel time of those arrival peaks is shown with the red and black lines. The estimated paths for those arrivals are shown in Fig. 2.2b. The grey-dashed line shows the source-receiver range divided by the average sound speed. The green line shows the difference in phase of the two arrival peaks.

The decreasing trend in the travel time for both arrivals is dominated by the decreasing source-receiver range. The $\pm$ 5 ms minute-scale travel time variability is also likely due to the

drifting horizontal motion of the receiver. The source-receiver range carries some uncertainty because the position of the source and receiver is not the same as the GPS position of the buoy or ship. However, the changes in travel time of the arrivals are similar, suggesting they may be similarly sensitive to the change in transmission range. Thus, the difference between the two travel times should constrain the range-related variability.

In addition to taking the difference in travel times, we take the difference in phase to exploit its stability. The phase provides information about the travel time, τ, because they are linearly related, $\phi = \omega\tau$, by the carrier angular frequency, ω. The phase has a 2π cycle ambiguity so the travel time can not be estimated from the phase, but the time-change in travel time can be estimated with the unwrapped phase. The error in peak-phase measurements, converted into travel time by dividing by the frequency, is $\pm 16\mu$s whereas the error in peak-travel-time measurements is $\pm 117\mu$s in our observations. The difference in the error is related to the stability of the pulse shape, specifically from the second arrival, which affects peak travel time more than the peak phase.

The unwrapped phase difference, see Fig. 2.1c, is absent of the range-related decreasing trend seen in the travel time observations. The phase difference amplifies disparate parts of the sound propagation for the two arrival paths. The observed phase difference includes minute-scale variability and smaller amplitude second-scale variability. Although the pulses are close in travel time and only propagate over a short range, the two arrivals differ in phase by $\pm 2\pi$ over 30 minutes – a 0.5 ms excursion in travel time difference.

2.3 Model

The phase difference of these receptions is modeled using measurements of the acoustic environment: source/receiver depth, range, and sound speed. There is a pressure sensor on the source and receiver array to get the depth of the two instruments. The range is calculated using the GPS position of the ship and the receiver buoy. The sound-speed profile from 0-200

m was estimated from the thermistor-chain temperature and pressure measurements during the transmission. Sound-speed profiles, see example in Fig. 2.2a, are sampled every minute and are estimated from a collection of thermistor-chain temperature and pressure measurements sampling at 2 Hz [8]. The thermistors are vertically spaced roughly every 2 m between 0-200 m depth. The salinity is estimated from the thermistor temperature measurements using the relationship between temperature and salinity derived from ship-board CTD casts.

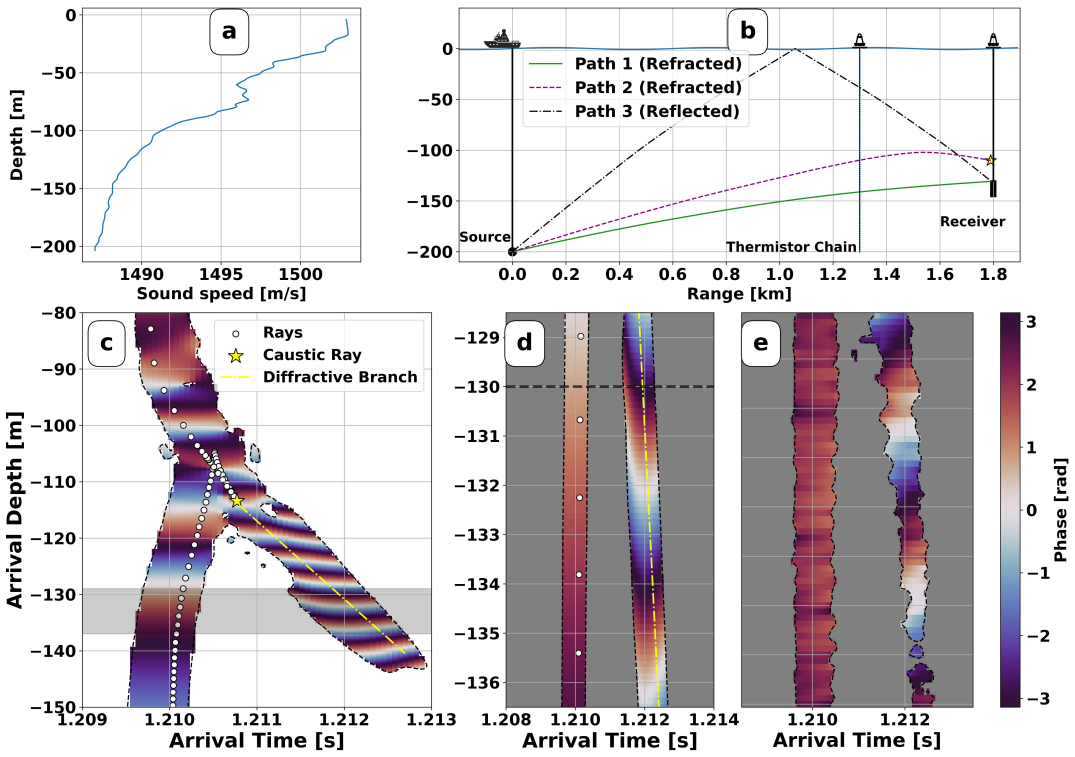

Figure 2.2. (a) A sound-speed profile at the measured at 19:30 7 May 2021 UTC. (b) A ray trace of three rays using the sound-speed profile in (a). (c) A PE simulation of acoustic phase at the source-receiver range between 80-150 m depth with rays laid on top for comparison. The star is the ray nearest to the bottom caustic of the triplication. The yellow dash-dot line represents an extension of the timefront using the angle of the ray nearest to the caustic. The gray box outlines the aperture of the receiver array. (d) The simulated acoustic phase between the aperture of the array, 128.5-136.5 m depth. (e) The observed acoustic phase along the aperture of the array.

Range-independent ray paths between the source and receiver are calculated to predict

the sensitivity of the arrival phases to the change in sound speed. The change in sound speed gradient between 100-150 m depth allows for two ray paths, see Fig. 2.2b, with launch angles of 3.3 and 5.5 degrees that connect the source and receiver. The two ray paths have a maximal vertical separation of 40 m. The second ray path does not intersect the receiver, however, this ray path is connected to the energy that ensonifies the receiver.

A ray and PE simulation of the acoustic reception at 1.8 km range in the vicinity of the receiver, see Fig. 2.2c, demonstrates two interesting effects in the acoustic propagation. There is a triplication along the ray arrivals at 1.8 km range between 105 and 115 m depth where the direction of the ray depth with respect to launch angle reverses once at 105 m and then again at 115 m. The second arrival recorded on the receiver is in the geometric shadow zone of the ray arrivals, however, the PE model demonstrates that energy from the ray triplication extends into the shadow zone. The PE model can replicate the phase distribution of the first and second arrival observed over the array of hydrophones with fairly consistent agreement, see Fig. 2.2d,e. The phase of the second arrival over the array changes at a constant rate suggesting that it acts like a plane wave.

The extension of sound energy into the shadow zone near triplications and caustics is well-known theoretically in the literature [45]. The alignment of the ray triplication branch and the PE branch, yellow dash-dot line in Fig. 2.2c, suggests that the energy near the triplication is diffracted into the shadow zone. We assume that the ray nearest to the bottom caustic, marked with a star, can be used to calculate the phase perturbations of the second observed arrival. The ray paths shown in Fig. 2.2b are used to calculate the change in phase of both arrivals from the change in sound speed over each ray path.

The change in time travel over each ray path is calculated using the thermistor chain sound-speed profiles and is described by Equation 2.1[33]. The travel time,

$$\tau(t) = \int_{\Gamma} S(\Gamma(z), t) ds, \tag{2.1}$$

is the integral of the slowness, $S(t) = 1/c(t)$, over the ray path, Γ. In our model, the sound speed, $c(t)$, varies in time, t, but not range.

Over the 30-minute transmission, the sound speed in the vicinity of the ray paths decreases due to the upward heaving of the water column from internal waves, see Fig. 2.3a. However, the decrease in sound speed over each ray path is not uniform. The upper ray path experiences a larger decrease in sound speed than the lower path. The heave of the internal waves illustrated with isotachs, black lines in Fig. 2.3a, is vertically correlated. The vertical standard deviation of isotach depth is also fairly uniform, see Fig. 2.3b. In contrast, the vertical standard deviation in sound speed is not uniform in depth due to the change in sound-speed vertical derivative between 100-130 m. The change in sound-speed vertical derivative over depth decorrelates the travel time/phase of these two paths, see Fig. 2.3c. The sound-speed observations indicate that the decorrelation between ray paths happens on a smaller vertical scale than the vertical decorrelation scale of internal wave displacement. In other words, the scale of the changing sound-speed vertical derivative determines the time scale for the change in acoustic phase rather than the modal structure of internal waves.

The changing source-receiver range and depth also contribute to the phase difference by changing the length of the ray path. We assume that the changes in the source and receiver position are small compared to the local curvature of the ray path and make a plane-wave approximation. The approximate phase change is proportional to the angular frequency, ω, the local sound speed, c, and the sine or cosine of the local ray angle, θ, at the source or receiver. The change in phase from depth perturbations is proportional to the sine of the local ray angle, in contrast, the change in phase from range perturbations is proportional to the cosine of the local ray angle [21].

To get the difference in phase, $\delta\phi = \phi_2 - \phi_1$, we subtract the phase perturbations of the

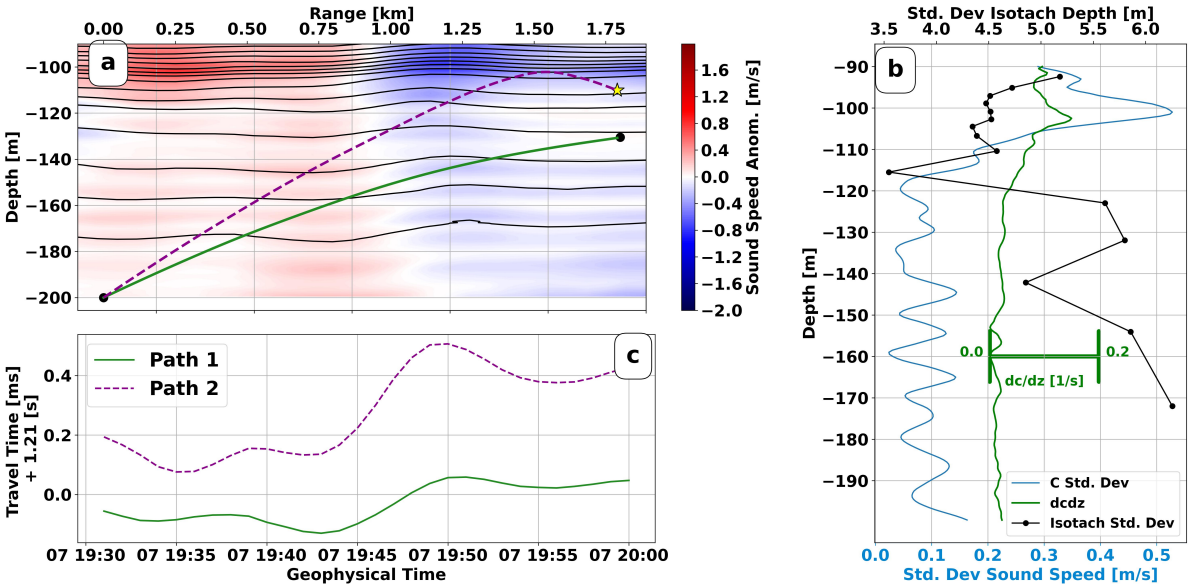

Figure 2.3. (a) Sound-speed anomaly (color) between 90-200 m depth with contours of constant sound speed (black lines). The ray path 1 (green line) and ray path 2 (magenta-dashed line) are drawn over the sound-speed anomaly. (b) The temporal standard deviation of sound speed (blue line), isotach depth (black line), and average sound-speed vertical derivative (green line) between 90-200 m depth. (c) The travel time estimates of ray paths 1 and 2 over the 30-minute interval.

two ray paths,

$$\delta\phi = -\left(\frac{\omega}{c}\right)\left[\delta Z_{src}\left[sin(\theta_2(r_{src})) - sin(\theta_1(r_{src}))\right] + \delta Z_{rcv}\left[sin(\theta_2(r_{rcv})) - sin(\theta_1(r_{rcv}))\right]\right] \tag{2.2}$$
$$+\left(\frac{\omega}{c}\right)\left[-\delta X_{src}\left[cos(\theta_2(r_{src})) - cos(\theta_1(r_{src}))\right] + \delta X_{rcv}\left[cos(\theta_2(r_{rcv})) - cos(\theta_1(r_{rcv}))\right]\right],$$

where θ_1 is the angle of the first ray path and θ_2 is the angle of the second ray path evaluated at the source position, r_{src}, or receiver position, r_{rcv}. The launch angles $\theta_1(r_{src})$, $\theta_2(r_{src})$ are estimated to be 3.3 and 5.5 degrees using the ray traces from Fig. 2.2. The arrival angles $\theta_1(r_{rcv})$, $\theta_2(r_{rcv})$ are calculated to be 1.0 and -6.1 degrees using the vertical phase rate of each arrival along the array from the first reception in the time series. These angles are plugged into Eq. 2.2

to get Eq. 2.3,

$$\delta\phi = -\left(\frac{\omega}{c}\right)\left[\delta Z_{src}\cdot\left[0.038\right] + \delta Z_{rcv}\cdot\left[-0.124\right] - \delta X_{rcv}\cdot\left[-0.006\right] + \delta X_{src}\cdot\left[-0.003\right]\right], \tag{2.3}$$

which explicitly shows the factors multiplying the perturbations. The closeness in the ray angles at both the source and receiver reduces the contribution of range/depth perturbations to the phase difference. The factor multiplying the range perturbations, δX_{src} and δX_{rcv}, is an order of magnitude smaller than the depth perturbations, δZ_{src} and δZ_{rcv}, because the ray angles at the source and receiver are shallow. Ultimately, taking the difference in arrival phase reduces the sensitivity to range perturbations by two orders of magnitude.

2.4 Model-Observation Comparison

The phase difference perturbations from the changing sound speed, range, and depth are summed to estimate the total phase difference. The estimated phase difference is compared to the observed phase difference in Fig. 2.4a. Since we are interested in the time evolution of the phase difference, the time mean of the phase difference is subtracted from the observed and estimated differences. The observed change in phase difference roughly matches the predicted change in phase difference over the 30-minute interval. The summed components that make up the estimated phase difference are shown individually in Figs 2.4b,c.

The internal-wave-driven change in sound speed, red line Fig. 2.4b, contributes the most to the increase in phase difference. The phase difference varies by a root-mean-square of $\pm$4.5 radians, or when converted into a travel time difference $\pm 180\mu$s over the transmission interval. The internal waves account for the change in the phase difference between minutes 5 and 17 of around 1 cycle over 12 minutes. The root-mean-square is provided to give an idea of the variation of these signals and is not an indication of their statistical distribution.

The second strongest component contributing to the change in phase is the decreasing

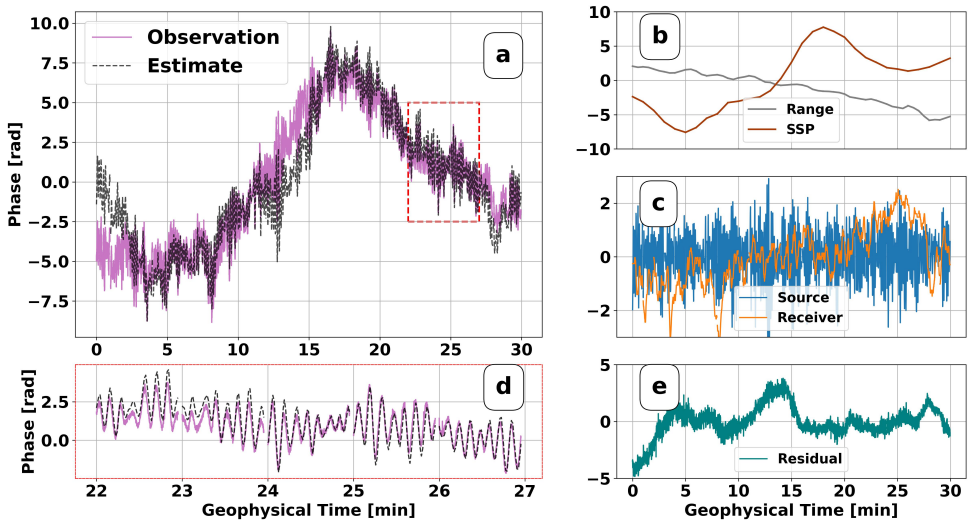

Figure 2.4. (a) Observed (black-dashed line) and estimated (purple line) phase difference between arrivals over 30 minutes. (b) Estimated phase difference from the change in range (grey line) and sound speed (red line). (c) Estimated phase difference from the change in the source (blue line) and receiver (orange line) depth. (d) A five-minute segment of estimated and observed phase difference (red-dashed box) is enlarged to show the oscillating phase difference from source depth perturbations. (e) The residual between observed and estimated phase difference over 30 minutes.

range, see the grey line in Fig. 2.4b, which varies by ± 2.3 radians, $\pm 90\mu$s. The depth perturbations, blue and orange lines in Fig. 2.4c, vary by ± 0.9 radians, $\pm 34\mu$s for the source and ± 1.1 radians, $\pm 42\mu$s for the receiver. The range change, in meters, is an order of magnitude larger than the depth change. The range is the dominant perturbation contributing to the phase of each arrival, however, the phase difference roughly equalizes, to an order of magnitude, the size of the range, sound speed, and depth phase difference perturbations.

In spite of their similar sizes, the distinct time scales of the depth, range, and sound speed perturbations help to identify the different signals contributing to the total phase difference. The signature of the source depth vertical motion on the phase difference is focused on in Fig. 2.4d. The high amount of coherence between the source depth and phase difference gives us confidence that our plane wave approximation is appropriate for the perturbations related to the changing location of the source and receiver. Overall the estimated phase difference is correlated with the

observed phase difference with a R^2 value of 88 percent. The residual difference between the predicted and observed phase difference is shown in Fig. 2.4e.

2.5 Discussion

At short ranges, the multiple propagation paths created from fine structure in the sound-speed profile allow for a phase difference measurement that is sensitive to small vertical changes in the sound-speed profile and source/receiver depth. These propagation paths illustrate the idea that complexity in the medium can increase the information gain in a system. The phase difference in our experiment was primarily driven by the advection of fine structure by internal waves. Importantly the difference in the sound-speed changes between the two ray paths is dominated by the different vertical sound-speed derivatives rather than the vertical modal structures of the internal wave displacements.

Although the ray model of propagation is not as complete as the PE or other propagation models, the ray model makes for a good approximation since the two receptions display ray-like behavior. The ray-based phase estimate captures most of the change in phase difference from the sound-speed profile and perturbations from the moving source/receiver. The ray model does not account for the diffractive part of the second propagation path which may contribute to the minute-scale variability in the residual. This variability could also be due to errors in the measured sound-speed profile. The second-scale residual variability is likely related to our assumption that the ray angles at the source and receiver are constant even though these angles change slightly due to the changing sound-speed environment.

The phase and amplitude fluctuations of mid-frequency acoustic receptions are often handled statistically due to the complications of the medium. These sequential observations of phase between two mid-frequency receptions show that the propagation can be handled deterministically at short ranges and with a well-resolved model of the medium. Even though this is not practical for all cases, these observations suggest that the temporal evolution of

micro-multipath arrivals can be understood by accurately modeling the fine structure in the sound speed environment. Conversely, the micro-multipath arrivals provide information that resolves small-granular vertical differences in the sound-speed profile paving the way for inversion of the fine structure.

ACKNOWLEDGEMENTS

Chapter 2, in part, has been submitted for publication of the material as it may appear in Journal Acoustical Society America Express Letters, 2024. Author list: DeFilippis, Jacob; Cornuelle, Bruce; Lucas, Drew; Hodgkiss William; Kuperman, William. The dissertation author was the primary investigator and author of this paper.

Chapter 3

Chapter 3: The influence of ocean upper ocean fine structure on sound speed fluctuations driven by internal waves.

3.1 Introduction

Acoustic fluctuation studies have largely focused on internal waves [43, 15, 41, 49, 10, 13] and to a lesser degree spice [12, 6, 42]. While there have been past efforts to address fine structure [19, 15, 30], this paper investigates the non-linear advection of fine structure by internal waves, particularly, how this process can change the temporal variability of ocean sound speed perturbations. High-resolution upper ocean observations of internal waves, spice, and fine structure, see Section 3.3, help quantify the temporal variability and implications for upper ocean acoustic propagation.

Sound speed fluctuations in the upper ocean are dominated by fluctuations of temperature and salinity. The vertical structure of these quantities has fine scales due to various oceanographic processes such as salt fingers, intrusions, or remnant mixed layers [35, 44]. The advection of fine structures by internal waves has been studied in the oceanographic literature. Notably, authors have looked at how the spectrum of passive tracers measured at fixed depths are whitened by the advection of vertical fine structures [1, 38]. Acoustic wave propagation through a time-varying internal wave field involves similar effects since sound propagates in an Eulerian coordinate

system. Section 3.3.2 and 3.4 explore the degree to which the fine structure creates sound speed perturbations at frequencies above the buoyancy frequency, the cut-off frequency for internal waves.

The change in the vertical sound-speed gradient plays an important role in altering the spectrum of internal-wave-induced sound speed perturbations through non-linear processes. The size of the internal wave displacements compared to the vertical scale of sound-speed gradients determines the strength of the nonlinearity. In Section 3.2, we derive a non-dimensional number N_F to quantify the local curvature of the sound speed compared to the vertical displacement from internal waves. Observed sound-speed profiles are advected with isopycnal displacements generated from an internal wave model, see Section 3.3.2. Internal waves cannot have frequencies higher than the buoyancy frequency of the surrounding water mass, hence, internal waves have a natural cut-off frequency, ω_c determined by the maximum buoyancy frequency of the stratification profile. However, we find that the sound speed variability extends past the maximum buoyancy frequency and is correlated with this non-dimensional number. The spectrum of sound speed perturbations and its time derivative have important implications for acoustic random medium effects and signal processing because the acoustic coherence is related to the phase fluctuation rate. The phase rate is driven by the temporal and spatial statistics of the time rate of change sound speed field, which is calculated in both Sections 3.3 and 3.4.

3.2 Theory

Consider a sound-speed profile $c(z)$ perturbed by vertical displacements, $\zeta(z)$ due to internal waves. The coordinate system is such that z increases positively towards the surface. A parcel of seawater with sound speed, $c(z_0,t_0)$, at depth z_0 is displaced adiabatically a distance $\zeta(z_0,t_0)$ at time t_0. The change in sound speed at depth $z' = z_0 + \zeta(z_0,t_0)$ and time t',

$$\delta c(z',t') = c(z',t_0) - [c(z_0,t_0) + \gamma\zeta(z_0,t_0)] \quad , \tag{3.1}$$

is described by the nonlinear equation, Eq. 3.1. The last term accounts for the adiabatic change in the parcel's sound speed as it moves to a z to z' depth. The adiabatic change is linearized to first order where the adiabatic gradient is $\gamma \simeq 0.016$ (1/s). The non-linear first term in Eq. 3.1 can Taylor expanded to higher order,

$$c(z',t') = c(z_0,t_0) + \frac{dc}{dz}\zeta(z_0,t_0) + \frac{d^2c}{dz^2}\frac{\zeta^2(z_0,t_0)}{2} - O(\zeta^3). \tag{3.2}$$

Then this expansion is substituted back into Eq. 3.1,

$$\delta c(z',t') = \left(\frac{dc}{dz}\right)_p \zeta(z_0,t_0) + \frac{d^2c}{dz^2}\frac{\zeta^2(z_0,t_0)}{2} + O(\zeta^3). \tag{3.3}$$

Most sound speed perturbation calculations only use the first-order term where

$$(dc/dz)_p = (dc/dz) - \gamma \tag{3.4}$$

is the potential sound-speed gradient. Linearization of the problem eases the calculation of sound speed perturbations, however, the higher-order terms contribute significantly to the sound speed perturbation when the higher-order derivatives are non-negligible especially when the displacement is large. For example, consider an idealized sound speed structure,

$$\Delta C(z) = \delta c_0 \tanh\left(\frac{(z-z_0)}{Z}\right) \quad , \tag{3.5}$$

to a linear sound-speed profile. A tanh function centered around z_0 and parameterized with a vertical scale, Z, and amplitude δc_0 represents the step-like feature of upper-ocean fine structure. The idealized perturbation demonstrates the case where the error in the approximation can be large, see Fig. 3.1.

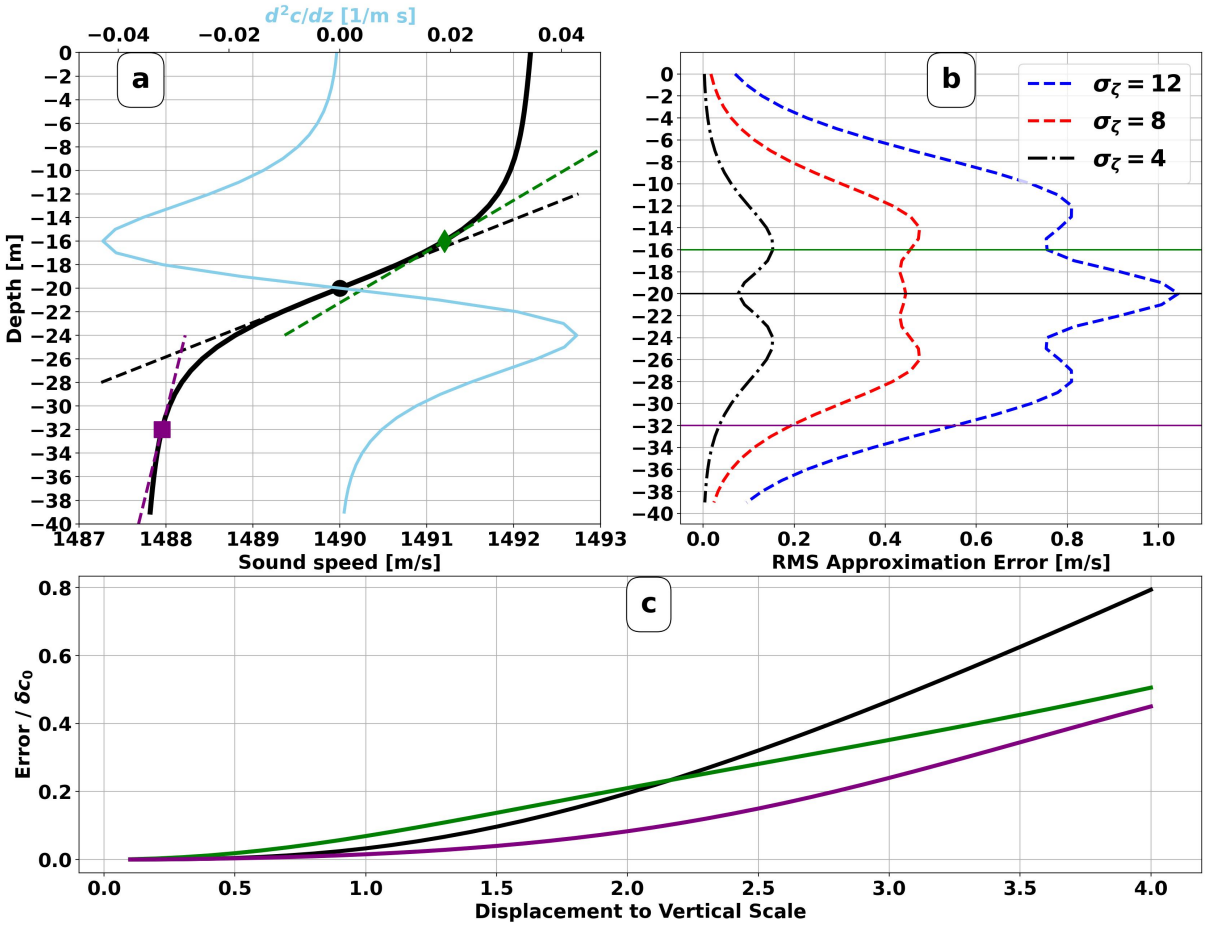

Figure 3.1. (a) An idealized sound-speed fine structure described by Eq. 3.5 (black line) with a vertical scale $Z = 8m$. Tangent lines (green, black, and purple dashed lines) are drawn at three center points along the curve. The second derivative of sound speed is shown with the light-blue curve. The center points on the curve are chosen to be at an extremum of the second derivative (green), below the maximum of the second derivative (purple), and at the zero-point of the second derivative (black). (b) The root-mean-square error for the tangent approximation at every point in the sound-speed profile for the maximum displacement of $\pm$4m (black), $\pm$8m (red), and $\pm$12m (blue). (c) The depth-average root-mean-square error of the tangent approximation as a function of varying maximum displacement for the three center points (green, black, purple) in (a).

The linearization of the curve in Fig. 3.1a is represented by the tangent lines (dashed lines) at three center points along the curve. The horizontal distance between the tangent line and the tanh curve is the error in sound speed. the tanh The vertical distance of each tangent line, the displacement, is twice as large as the vertical scale, Z. The error of the linear approximation as a function of the center point, see Fig. 3.1b, is related to the magnitude of the second derivative

shown in Fig. 3.1a (light blue curve). The error is cumulative over the scale of the displacement.

The ratio of the vertical scale of the sound speed perturbation to the displacement scale determines the strength of the non-linearity which is represented by the error made by the linear approximation. The error grows as the displacement scale grows, see Fig. 3.1b,c. When the displacement scale is small, center points near the maximum absolute value of the second derivative have maximum error (Fig. 3.1b black curve). However, when the displacement scale is larger than the vertical scale of the sound speed structure, the error at the inflection point (black dot) grows the fastest because the displacement spans over both maxima in the second derivative, see Fig. 3.1c (black line).

An important factor for signal processing is the time rate of change of sound speed perturbations, $\delta\dot{c}$. This quantity is relevant for calculating the acoustic coherence and phase rate. Taking the time derivative of Eq. 3.3 to second order gives,

$$\delta\dot{c}(z',t') = -w(z_0,t_0)\left[\left(\frac{dc}{dz}\right)_p + \zeta(z_0,t_0)\frac{d^2c}{dz^2}\right] \quad , \tag{3.6}$$

where $w(z,t)$ is the internal wave vertical velocity. The second-order quadratic terms in Eqs. 3.3 and 3.6 generate second harmonics that contribute to fine structure time scales. Consider the case of a single frequency sinusoidal displacement over time, $\zeta = \zeta_0 \sin(\omega t)$ and $w = \omega\zeta_0 \cos(\omega t)$. Substituting this form of displacement into Eq. 3.6,

$$\delta\dot{c}(z',t') = -\omega\zeta_0\left(\frac{dc}{dz}\right)_p \cos(\omega t_0) - \frac{\omega\zeta_0^2}{2}\frac{d^2c}{dz^2}\sin(2\omega t_0). \tag{3.7}$$

and the second harmonic is clear from the second term in Eq. 3.7. The higher-order terms in the expansion generate even higher harmonics further spreading the spectrum of sound speed variability. The amplitude of each of these terms is proportional to the n^{th} vertical derivative. We will assume that the second-order term in the Taylor expansion is larger than the rest of the higher-order terms and focus on the second harmonic. A natural non-dimensional number to

measure the fine structure can then be defined by the ratio of the second term to the first term in Eq. 3.3 namely,

$$N_F = \frac{\zeta_0}{2} \frac{d^2c/dz^2}{(dc/dz)_p}. \tag{3.8}$$

When $N_F > 1$ fine structure effects will be significant. If the spectrum of $\dot{c}$ is considered the ratio of the second harmonic energy over the first harmonic will be $2N_F^2$. This paper normally will report the base-10 logarithm of the fine-structure number.

3.3 Observations

Internal waves change the depth of surfaces with constant density, isopycnals, in the ocean. In doing so the potential temperature and salinity move with these isopycnals giving rise to sound speed changes. The change in sound speed is related to both the change in sound speed between isopycnal surfaces as well as the motion induced by internal waves. The sound speed can also change along isopycnal surfaces, commonly referred to as spice. Both internal-wave- and spice- related sound speed variability was observed in a series of salinity, temperature, and pressure profiles measured 400 miles off the coast of Southern California in deep water on the R/V Sally Ride on 9 November 2020, see Fig. 3.2.

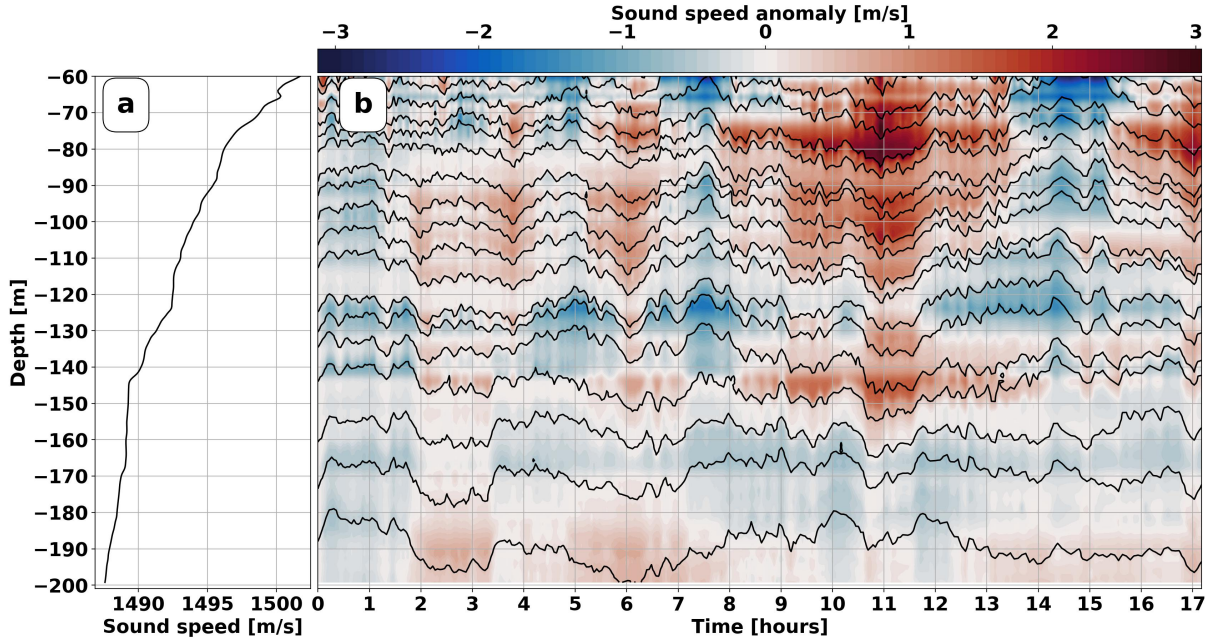

Figure 3.2. Observations of sound-speed anomaly with respect to the first profile and density calculated from a 17-hour series of FastCTD profiles sampled every 3 minutes. (a) Sound-speed profile measured 2:00 9 Nov. 2020 UTC (black line) between 60-200 m depth. (b) The temporal sound-speed anomaly (color) at each depth between 60-200 m. Contours of constant density (black lines) from 1024.26-1026.35 σ_θ at 0.1 spacing are overlaid on top of the sound-speed anomaly The action of the internal waves changes the depth of these constant-density surfaces over time which changes the measured sound speed at each depth.

The water column was measured down to 200 m for 17 hours from 2:00-19:00 UTC on 9 Nov. 2020 with the FastCTD – a rapid profiling system – while the ship was stationary. Each 200 m round-trip profile is sampled roughly every three minutes, with a vertical transit rate of $\sim$ 2.5 m/s. Temperature, conductivity, and pressure were sampled at 16 Hz. Sound speed and density were calculated from the equation of state[32] using the salinity and temperature binned to a vertical grid with 0.25 dbar resolution. The oscillating isopycnals, black contours in Fig. 3.2, demonstrate the action of the internal waves over time. Fig. 3.2 also shows that the sound speed anomaly is positive (red) when isopycnals move downwards and the sound speed anomaly is negative (blue) when isopycnals move upwards. The spice variability being weaker than the internal wave sound speed variability is not obvious from Fig. 3.2.

To deconstruct the sound-speed field into internal wave and spice variability, the sound

speed and depth are mapped onto a uniform grid in density coordinates. A set of densities, σ_j, with equal 0.005 σ_θ density spacing between 1024.26-1026.35 σ_θ are selected using the first CTD profile to make a uniform density grid. The potential sound speed and depth of those densities are calculated for each profile in the series. This is done by interpolating the potential sound speed and depth as a function of density, $C_p(\sigma_\theta)$ and $Z(\sigma_\theta)$ for each profile and then evaluating those interpolations onto a uniform-density grid, $C_p(\sigma_j), \quad Z(\sigma_j)$.

The spice variability is directly calculated from the change in potential sound speed on each isopycnal. The internal wave variability is calculated from the isopycnal displacement. The displacement, ζ, is referenced to the time-mean depth of each isopycnal, $\overline{Z(\sigma_j)}$. The isopycnal displacement and spice are mapped back into depth coordinates by interpolating the spice, $C_s(\sigma_j)$, and displacement, $\zeta(\sigma_j)$, to the mean isopycnal depth, $\overline{Z(\sigma_j)}$, and then the interpolation function is evaluated onto a uniform depth grid between 60-200 m depth with 0.5 m spacing.

The internal wave displacement is interpolated along the time dimension for a uniform one-minute time sampling. The one-minute time sampling is needed to investigate sound-speed variability at frequencies past the maximum buoyancy frequency discussed in Section 3.3.2. The interpolation is done by fitting a harmonic model of sines and cosines to the displacements at each depth. The internal wave displacement of isopycnals cannot have frequencies greater than the maximum buoyancy frequency ≈ 6 cph, and so the roughly three 3-minute time sampling of the FastCTD, 20 cph, is sufficient to capture the variability of displacement. The harmonic model has discretized frequencies from $1/17$ to 6 cph at $1/17$ cph intervals. The interpolation of displacement is shown at two depths in Figs. 3.3 b,f.

3.3.1 Sound Speed Model

We calculated the change in sound speed by simulating the displacement of the first sound speed profile over time with the interpolated grid of isopycnal displacements using a non-linear vertical advection scheme (NLVA) following Equation 3.1. This algorithm is discussed further in Appendix B. The modeled sound speed anomalies isolate the variability from internal waves.

The displacement and sound-speed anomaly at two fixed depths shown in Figs. 3.3b,c,e,f use this scheme.

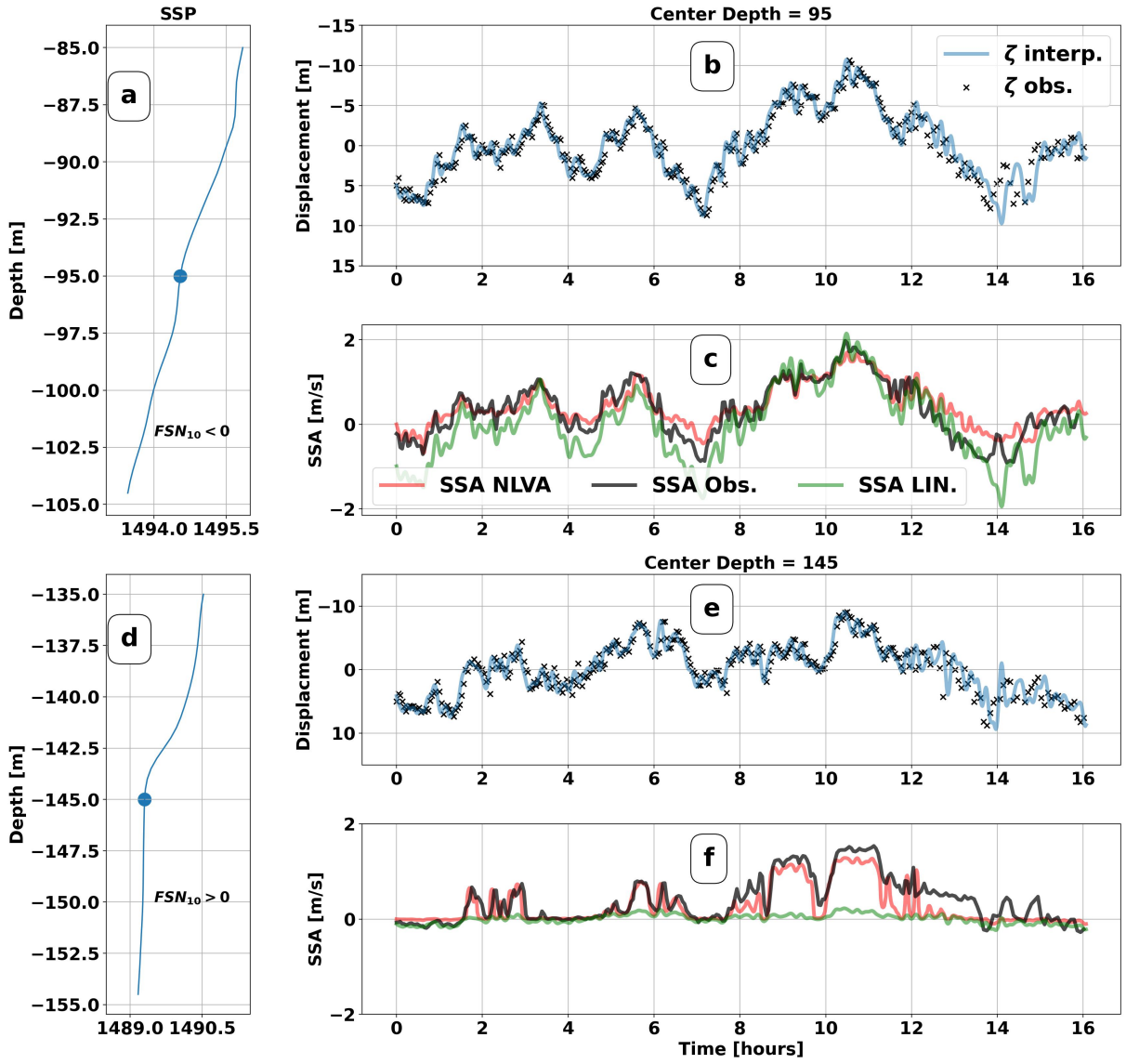

Figure 3.3. (a) The sound-speed profile between 85-105 m depth, which has a low fine-structure number and (d) the sound-speed profile between 135-155m which has a high fine-structure number. (b),(e) The measured change in isopycnal depth (black 'x' marks) and the temporal interpolation (blue line) to those measurements at 90 m and 145 m depth. (c),(f) The linear (green line) and non-linear (red line) models of sound-speed anomaly are compared to the measured sound-speed anomaly (black line) over 16 hours at 90 m and 145 m depth.

The time series of modeled SSA, red and green lines in 3.3c,f, is driven by the time series of isopycnal displacement, blue lines 3.3b,e. SSA anomaly is normally negatively correlated with

displacements because in the upper ocean sound speed increases towards the surface. The match between the linear model and the observations, see Fig. 3.3c,f, depends on the local curvature of the sound-speed profile represented by the fine structure number, see Fig. 3.3a,d.

A salient feature of the non-linear relationship between SSA and displacement is demonstrated in Fig. 3.3d,e,f. The sound-speed profile centered at 145 m depth has a gradient that changes from near-zero at below 145 m to 0.15 $sec^{-}1$ above 145 m. When the profile is displaced downwards, the change in sound speed is positive and proportional to the gradient above 145 m. When the profile is displaced upwards the change in sound speed is proportional to the gradient below 145 m so there is nearly zero change in sound speed. This effect creates a square-wave-like signal to the sound-speed anomaly. The linear model, which uses the local gradient in sound speed, fails to produce this signal.

Differences between the observed SSA and the SSA NLVA in Figs. 3.3c,f are attributed to the spice anomaly in the observations. This difference is most apparent in Fig. 3.3f between hours 12 and 14, where the observed displacement and sound speed anomaly are both positive – these two factors are supposed to be inversely proportional. The increase in sound speed therefore must have come from the horizontal advection of seawater with a higher sound speed but equal density.

The linear and non-linear models of SSA are compared to the observations for all depths, see Figs. 3.4a,b,c. The non-linear model reduces the difference between observation and model, the residual, by half compared to the linear model, see Fig. 3.4d. The effect of the fine structure is illustrated by the residual between the linear model and observations, Fig 3.4a. This residual contains stronger and more frequent variability than that of the residual between the observations and the non-linear model, see Fig. 3.4b.

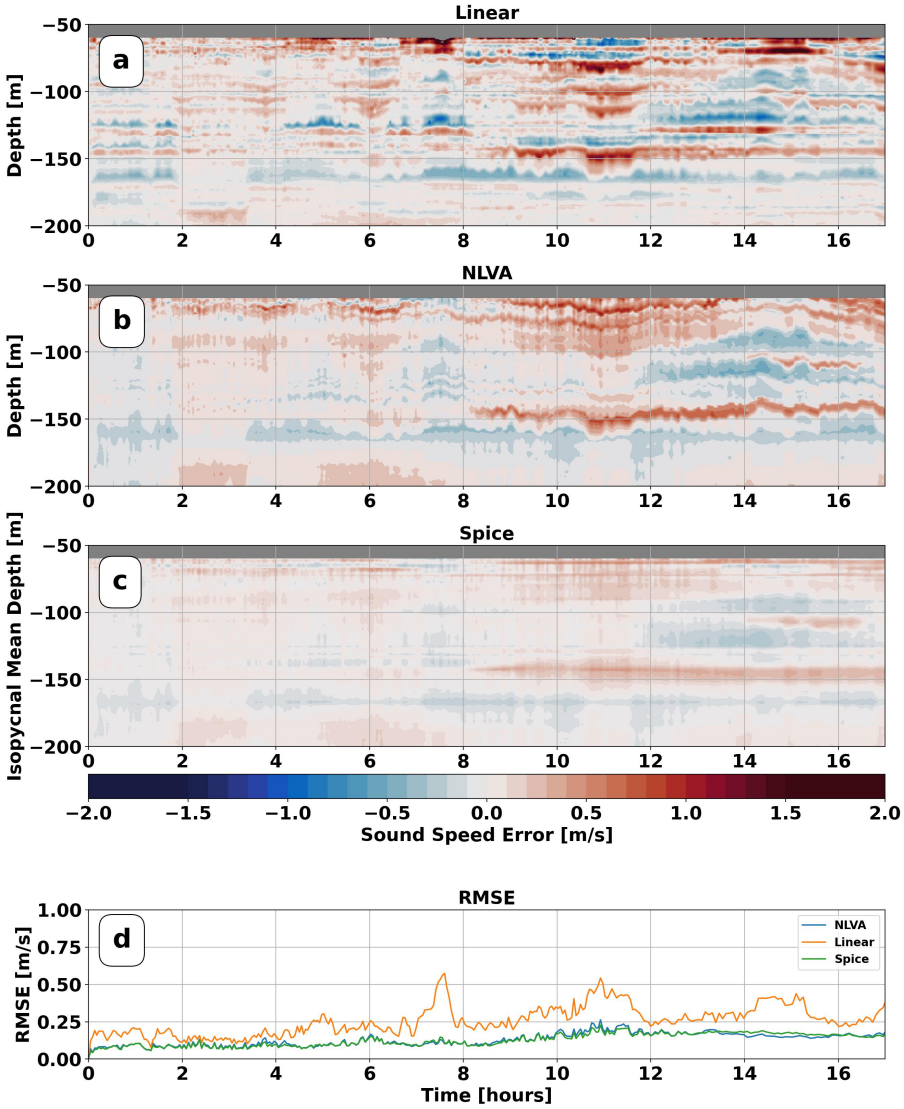

Figure 3.4. (a) The difference between the linear approximation of SSA using observed isopycnal displacement and observed SSA over 17 hours between 60-200 m depth. The sound-speed anomaly is calculated with respect to the first profile in the time series. (b) The error between the non-linear prediction and observed sound-speed anomaly using measured isopycnal displacement over 17 hours between 60-200 m depth. (c) The on-isopycnal sound-speed anomaly (spice) over 17 hours plotted at the mean depth of the isopycnal. (d) The depth-average error of the linear and non-linear model and the depth-average sound-speed anomaly from spice.

The horizontal spice variability is converted into a temporal variability as patches of spice pass by the ship's profiler. The on-isopycnal SSA variability (spice), see Fig 3.4c, is an order of magnitude smaller than the total sound-speed anomaly. Since the internal wave and

spice sound-speed anomalies make up the total sound-speed anomaly when the internal wave variability is subtracted from the observations the spice sound-speed anomaly is left over. This is why the NLVA residual and spice sound-speed anomaly roughly match up, however, the spice variability in Fig. 3.4c is plotted in isopycnal coordinates, so the action of the internal waves is removed.

3.3.2 Temporal Scales

The spectra of interpolated isopycnal displacements and NLVA SSA are estimated using a Welch Method with 3-hour window lengths. The power spectra are normalized by dividing by the total power of each spectrum so the y-axis of Fig. 3.5 shows the fractional power with unit variance. As previously discussed in Section 3.3 the NLVA SSA does not contain spiciness hence isolating the effect of the fine structure and internal waves. We hypothesize that the spectra of SSA should extend past the cut-off frequency due to the non-linear advection of fine structure. The internal wave cut-off frequency in Fig. 3.5 is set to $\omega_c = 6$ cph by the harmonic model interpolation of displacement.

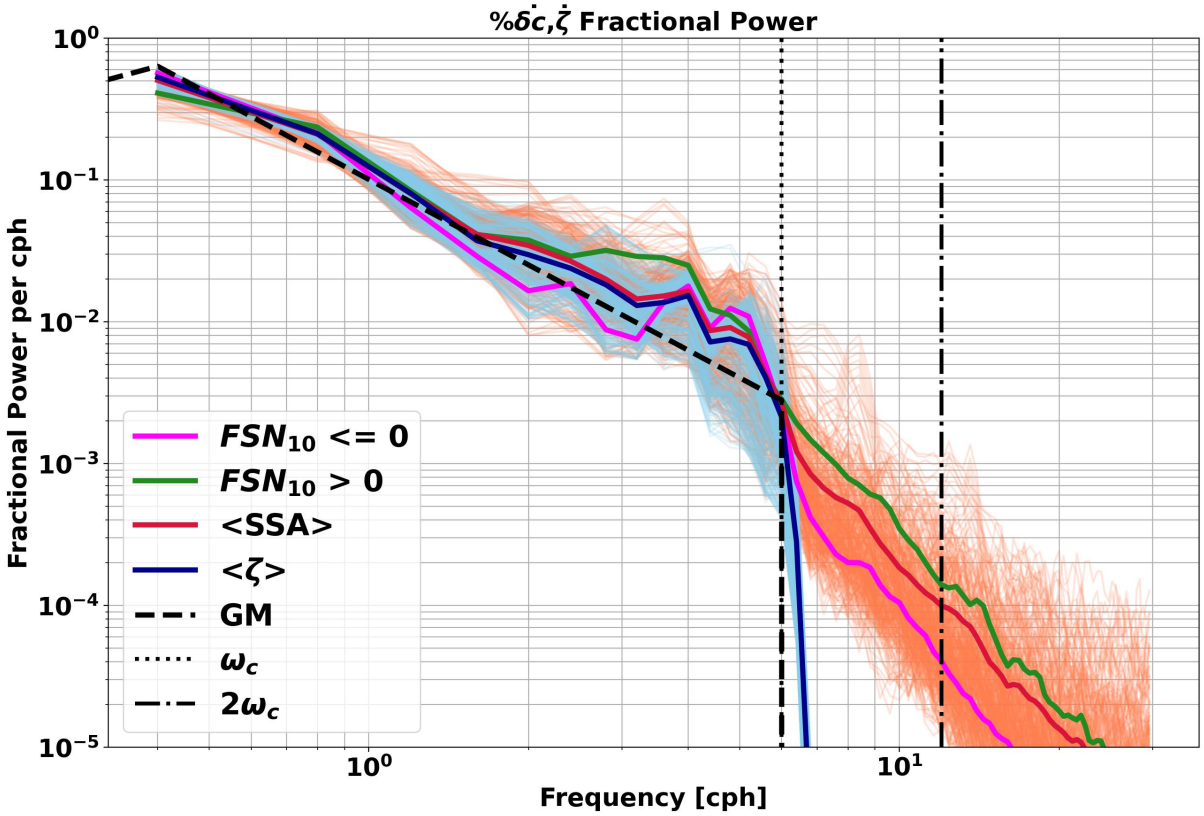

Figure 3.5. Spectra of isopycnal displacement (light blue lines) and sound-speed anomaly (orange lines) calculated over 17 hours at 0.5 m depth intervals between depths of 60-200 m. Each spectrum is normalized by its total power to compare displacement and sound speed on the same plot. The black-dashed line shows the normalized Garrett and Munk spectrum (black-dashed line) for internal wave isopycnal displacement. The depth-mean of the displacement and SSA spectra are shown with the dark blue and red lines, respectively. The depth-average SSA spectrum between 140-160 m depth, which generally has a high fine structure number, is shown with a dark green line. The depth-average SSA spectrum between 80-100 m depth, which generally has a low fine structure number, is shown with a magenta line.

The roll-off of power past the cut-off frequency varies with depth and is correlated with the amount of fine structure at each depth. The slope of the normalized depth-averaged power spectra of sound-speed anomaly past ω_c is -4.1. The slope of the depth-averaged sound speed spectrum for frequencies less than ω_c is -1.7 which deviates slightly from ω^{-2} due to the bump in power near ω_c. Both displacement and sound speed have this bump, which is discussed further in Section 3.4.

Depths (140-160 m) that on average have fine structure numbers above zero have an

average spectral slope past the cut-off frequency of -4.0. On the other hand, the depth-average spectral slope past the cut-off frequency at depths between 80-100 m, which on average have low fine structure numbers, is -4.7, which suggests a correlation with power past ω_c and the fine structure number.

The time rate-of-change in sound speed, $\dot{\delta c}$, is a relevant quantity for calculating the phase rate of acoustic fluctuations. The time derivative introduces a factor of ω^2 to the power spectra of sound speed fluctuations. This additional factor makes the Garrett and Munk spectrum white, see black-dashed line Fig. 3.6a. The observational spectra of sound speed and displacement have a bump in power near the cut-off frequency meaning that frequencies right before the cut-off frequency contribute the most to $\dot{\delta c}$.

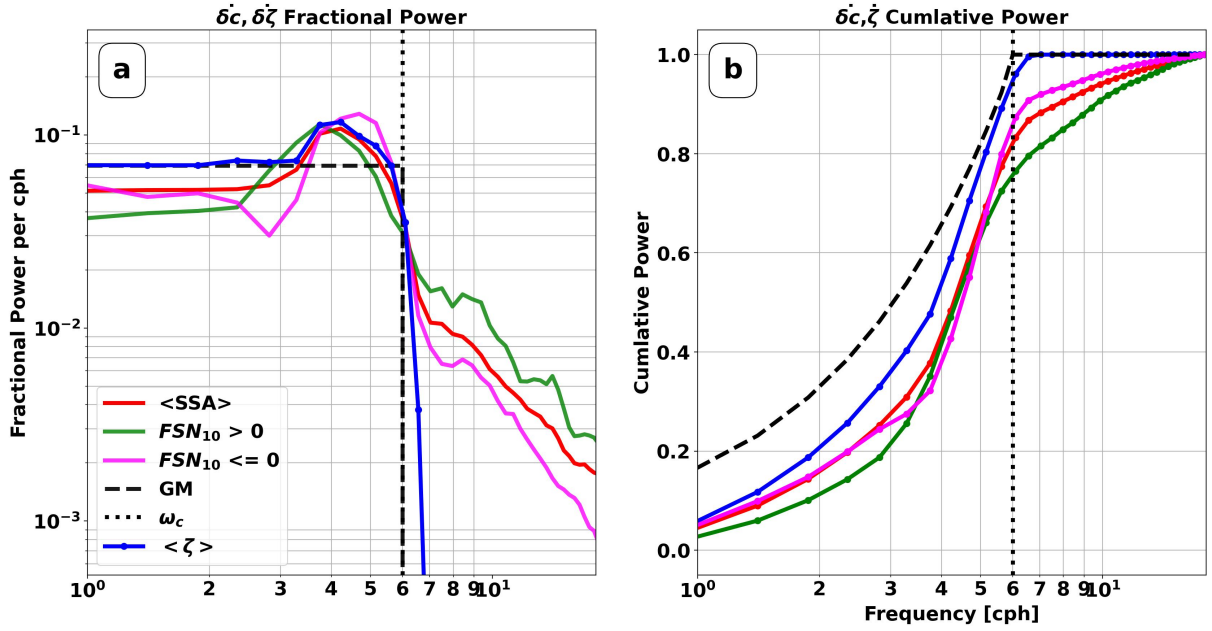

Figure 3.6. (a) Depth-averaged spectra from Fig. 3.5 are whitened by taking the time derivative of the sound-speed anomaly (magenta, red, green lines) and displacement (blue line). (b) The cumulative power of each of those spectra is shown as a function of frequency. The dotted line is the cut-off frequency, ω_c, for internal waves.

The variability of the $\dot{\delta\zeta}$, blue and black line Fig 3.6b, is limited to frequencies less than the cut-off frequency. This means 0% of the variability for a linear model is at frequencies above the cut-off frequency. Whereas the observed depth-averaged power spectra of $\dot{\delta c}$, red line Fig

3.6b, has roughly 20 % of its variability at frequencies above the cut-off frequency. Near depths with low or high fine structure numbers that percentage may be lower or higher, see green and magenta lines Fig. 3.6b.

To find out whether the proposed fine structure number is a predictor for changes in the power spectra, we calculate the ratio of the energy above and below the cut-off frequency. Equation 3.9 defines the ratio of this energy,

$$R_H(z) = \int_{\omega_c}^{\omega_h} S_{\dot{c}}(z,\omega)d\omega / \int_{\omega_0}^{\omega_h} S_{\dot{c}}(z,\omega)d\omega \quad , \tag{3.9}$$

where $S_{\dot{c}}$ is the power spectra of the time rate-of-change in sound speed, ω_0, is the fundamental frequency, ω_c, is the cut-off frequency, and $\omega_h = 2\omega_c$ is the first harmonic of the cut-off frequency. $R_H(z)$ gives a rough estimate of how much the spectrum has whitened and therefore how much the timescales of the underlying signal have changed. R_H should be zero for a linear sound-speed profile when the fine-scale number is zero. R_H should increase with increasing fine structure number.

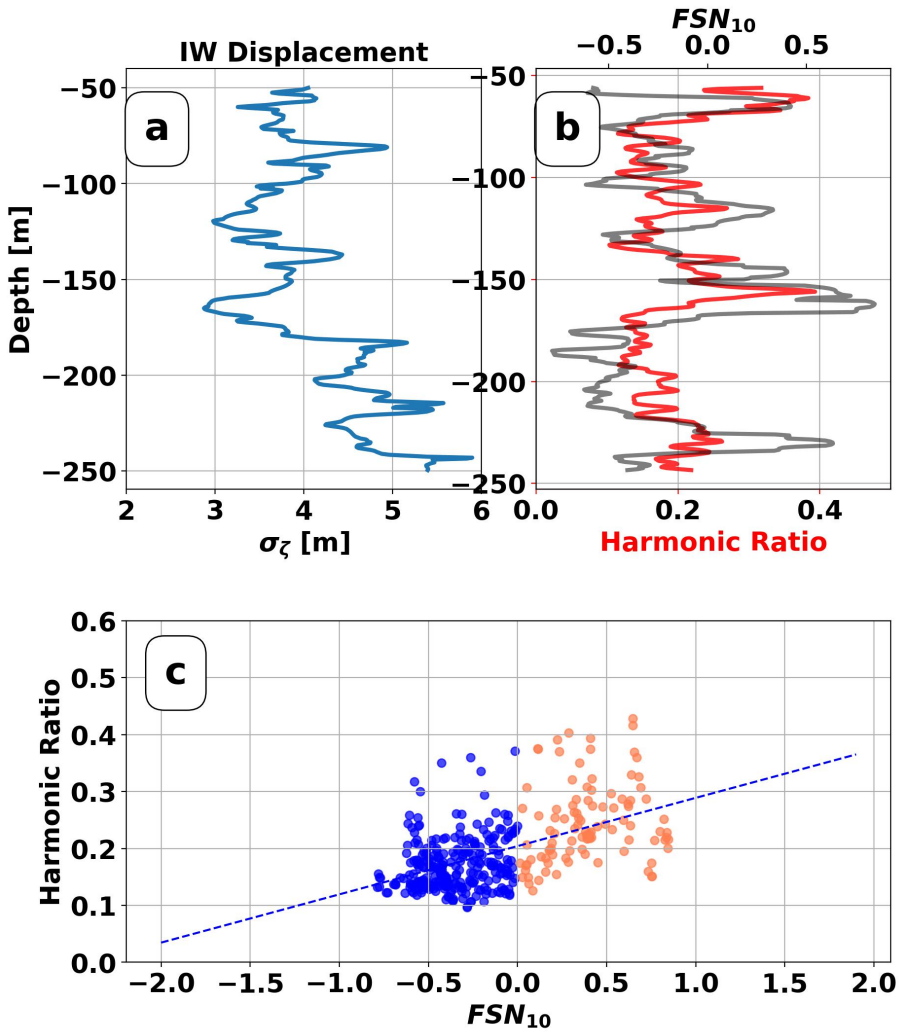

Figure 3.7. (a) The RMS displacement of isopycnal surfaces between 50-250 meters. (b) The harmonic ratio (red line) of sound speed fluctuation spectrum versus depth compared to the base-10 logarithmic fine structure number (black line) of the sound-speed profile. (b) A scatter plot of the harmonic ratio and logarithmic fine structure number. Blue dots are logarithmic fine structure numbers below zero and orange dots are above zero. The blue-dashed line is fit to the points in (b) and has a slope of 0.08 and an R^2 value of 0.52.

We calculated the logarithmic fine structure number and harmonic ratio at each depth from the 17 h FastCTD record, see Fig. 3.7a. The fine-structure number is plotted on a logarithmic scale along the horizontal axis because of the large range of fine-structure numbers. Fig. 3.7 shows harmonic ratio as a function of fine structure number. The harmonic ratio is positively correlated with fine structure numbers, however, for this data set the correlation value is 0.52.

Though the harmonic ratio tends to increase with fine structure numbers there are outlier depths that have a high harmonic ratio, $H_r > 0.3$, for fine structure numbers below zero.

3.4 Internal Wave Model

3.4.1 Linear Depth-Independent Model

Two linear internal wave models are utilized to generate more realizations of the internal-wave-driven isopycnal displacements. The first model produces a two-dimensional field of internal wave displacements which are a sum of plane waves varying solely in time,

$$\zeta(t) = \Re e\left\{\sum_j A_j e^{-i\omega_j t+\phi_j}\right\}, \tag{3.10}$$

where ω_j are the angular frequencies, ϕ_j are the phases, and A_j the amplitudes of each wave. The amplitudes are solely dependent on the frequency. Amplitudes for each wave in the model are derived from Eq. 3.11 from the Garrett and Munk spectrum. The power of each frequency is described by

$$B(\omega) = \frac{2f}{\pi\omega\sqrt{(\omega^2 - f^2)}} \quad , \tag{3.11}$$

where ω is the internal wave frequency, f is the Coriolis frequency. The phase, ϕ_j, of each internal wave is sampled from a uniform distribution from $[0-2\pi]$. In this model, we assume that the buoyancy frequency is uniform in depth thus the internal waves are also depth-independent. This assumption does not hold in the real ocean where the depth-varying stratification causes the displacement to vary with depth. However, keeping the displacement constant in depth allows us to remove any correlations between the depth-varying stratification and the sound speed structure.

Three different profiles are vertically displaced using the NLVA scheme and the field of simulated isopycnal displacements. Each profile represents a different case in terms of the amount of total fine structure between 60-250 m depth. A sampled profile from May 2021,

during TFO2, represents a case of high fine structure. A sampled profile from 9 Nov 2020, during TFO1, represents a case of low fine structure. A 100-member ensemble of 2-day internal wave fields is simulated. The simulated realizations have a half-minute sampling and 0.5 meter vertical sampling.

The power spectra of isopycnal displacement and sound-speed anomaly are estimated using a Welch Method with 23-hour window lengths, see Fig. 3.8. The spectra are depth-averaged, however, the spectra at each depth are divided by their total powers. The slope and shape of the spectrum are more relevant for our study than the total power of each spectrum.

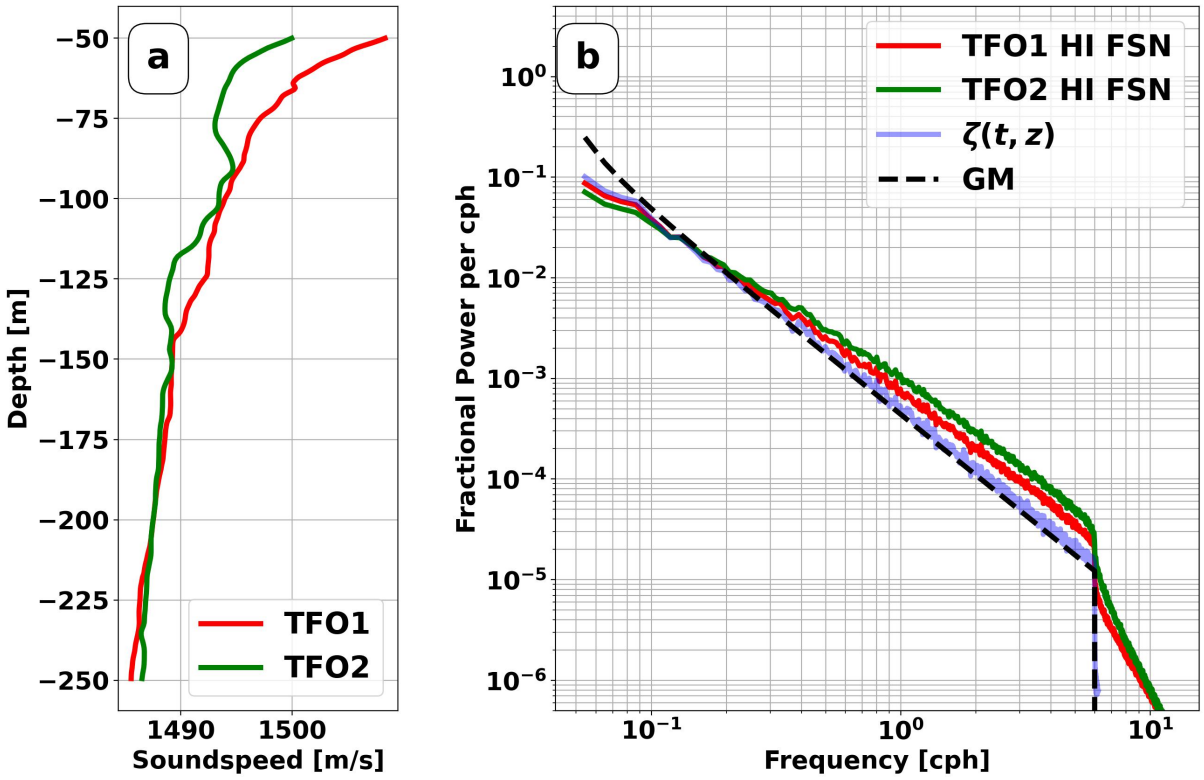

Figure 3.8. (a) Two sound-speed profiles, one sampled during the Fall of 2020 during the TFO1 experiment(red line) and one sampled in Spring 2021 during the TFO2 experiment (green line). (b) The depth-averaged power spectra of sound speed fluctuations are normalized by the total power of the spectra at each depth. The power spectral density at each depth is estimated using Welch's method with a window length of about 23 hours. The power spectrum of isopycnal displacement prescribed by a Garrett and Munk Spectrum is shown with the black-dashed line. The depth-average simulated isopycnal displacement spectrum normalized by the total power is shown with the blue line.

Both sound-speed anomaly spectra have energy leaking past the cut-off frequency due to the whitening of their spectra. The slopes of depth-average spectra of SSA (green and red lines) past ω_c, see Fig. 3.8, are -3.7 and -4.3 respectively, and are -1.8 and -1.9 before ω_c which agrees with the slopes estimated from observations. The time rate-of-change of the sound speed spectra is shown in Fig. 3.9a. The cumulative variance of $\dot{\delta c}$ is computed as a function of frequency in Fig. 3.9b.

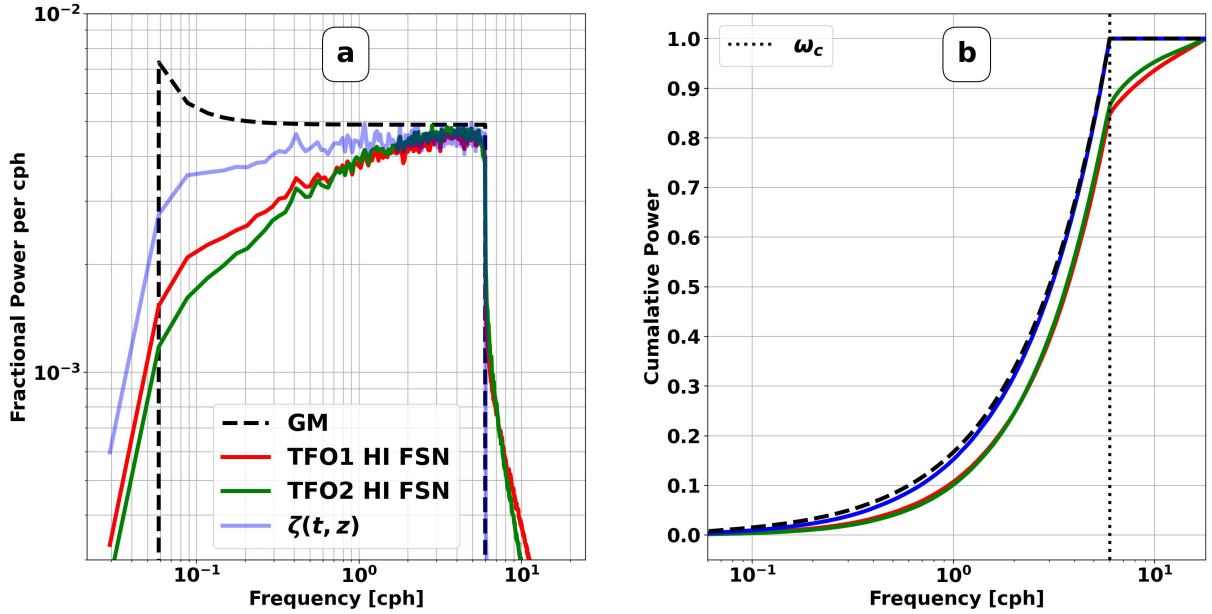

Figure 3.9. (a) Spectra in Fig. 3.8 are whitened by multiplying ω^2 to emphasize the change in slope of the sound-speed anomaly compared to the GM spectrum. (b) The cumulative power of the spectra is shown as a function of frequency. The dot line vertical line is the cut-off frequency for internal waves, ω_c.

The depth-dependent model shows only 10% of the total power at frequencies greater than the cut-off frequency, ω_c, which is lower than the observations. Another difference is that the isopycnal displacement spectrum does not have a bump in energy near ω_c like the observed displacement spectrum. The additional bump in energy is an important factor in calculating the sound speed fluctuation spectrum for frequencies greater than ω_c, and so we investigate fluctuations from a modal internal wave model in the next section.

3.4.2 Modal Model

A second model is used to produce internal wave displacements that are depth-dependent. The solution of the internal wave field is assumed to be separable $\zeta(t,z) = F(t)\Phi(z)$. The solution $F(t)$ is assumed to be a sum of plane waves, the same as the first model. The depth-dependent component is modal due to the top and bottom boundary conditions at the surface and bottom of the ocean where the displacement must be zero. The stratification, $N(z)$, and frequency, ω, determines the modal solutions of Equation 3.12.

$$\frac{d^2\Phi}{dz^2} + k^2 \frac{N^2(z) - \omega^2}{\omega^2 - f^2}\Phi(z) = 0 \tag{3.12}$$

where k is the wavelength and Φ are the modes. Each mode, ϕ_i, is normalized by using the potential energy normalization,

$$\frac{\rho}{2}\int_0^D N^2(z)\phi_i(z)^2 dz = 1 \tag{3.13}$$

described by Eq. 3.13, where ρ is the average density, $N^2(z)$ is the stratifcation profile, and D is the depth range.

Fig 3.10 shows the first three modes for a frequency $1/12$ cph generated from the stratification profile of TFO1. Fig 3.10 shows the first three modes for frequency 4 cph from the same stratification. The solutions are evanescent when the internal wave frequency is higher than the buoyancy frequency, $\omega > N(z)$. As frequency increases the modes become trapped in areas of higher stratification.

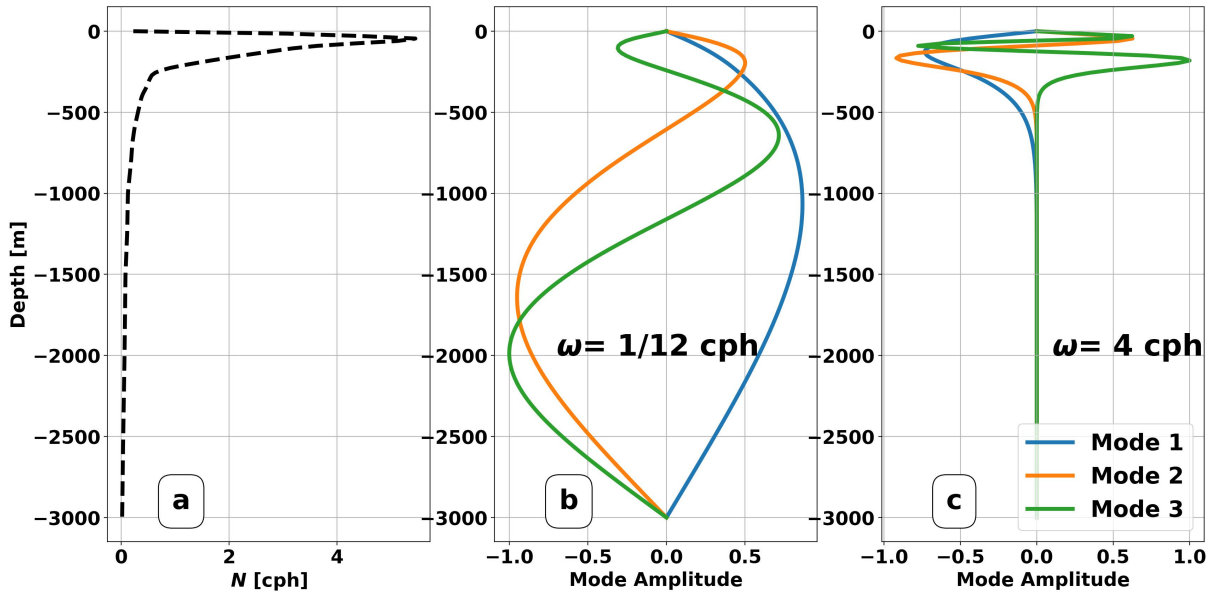

Figure 3.10. (a) A stratification profile, $N(z)$ versus depth (black-dashed line). (b) The first three modes of an internal wave with $\omega = 1/12$ cph. (c) The first three modes of an internal wave with $\omega = 4$ cph.

The modal model contains a set of 144 frequencies from the inertial frequency, $1/24$, cph to the cut-off frequency of the stratification profile, $\omega_c = 6$ cph. Each frequency consists of three modes. The amplitude of each wave is prescribed by the Garrett and Munk spectrum[20] which now varies with both frequency and mode number, described by

$$G(\omega, j) = B(\omega) \cdot H(j) \quad , \tag{3.14}$$

where j is the mode number and ω is the frequency. The modal spectrum

$$H(j) = \frac{N_j}{(j + j^*)} \quad , \quad \frac{1}{N_j} = \sum_1^\infty \frac{1}{(j + j^*)}, \tag{3.15}$$

decreases with mode number, j^* is a tunable parameter. The mode spectrum is normalized by a factor N_j so that all the modes sum to one. We have chosen $j^* = 3$. The phase of each wave is again sampled from a uniform distribution providing a random realization of the internal wave field. This model is similar to one used by previous authors[5] however the modes are solved

numerically rather than making a WKB approximation to the mode solutions.

The sound-speed anomaly is calculated with the NLVA scheme using both sound-speed profiles from TFO1 and TFO2. The power spectra of the sound-speed anomaly at each depth between 60-200 m every 0.5 m are estimated with Welch's method with 23-hour window lengths. Each spectrum is divided by the total power. The depth-average of those spectra is shown in Fig. 3.11.

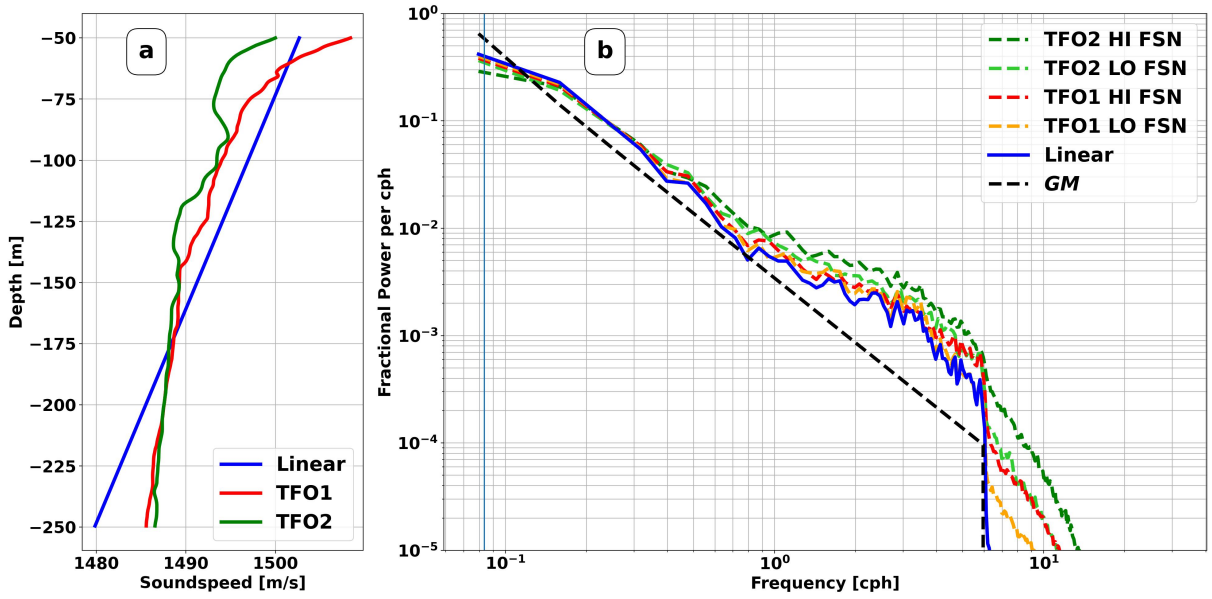

Figure 3.11. (a) Three sound-speed profiles between 0-250 m depth: a linear profile (blue line), sound-speed profile from the TFO1 experiment (red line), sound-speed profile from the TFO2 experiment (green line). (b) Depth-averaged sound speed fluctuations normalized by the total power of each spectra are split into groups that have fine-structure numbers above (green and red line) and below (light green and orange line) zero. These are labeled as HI FSN and LO FSN respectively. The blue line shows the SSA depth-averaged normalized spectra from a linear profile and is a proxy for the spectrum of simulated displacements. The Garrett and Munk frequency spectrum is plotted with a black-dashed line.

The whitening of the sound speed fluctuations is similar to the first model which contained no modes. The slope of the spectra for TFO1 and TFO2 past ω_c at high fine structure numbers are -3.7 and -4.3, respectively. The sound speed spectrum of the linear profile, which is a proxy for displacement, has an increase in power around N, which can be seen with the blue line in Figs. 3.11,3.12. The slope of the spectra derived from the linear and other sound speed

models flattens to a slope of between -1.7 to -1.4 between frequencies of 1-6 cph. This change in the internal wave spectrum near the buoyancy frequency is consistent with observations from our experiment and other ocean observations[37, 39].

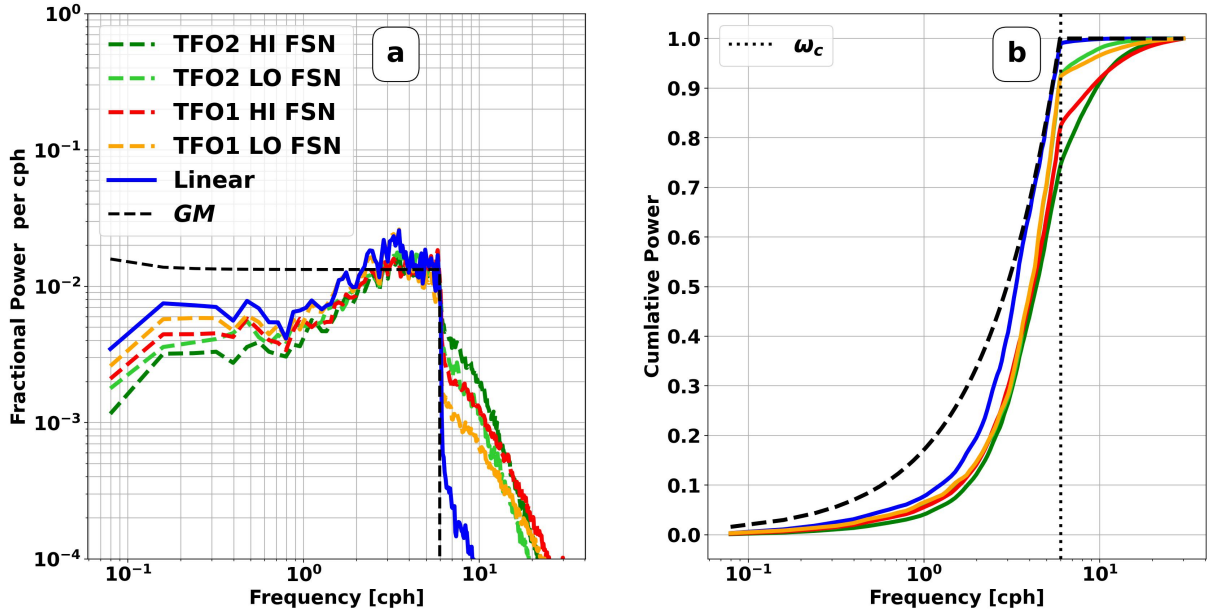

Figure 3.12. (a) Spectrum of $\dot{\delta c}$ from simulated sound speed fluctuations for a linear profile (blue line), a profile from TFO1 (red and yellow lines), and a profile from TFO2 (green and light green lines). The observed profiles are split into high and low fine structure numbers depending on whether $FSN > 0$. (b) The cumulative power is divided by the total power of the $\dot{\delta c}$ as a function of frequency.

This apparent bump in energy is explained by sampling depths in the upper part of the ocean where the stratification is large. The higher the frequency internal wave modes are trapped in the maximal part of the stratification, see Fig. 3.10b,c. Thus when we sampled displacements in the maximal part of the stratification we found more energy from high-frequency internal waves than the low-frequency internal waves that spread their energy over the entire water column.

The connection between the fine-structure number and harmonic ratio is revisited for the modal simulation, see Fig. 3.13. The simulation contains many realizations of a two-day time period of internal waves and sound-speed anomalies, which is more realizations than the 17-hour

series observations. The TFO1 profile in general has lower fine-structure numbers than TFO2. The combined data set samples fine structure numbers ranging from -1 to 1.75.

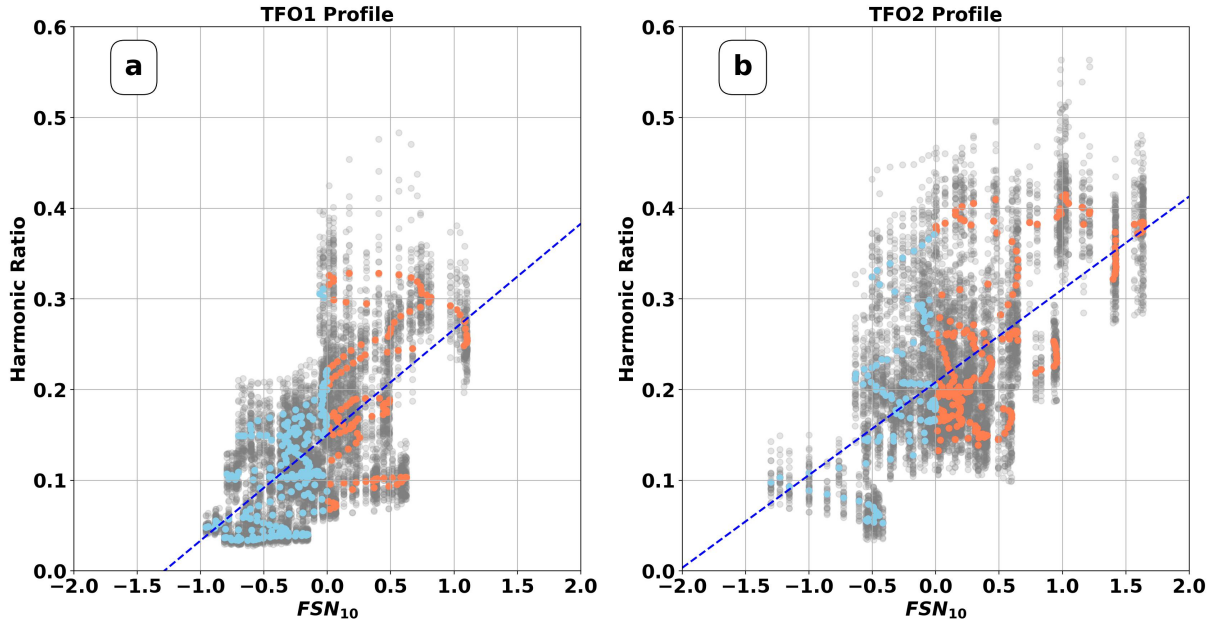

Figure 3.13. (a) A scatter plot of the harmonic ratio of sound speed fluctuations at each depth and realization versus the fine-structure number associated with that depth. Colored dots are the ensemble-mean of the harmonic ratio, with blue dots having harmonic ratios less than one, and orange dots having harmonic ratios greater than one. (b) The same scatter plot in (a) with the sound-speed profile from TFO2. Lines are fit to both scatter plots (blue dashed line) and have slopes of 0.12 and 0.10 for TFO1 and TFO2, respectively. The linear fits have R^2 values of 66 % and 62 % for TFO1 and TFO2, respectively.

The linear fit of harmonic ratio values for the TFO1 profile as a function of fine structure number is improved to an R^2 of 62% and with a similar slope of 0.12. This result is fairly consistent with the observations. The profile from TFO2 samples fine structure numbers above 1.25, and shows that the harmonic ratio for those depths continues to follow the increasing linear trend. The linear fit to the TFO2 dataset has a slightly shallower slope of 0.10 when compared to TFO1, however, the R^2 value of 66% has improved.

3.5 Discussion

The observational and simulated data of sound speed fluctuations from internal waves suggest that the vertical structure of the advected sound-speed profile impacts the time power spectra of those fluctuations. In particular, time scales that are shorter than the period of the buoyancy frequency cut-off have non-zero power when there is a non-trivial vertical structure in the sound-speed profile. The simulated and observed data, on average suggest that 20 % of the variability in the time rate of change in sound speed can happen at frequencies higher than the cut-off frequency. The simulated data has depths where the contribution is as high as 40%.

The modal spectrum of internal waves affects the calculation of the variability past the cut-off frequency. The modes give an additional 10 % amount of power near the cut-off frequency which is transferred to the harmonics of those frequencies for the non-linear sound-speed anomaly. This is demonstrated in the modal model compared to the depth-independent model. The modal model is validated by a flattening displacement spectrum near the cut-off frequency.

The fine structure number, N_f, is proposed as a way to estimate the change in the spectrum past the cut-off frequency. The base-10 logarithm of the fine structure number is positively related to the amount of variability past the cut-off frequency. The proportion factor between FSN_{10} and the harmonic ratio varied between 0.8 - 0.12 among the observed and simulated data sets with R^2 values ranging from roughly $50-70$ %. The fine-structure number in this paper only considers the second-order term in the Taylor expansion. Higher-order terms that are proportional to the higher-order vertical derivatives also contribute to energy at harmonic frequencies. Overall we find that if the second-order-vertical derivative of sound speed is large over the scale of the internal wave displacement then the change in the sound speed from the internal waves should use a non-linear calculation.

ACKNOWLEDGEMENTS

Chapter 3, in part is currently being prepared for submission for publication of the material. Author list DeFilippis, Jacob; Cornuelle, Bruce; Lucas, Drew; Colosi, John. The dissertation author was the primary investigator and author of this material.

Appendix A

Comparison Metrics

To quantify the difference between the observed and simulated arrivals over the array of hydrophones, the two-dimensional array data are converted into a single vector by concatenating the pressure record from each hydrophone along the time delay axis. The number of elements in the vector,

$$N = m \cdot T \cdot f_t \tag{A.1}$$

is equal to the time interval, T, times the sampling frequency, f_t, the number of hydrophone elements, m. Each pressure record is selected over a fixed $T = 5$ ms interval centered around the refracted arrivals. Those vectors of observed and simulated pressure were compared using the following metrics.

The Pearson Correlation Coefficient,

$$r = \frac{\sum_{i=1}^{N}(d_i - \overline{d})(\hat{d}_i - \overline{\hat{d}})}{\sqrt{\sum_{i=1}^{N}(d_i - \overline{d})^2(\hat{d}_i - \overline{\hat{d}})^2}} \quad , \tag{A.2}$$

and the MSE,

$$MSE = \frac{1}{N}\sum_{i=1}^{N}(d_i - \hat{d}_i)^2 \quad , \tag{A.3}$$

are calculated for $d_i = \frac{|p_i|}{\sum_{i=1}^{n}|p_i|}$ the magnitude of the observed pressure p_i normalized by the sum over the entire array vector, and $\hat{d}_i = \frac{|\hat{p}_i|}{\sum_{i=1}^{n}|\hat{p}_i|}$ the magnitude of the simulated pressure $\hat{p}_i$

normalized by the sum over the entire array vector. The MSE is reported scaled by the average squared amplitude inside the pulse arrival, d_i, as the Skill Score,

$$SS = 1 - \frac{MSE}{\frac{1}{N}\sum_{i=1}^{N}(d_i)^2} \quad , \tag{A.4}$$

and scaled by the average observed squared amplitude outside the pulse arrival, d_j,

$$MSE_r = 10\log_{10}\left[\frac{MSE}{\frac{1}{M}\sum_{j=1}^{M}(d_j)^2}\right] \quad , \tag{A.5}$$

which is the MSE relative to the observational noise. The observational noise is calculated by taking the average of the squared amplitude of the matched filter output before and after the pulse arrival. The ratio of the MSE to the noise is then reported in decibels.

Appendix B

NLVA Scheme

Algorithm 1 is a simple algorithm describing how to calculate non-linear sound-speed anomalies from a time-by-depth dimensional array of isopycnal displacements. Given an initial sound speed profile represented by a vector of depths and sound speed, the sound speed anomaly can be calculated from the displacement array. A 1-dimensional interpolation, `interp()`, is performed on the initial sound speed profile. At each time, the initial depth vector is displaced by adding a displacement vector. A second interpolation is done on the displaced depth vector and the initial sound speed vector. The sound speed anomaly is calculated as the difference between those two interpolation functions evaluated on the initial depth vector minus the adiabatic gradient time displacement.

Algorithm 1. Algorithm for calculating the non-linear advected sound speed anomaly.

{Initialize Input Variables}
$Z \leftarrow [z_1, z_2, ...z_N]$
$C \leftarrow [c_1, c_2, ...c_N]$
$\gamma \leftarrow 0.016$
$\zeta \leftarrow [[\zeta_{00}, \zeta_{0,1}...\zeta_{0,N}]...[\zeta_{M0}, \zeta_{M,1}...\zeta_{M,N}]]$

{Initialize Output Variables}
$dC < -\mathbf{array}(M,N)$

$CofZ() \leftarrow \mathbf{interp}(Z,C)$ {Interpolate Initial Profile}
for j in M **do**
$D \leftarrow Z + \zeta[j,:]$
Ensure: $D_i < D_{i+1}$ {Displaced depths should not cross over each other}
$CofD() \leftarrow \mathbf{interp}(D,C)$ {Interpolate Displaced Profile}
$dC[j,:] \leftarrow CofZ(Z) - CofD(Z) - \gamma\zeta[j,:]$
end for

Bibliography

[1] Matthew H Alford. Fine-structure contamination: Observations and a model of a simple two-wave case. *Journal of physical oceanography*, 31(9):2645–2649, 2001.

[2] John A. Colosi. *Sound propagation through the stochastic ocean*, chapter 1, pages 14–20. Cambridge University Press, New York, NY, 2016.

[3] John A. Colosi. *Sound propagation through the stochastic ocean*, chapter 4, pages 144–156. Cambridge University Press, New York, NY, 2016.

[4] John A. Colosi. *Sound propagation through the stochastic ocean*, chapter 2, pages 63–75. Cambridge University Press, New York, NY, 2016.

[5] John A. Colosi and Michael G. Brown. Efficient numerical simulation of stochastic internal-wave-induced sound-speed perturbation fields. *The Journal of the Acoustical Society of America*, 103(4):2232–2235, April 1998. Publisher: Acoustical Society of America.

[6] John A. Colosi and Daniel L. Rudnick. Observations of upper ocean sound-speed structures in the North Pacific and their effects on long-range acoustic propagation at low and mid-frequencies. *The Journal of the Acoustical Society of America*, 148(4):2040–2060, October 2020. Publisher: Acoustical Society of America.

[7] Grant B. Deane, James C. Preisig, Chris T. Tindle, Andone Lavery, and M. Dale Stokes. Deterministic forward scatter from surface gravity waves. *The Journal of the Acoustical Society of America*, 132(6):3673–3686, December 2012.

[8] Jacob P. DeFilippis, Bruce D. Cornuelle, Andrew J. Lucas, William S. Hodgkiss, Luc Lenain, W. A. Kuperman, and Matthew H. Alford. Observations and simulations of caustic formation due to oceanographic fine structure. *The Journal of the Acoustical Society of America*, 154(3):1372–1388, September 2023.

[9] Paul Dierckx. *Curve and surface fitting with splines*, chapter 4, pages 53–69. Oxford University Press, 1995.

[10] T. F. Duda, S. M. Flatté, J. A. Colosi, B. D. Cornuelle, J. A. Hildebrand, W. S. Hodgkiss, P. F. Worcester, B. M. Howe, J. A. Mercer, and R. C. Spindel. Measured wave-front fluctuations in 1000-km pulse propagation in the pacific ocean. *The Journal of the Acoustical Society of America*, 92(2):939–955, August 1992.

[11] Timothy F. Duda and James B. Bowlin. Ray-acoustic caustic formation and timing effects from ocean sound-speed relative curvature. *The Journal of the Acoustical Society of America*, 96(2):1033–1046, August 1994. Publisher: Acoustical Society of America.

[12] Matthew Dzieciuch, Walter Munk, and Daniel L. Rudnick. Propagation of sound through a spicy ocean, the SOFAR overture. *The Journal of the Acoustical Society of America*, 116(3):1447–1462, September 2004. Publisher: Acoustical Society of America.

[13] Matthew A. Dzieciuch, Peter F. Worcester, and John A. Colosi. Time coherence of acoustic arrivals during the philsea09 experiment. *The Journal of the Acoustical Society of America*, 128(4):2385–2385, October 2010.

[14] Terry E. Ewart. A numerical simulation of the effects of oceanic finestructure on acoustic transmission. *The Journal of the Acoustical Society of America*, 67(2):496–503, February 1980.

[15] Terry E. Ewart, John E. Ehrenberg, and Stephen A. Reynolds. Observations of the phase and amplitude of individual fermat paths in a multipath environment. *The Journal of the Acoustical Society of America*, 63(6):1801–1808, June 1978.

[16] Terry E. Ewart and Stephen A. Reynolds. The mid-ocean acoustic transmission experiment, MATE. *The Journal of the Acoustical Society of America*, 75(3):785–802, March 1984.

[17] Maurice Ewing and J. Lamar Worzel. *LONG-RANGE SOUND TRANSMISSION*, page 1–32. Geological Society of America, 1948.

[18] Stanley M Flatte, Roger D Dashen, Walter Heinrich Munk, and Fredrik Zachariasen. *Sound transmission through a fluctuating ocean*, chapter 7, pages 101–106. Stanford Research Institute, 1977.

[19] Stanley M. Flatté, R. Leung, and S. Y. Lee. Frequency spectra of acoustic fluctuations caused by oceanic internal waves and other finestructure. *The Journal of the Acoustical Society of America*, 68(6):1773–1779, December 1980.

[20] Christopher Garrett and Walter Munk. Space-Time scales of internal waves. *Geophysical Fluid Dynamics*, 3(3):225–264, May 1972.

[21] Kay L. Gemba, Jit Sarkar, Bruce Cornuelle, William S. Hodgkiss, and W. A. Kuperman. Estimating relative channel impulse responses from ships of opportunity in a shallow water environment. *The Journal of the Acoustical Society of America*, 144(3):1231–1244, September 2018.

[22] Kay L. Gemba, Heriberto J. Vazquez, Joseph Fialkowski, Geoffrey F. Edelmann, Matthew A. Dzieciuch, and William S. Hodgkiss. A performance comparison between m-sequences and linear frequency-modulated sweeps for the estimation of travel-time with a moving source. *The Journal of the Acoustical Society of America*, 150(4):2613–2623, October 2021. Publisher: Acoustical Society of America.

[23] Adrian E. Gill. *Atmosphere-ocean dynamics*, volume 30, chapter 8, pages 256–266. Academic press, 1982.

[24] Ganesh Gopalakrishnan, Bruce D. Cornuelle, Matthew R. Mazloff, Peter F. Worcester, and Matthew A. Dzieciuch. State estimates and forecasts of the northern Philippine Sea circulation including ocean acoustic travel times. *Journal of Atmospheric and Oceanic Technology*, 38(11):1913 – 1933, 2021.

[25] Laurent Grare, Nicholas M. Statom, Nick Pizzo, and Luc Lenain. Instrumented wave gliders for air-sea interaction and upper ocean research. *Frontiers in Marine Science*, 8, 2021.

[26] Frank S. Henyey, Kevin L. Williams, Jie Yang, and Dajun Tang. Simultaneous Nearby Measurements of Acoustic Propagation and High-Resolution Sound-Speed Structure Containing Internal Waves. *IEEE Journal of Oceanic Engineering*, 35(4):684–693, October 2010.

[27] Jody M. Klymak, Robert Pinkel, and Luc Rainville. Direct breaking of the internal tide near topography: Kaena ridge, hawaii. *Journal of Physical Oceanography*, 38(2):380–399, February 2008.

[28] Yu. A. Kravtsov and Yu. I. Orlov. *Caustics, Catastrophes and Wave Fields*, chapter 2, pages 17–26. Springer Berlin Heidelberg, 1993.

[29] Luc Lenain and W. Kendall Melville. Autonomous surface vehicle measurements of the ocean's response to tropical cyclone freda. *Journal of Atmospheric and Oceanic Technology*, 31(10):2169–2190, October 2014.

[30] Murray D. Levine and James D. Irish. A statistical description of temperature finestructure in the presence of internal waves. *Journal of Physical Oceanography*, 11(5):676–691, May 1981.

[31] Andrew Lucas, , Robert Pinkel, and Matthew Alford. Ocean wave energy for long endurance, broad bandwidth ocean monitoring. *Oceanography*, 30(2):126–127, June 2017.

[32] Frank J. Millero, Chen-Tung Chen, Alvin Bradshaw, and Karl Schleicher. A new high pressure equation of state for seawater. *Deep Sea Research Part A. Oceanographic Research Papers*, 27(3):255–264, 1980.

[33] Walter Munk, Peter Worcester, and Carl Wunsch. *Ocean Acoustic Tomography*, chapter 2, pages 38–56. Cambridge University Press, 1995.

[34] Walter Munk, Peter Worcester, and Carl Wunsch. *Ocean Acoustic Tomography*, chapter 5, pages 173–215. Cambridge University Press, 1995.

[35] Thomas R. Osborn and Charles S. Cox. Oceanic fine structure. *Geophysical Fluid Dynamics*, 3(4):321–345, 1972.

[36] R. Pinkel, M. A. Goldin, J. A. Smith, O. M. Sun, A. A. Aja, M. N. Bui, and T. Hughen. The Wirewalker: A Vertically Profiling Instrument Carrier Powered by Ocean Waves. *Journal of Atmospheric and Oceanic Technology*, 28(3):426–435, March 2011. Publisher: American Meteorological Society Section: Journal of Atmospheric and Oceanic Technology.

[37] Robert Pinkel. Observations of the Near-Surface Internal Wavefield. *Journal of Physical Oceanography*, 11(9):1248–1257, September 1981. Publisher: American Meteorological Society Section: Journal of Physical Oceanography.

[38] Robert Pinkel. Advection, phase distortion, and the frequency spectrum of finescale fields in the sea. *Journal of Physical Oceanography*, 38(2):291–313, February 2008.

[39] K. L. Polzin and Y. V. Lvov. Toward regional characterizations of the oceanic internal wavefield. *Reviews of Geophysics*, 49(4), November 2011.

[40] James C. Preisig and Grant B. Deane. Surface wave focusing and acoustic communications in the surf zone. *The Journal of the Acoustical Society of America*, 116(4):2067–2080, 2004.

[41] Stephen A. Reynolds, Stanley M. Flatté, Roger Dashen, Barry Buehler, and Pat Maciejewski. AFAR measurements of acoustic mutual coherence functions of time and frequency. *The Journal of the Acoustical Society of America*, 77(5):1723–1731, May 1985.

[42] Edward L. Richards and John A. Colosi. Observations of ocean spice and isopycnal tilt sound-speed structures in the mixed layer and upper ocean and their impacts on acoustic propagation. *The Journal of the Acoustical Society of America*, 154(4):2154–2167, 10 2023.

[43] John C. Steinberg and T. G. Birdsall. Underwater sound propagation in the straits of florida. *The Journal of the Acoustical Society of America*, 39(2):301–315, February 1966.

[44] Henry Stommel and K. N. Fedorov. Small scale structure in temperature and salinity near Timor and Mindanao. *Tellus*, 19(2):306–325, January 1967.

[45] Chris T. Tindle. Wavefronts and waveforms in deep-water sound propagation. *The Journal of the Acoustical Society of America*, 112(2):464–475, 2002.

[46] Robert E. Todd, Daniel L. Rudnick, Matthew R. Mazloff, Bruce D. Cornuelle, and Russ E. Davis. Thermohaline structure in the california current system: Observations and modeling of spice variance. *Journal of Geophysical Research: Oceans*, 117(C2), February 2012.

[47] B.A. Warren. *Evolution of physical oceanography*, chapter 9, pages 266–267. MIT Press, 1981.

[48] Peter F. Worcester. Reciprocal acoustic transmission in a midocean environment. *The Journal of the Acoustical Society of America*, 62(4):895–905, October 1977.

[49] Peter F. Worcester. Reciprocal acoustic transmission in a midocean environment: Fluctuations. *The Journal of the Acoustical Society of America*, 66(4):1173–1181, October 1979.

[50] Bofu Zheng, Andrew J Lucas, Robert Pinkel, and Arnaud Le Boyer. Fine-scale velocity measurement on the wirewalker wave-powered profiler. *Journal of Atmospheric and Oceanic Technology*, 39(2):133–147, 2022.